

PHOTO-ELECTROFORMING: A NEW MANUFACTURING  
PROCESS FOR MICRO-ELECTRO-MECHANICAL SYSTEMS

BY

CHE-CHIH TSAO

B.S., National Tsing Hua University (1985)

M.S., National Taiwan University (1987)

Submitted to the Department of Mechanical Engineering  
in Partial Fulfillment of the Requirements

for the Degree of

DOCTOR OF PHILOSOPHY

at the

Massachusetts Institute of Technology

February 1995

Copyright 1994, MIT. All rights reserved.

Signature of Author \_\_\_\_\_

Department of Mechanical Engineering

December 22, 1994

Certified By \_\_\_\_\_

Emanuel Sachs

Professor of Mechanical Engineering

Thesis Supervisor

Accepted By \_\_\_\_\_

Ain Sonin

Chairman, Department Committee on Graduate Students

Eng.

# Photo-Electroforming: A New Manufacturing Process for Micro-Electro-Mechanical Systems

by  
Che-Chih Tsao

Submitted to the Department of Mechanical Engineering  
on December 22, 1994 in partial fulfillment of the  
requirements for the Degree of Doctor of Philosophy in  
Mechanical Engineering

## Abstract

A new manufacturing process for making micro-electro-mechanical systems (MEMS) called Photo-Electroforming was conceived, demonstrated, and studied. Photo-Electroforming builds parts by an additive process which defines geometry by depositing powder in layers and creating regions of selective conductivity by laser enhanced electroless plating. The conductive region is then joined by a second plating step into an integral part. The unmetallized portion is removed by selective etching after all layers are defined and joined.

Based on different methods of powder deposition, two process sequences, the Sequential approach and the Continuous approach, were developed. Single-layer and dual-layer stand-alone parts made of nickel/silicon carbide composites of overall size 75-100  $\mu\text{m}$  and feature size of 25 microns were created by the Sequential approach. Crude patterns and interlayer bonding were also demonstrated by the Continuous approach.

The mechanism of laser enhanced electroless plating was investigated to understand parameters controlling process rate and resolution. The rate of pattern definition is mainly controlled by heat transfer and the resolution is mainly controlled by the diverging effect of hydrogen bubbles generated during the electroless plating process. The deposition rate of laser enhanced electroless plating appears to be controlled by mass transfer, which is enhanced by the formation and detachment of hydrogen bubbles during the plating. The bubble displacement model of Ibl and Venzel provided a reasonable match to the data.

The planar resolution achieved was 10-15  $\mu\text{m}$ , using a 12  $\mu\text{m}$  focused laser spot. The layer thickness was 5-10  $\mu\text{m}$ . The writing speed achieved was 24 cm/sec, at 1.5 W. With improved optics and higher laser power, finer resolution and higher writing speed can be achieved. In comparison with existing IC-based poly-silicon technique, Photo-Electroforming has fewer steps and each step requires less operation time and equipment with lower costs. Expected potential areas of applications include multilayer electronic packaging, MEMS fabrication, and micro-tooling.

## Thesis Committee:

Prof. Emanuel Sachs of Mechanical Engineering, Chairman

Prof. Donald Sadoway of Materials Science and Engineering

Prof. Martin Schmidt of Electrical Engineering and Computer Science

*Dedicated to my wife, Han-jie*

## Acknowledgments

I would like to thank my adviser, Prof. Emanuel Sachs, for his support, advice, and the venturous decision in September 1989 to start this research with me. This five-year process has been very exciting and bountiful.

Prof. Donald Sadoway's guidance and encouragement is especially helpful. His challenge on the theoretical portion of this work as well as his help on experimental equipment is deeply appreciated.

I would also like to thank Prof. Martin Schmidt. His advice helps me to formulate this thesis in a more omnibus viewpoint.

The technical help from Mr. Fred Cote of LMP must be appreciated in particular. The assistance from Ms. May Lu, Mr. Tim McClure, and Mr. Richard Perilli in Building 13 is acknowledged. Without their help, many works become impossible. Miss Shelley Alden's help in preparing and printing the figures is deeply appreciated. And the help from Mr. T. Bloomstein on the modeling of laser heating is also acknowledged.

And finally, the financial support from the MIT Leaders for Manufacturing Program and the National Science Foundation is acknowledged.

# Table of Contents

<b>Abstract</b>	2
<b>Dedication</b>	3
<b>Acknowledgments</b>	4
<b>Table of Contents</b>	5
<b>List of Figures</b>	7
<b>List of Tables</b>	9
<b>List of Symbols</b>	10
<b>1. Introduction</b>	
1.1 Motivation and Goal	11
1.2 Related Work	14
1.3 Method of Approach	15
<b>2. Photo-Electroforming - Process Concept</b>	
2.1 Basic Concept	17
2.2 Photo-Metallization	17
2.2.1 Method of Electroless Plating	
2.2.2 Method of Photo-deposition on Semiconductor	
2.2.3 Method of Silver Halide	
2.3 Layer Material Deposition	22
2.3.1 Particles	
2.3.2 Sheet	
2.4 Joining	25
2.4.1 Plating	
2.4.2 Enhanced Sintering	
2.5 Removal/Treatment of Un-metallized Material	26
2.5.1 Removal	
2.5.2 Infiltration	
<b>3. Feasibility Study</b>	
3.1 Study of Photo-Metallization Methods - A Brief Summary	28
3.1.1 Laser Enhanced Electroless Plating	
3.1.2 Semiconductor Method	
3.1.3 Silver Halide Method	
3.1.4 Conclusion	
3.2 Process Demonstration by Electroless Plating	32
3.2.1 Sequential Photo-Electroforming	
3.2.2 Continuous Photo-Electroforming	
3.2.3 Conclusion	
<b>4. Process Mechanism Understanding</b>	
4.1 Surface Temperature: Ni-glass experiments	46
4.2 Deposition Rate Controlling Mechanism	54

4.2.1 Temperature Effect	
4.2.2 Mass Transfer Effect	
4.2.3 Laser Enhancement	
4.3 Gas Bubble Effect	74
4.4 Surface Temperature: SiC samples	74
<b>5. Process Characteristics</b>	
5.1 Rate	82
5.2 Resolution	87
5.3 Material Strength	91
5.4 Material Flexibility	97
5.5 Comparison of Sequential and Continuous Approaches	99
5.6 Comparison of Photo-Electroforming and Existing Techniques	101
<b>6. Applications</b>	
6.1 Multilayer Electronic Packaging	106
6.2 Micro-Electro-Mechanical Systems	108
6.3 Micro-Tooling	109
<b>7. Conclusions</b>	111
<b>Appendices</b>	
<b>A1: Experimental Details on Laser Enhanced Electroless Plating</b>	A-1
<b>A2: Experimental Details on Semiconductor Method</b>	A-7
<b>A3: Experimental Details on Silver Halide Method</b>	A-12
<b>A4: Thermal Conductive Model for Laser Heating</b>	A-14
<b>A5: Thermal Conductive-Convective Model for Laser Heating</b>	A-17
<b>A6: Boundary Layer Thickness and Diffusion Layer Thickness Estimation</b>	A-23
<b>A7: Bubble Displacement Model</b>	A-27
<b>A8: Electroless Plating: Principle, Bath Composition, and Sample Preparation</b>	A-29
<b>A9: Material Properties</b>	A-33
<b>A10: Flow-through Plating</b>	A-38
<b>Bibliography</b>	

# List of Figures

- Fig. 1 Basic concept of Photo-Electroforming
- Fig. 2 Basic concept of Photo-Electroforming by semiconductor method
- Fig. 3 Basic concept of Continuous Photo-Electroforming
- Fig. 4 Line pattern created by laser induced electroless Cu plating on a SiC pellet
- Fig. 5 Line pattern created by laser induced electroless Ni plating on a SiC pellet
- Fig. 6 Process sequence of the Sequential Photo-Electroforming
- Fig. 7 Stand-alone single layer part created by Sequential Photo-Electroforming
- Fig. 8 Stand-alone dual layer part created by Sequential Photo-Electroforming
- Fig. 9 Stand-alone single layer part created by Continuous Photo-Electroforming
- Fig. 10 Simple patterns created by Continuous Photo-Electroforming
- Fig. 11 A single layer pattern joined to a base of Ni powder; Continuous Photo-Electroforming
- Fig. 12 Whisker structures formed by single beam Continuous Photo-Electroforming
- Fig. 13 Dual-beam concept and its setup
- Fig. 14 Surface temperature increase estimated by pure conduction and conductive-convective model
- Fig. 15 Lines created by laser induced electroless Ni on sputtered Ni film on glass at different power
- Fig. 16 Turn table setup for scanning tests
- Fig. 17 Experimental surface temperature increase on Ni-coated glass
- Fig. 18 Results of Ni-coated glass water quenching test
- Fig. 19 Close-up of lines created by laser enhanced electroless Ni on SiC pellet at different power
- Fig. 20 Deposition thickness of laser induced electroless Ni on Ni-coated glass at different power
- Fig. 21 Qualitative temperature history in laser enhanced electroless plating at different power
- Fig. 22 Temperature sensitivity of electroless Ni deposition rate
- Fig. 23 Qualitative surface temperature profile indicating laser exposure duration and cooling period
- Fig. 24 Observed cooling period on SiC pellets
- Fig. 25 Continuing deposition in cooling period, in-situ observation
- Fig. 26 Experimental laser induced electroless Ni deposition rate

## List of Figures (cont'd)

- Fig. 27 Laser Induced electroless Ni deposition on SiC at different power
- Fig. 28 Ni deposition rate in Continuous Photo-Electroforming at different cell pressure
- Fig. 29 Successive image frames of slow laser scanning across SiC pellet in electroless Ni solution
- Fig. 30 Comparing experimental deposition rate of laser induced electroless Ni with mass transfer limits
- Fig. 31 Ni deposition rate in log scale vs.  $1/T$  plot
- Fig. 32 Bubble shielding effect
- Fig. 33 Successive image frames of laser scanning across Ni-film on glass in electroless Ni solution
- Fig. 34 Ray tracing analysis to explain bubble shielding and diverging effect
- Fig. 35 Comparing resolution of back scanning and front scanning of laser induced electroless Ni on Ni-coated glass
- Fig. 36 Estimated temperature increase on SiC pellet in electroless solution
- Fig. 37 Successive image frames of laser scanning across SiC pellet in electroless Ni solution
- Fig. 38 Dimensionless solution of conductive-convective model of laser heating (scanning)
- Fig. 39 A Ni/SiC line created at scan speed 24 cm/sec
- Fig. 40 Dimensionless thermal diffusion distance by conductive-convective model of laser heating (scanning)
- Fig. 41 Comparing experimental resolution and theoretical thermal diffusion distance
- Fig. 42 Tensile strength of micro bars formed by Sequential Photo-Electroforming
- Fig. 43 Apparatus for tensile test
- Fig. 44 A typical broken micro bar after tensile test
- Fig. 45 Optical compatibility of various materials for Photo-Electroforming
- Fig. 46 Comparison of Sequential Photo-Electroforming and Poly-Si technique
- Fig. 47 Making multi-layer electronic package substrate by Photo-Electroforming
- Fig. 48 Making micro-actuator by Photo-Electroforming

## **List of Tables**

Tab. 1 Process characteristics of current MEMS fabrication techniques

Tab. 2 Strength of Photo-Electroformed parts in comparison with other related materials

Tab. 3 Comparison of Photo-Electroforming and existing techniques

## List of Symbols

$\alpha$	thermal diffusivity
$\beta = \frac{h}{2k}$	dimensionless heat transfer coefficient
$\delta_o; \delta_p$	diffusion layer thickness
$\nu$	fluid viscosity
$\mu$	fluid viscosity
$\epsilon$	porosity
$\lambda$	wavelength
$v$	volume generation rate of gas
$\tau$	time constant
A	surface area
$a_b$	radiative absorptance of the solid surface,
C	bulk concentration of species
D	diffusivity
$d_{bl}$	bubble diameter
F	Faraday constant, 96487
$f$	focal length
$f_c$	correction factor to account for solution absorption, bubble shielding etc.
h	heat transfer coefficient
i	current
$i_l$	Cottrell limiting current
j	flux of species; current density
$j_l$	mass transfer limited flux of species
k	thermal conductivity; reaction rate constant
L	powder bed depth
M	atomic weight
n	number of electron transferred
P	laser output power
p	effective input power density
$\Delta p$	dynamic pressure difference
Q	energy
q	energy per unit area
R	deposition rate; radius
r	radius; radial distance
$r_{bl}$	radius of gas bubbles
s	specific area (area per unit volume)
T	temperature
t	time
$U_o$	free stream velocity
u	flow velocity; laser scan speed
v	volume flow rate
w	radius of incident laser beam
$w_o$	radius of focused beam waist
$y_h$	hydrodynamic boundary layer thickness

# 1. Introduction

## 1.1 Motivation and Goal

Micro-electro-mechanical (MEM) devices have become a focus of interest of both the academy and the industry due to their technical challenge as well as market potential. Devices of various structures and functions, mostly sensors and actuators, have been demonstrated and some of them, such as pressure sensors, have been commercialized [Wolfe 1990, O'Connor 1992]. A demand for micro-electro-mechanical (MEM) devices is now increasing. On the other hand, the development of integrated circuits also fosters the fabrication of small mechanical objects. Typical examples are the injection molding tools for making small, complicated electronic connectors[Bertoncini 1990] and multilayer ceramic packages for microchips[Tucker 1992]. Another recent development related to small scale technology is the invention of the scanning tunneling microscope[Binnig 1982]. Its commercialization and various applications in a number of fields[e.g. Streker & Persch 1991; Haberle et al. 1991] opened new possibilities for "nanotechnologies" for novel commercial products. Therefore, it is highly possible that these three developments, micro-sensors and actuators, microelectronic packaging and connectors, and nanotechnology, will jointly promote the development of a "small-scale industry" in which peripheral parts for micro-chips or nanomachines together with micro-mechanical devices themselves will find market niches in various commercial applications.

At the present time, micro-mechanical fabrication is primarily based on the use of technology originally developed for integrated circuit (IC) fabrication. Cantilever beam and diaphragm based pressure sensors have been built and commercialized successfully [O'Connor 1992, Petersen 1988]. Integrated, movable micromechanical structures as well as electrostatic micromotors made of silicon and tungsten have also been fabricated and studied [Muller 1988, Fan 1988, Tai 1989, Macdonald 1989]. Methods for micro-

machining such as selective etching and etching stop techniques have also been developed [Seidel 1990, Wang 1991]. However, these techniques carry with them significant limitations. There are generally three categories of IC-based technology: bulk micromachining, wafer bonding, and surface micromachining [O'Connor 1992]. Table 1 summarizes the major process characteristics of these three categories of techniques (two related processes to be discussed in section 1.2 are also listed). From the table, one can see that there are three major limitations in IC based micromachining techniques:

1. Geometric limitation - Bulk etching techniques usually involve limitations associated with crystallographic angles. Wafer bonding techniques has the ability of simple geometry. In principle, surface machining can fabricate complex geometry by sequentially adding a layer of material, patterning it, and selectively removing portions of each layer. However, because material must be removed after each layer is patterned, and planarization steps may be required, the number of steps involved may be prohibitive.
2. Material limitation - The IC processing technology is primarily based on silicon processing. Therefore, most current micro-electro-mechanical systems (MEMS) are silicon based. However, to extend the application areas of MEMSs, other engineering materials such as metals and ceramics must be used.
3. Cost penalty - IC processing facilities are extremely expensive and they are designed mainly for mass production. However, future products in the small scale industry may feature diversity and small lot-size. Using current IC processing facilities for such a purpose may results in a great cost penalty.

In summary, to meet the growing need from the "small scale industry", novel techniques are necessary. Accordingly, the goal of this work is to develop a new technique for manufacturing MEMS which is able to:

- create fully three-dimensional (3-D) geometry;
- fabricate parts of various materials, including metals and ceramics; and
- manufacture MEMSs flexibly at a moderate cost.

Table 1 Process characteristics of current MEMS techniques

	Bulk Micromachining	Wafer Bonding	Surface Micromachining	LIGA or SLIGA	Photo-sensitive Polyimide
Rate per layer --patterning --growth or etching	masking + patterning 0.1-10 $\mu\text{m/s}$	masking + patterning $\sim 0.8 \mu\text{m/hr}$	masking + patterning $\sim 0.8 \mu\text{m/hr}$	masking + patterning $\sim 100\mu\text{m/hr}$ (Ni)	
Resolution --planar --layer thickness	$\sim 100\mu\text{m}$ $\sim 10\mu\text{m}$	$\sim 1\mu\text{m}$ $1-2 \mu\text{m}$	$\sim 1\mu\text{m}$ $1-2 \mu\text{m}$	$< 1\mu\text{m}$ $1-400 \mu\text{m}$	$\sim 1 \mu\text{m}$ $1-50 \mu\text{m}$
Material	Si	Si	poly-Si, Si <sub>3</sub> N <sub>4</sub> , W, Ni	Ni, Cu, platable metals	
Major equipment			LPCVD etc.	X-ray source	
Geometric flexibility --planar 2D --high aspect ratio 2D --fully 3D	✗ —	✗ need repeated layer growth, patterning, planarization	✗	✗	✗
Reference	Wolf & Tauber 1986	Peterson 1988	Muller 1988	Guckel 1991	Frazier & Allen 1992

## 1.2 Related Work

Besides standard IC processing techniques reviewed in the previous section, there are several other techniques under research and development which may have a goal similar to this work.

One of the most interested techniques is the LIGA process, originally developed at the Karlsruhe Nuclear Research Center, Germany. In this process, a thin layer of photoresist coated on a conductive base plate is patterned by photolithography to become a "micro-mandrel". Electroplating fills metal in the mandrel and produces micro-mechanical devices [Ehrfeld 1987]. Microactuators made of metal have also been built by adding a sacrificial layer in this process[Guckel 1991]. The major disadvantage of the LIGA process is the need of X-ray source, usually generated by expensive synchrotrons, for deep photolithography. Recent work by [Frazier & Allen 1992] used photo-sensitive polyimide as resist and therefore replaced X-ray with deep UV light.

Another technique which can produce micro-scale three dimensional patterns is laser deposition and etching developed at Lincoln Lab[Bloomstein 1991]. A UV or visible laser beam is focused on a substrate in contact with a moderate pressure molecular vapor thereby inducing photochemical or thermal chemical etching or deposition. However, this technique lacks the ability to make certain 3-D geometry, such as overhanging structure, due to the limit of its building scheme.

For the fabrication of larger mechanical parts, there is currently significant interest in the field called "Desktop Manufacturing"[Fallon 1989] or "Rapid Prototyping"[Ashley 1991]. Most of these processes involve building a part in layers where the geometry is defined by depositing a layer and then changing the properties of a selected portion of the layer. All layers are added before the excess material is removed in one final step and all the layers are sequentially fabricated in one machine. Among them, Three Dimensional Printing, under development at MIT, uses ink-jet printing of a binder material to selectively

join layers of powder to form parts [Sachs 1992]. Selective Laser Sintering, from DTM Corp., uses a laser to sinter areas of loosely compacted powder that is applied layer by layer [Deckard 1990]. There are other methods such as Fused Deposition Modeling [American Machinist 1990], Laminated Object Manufacturing [Fagin 1990], and Ballistic Particle Manufacturing [Masters 1990]. Generally, the above methods have a resolution no finer than 100  $\mu\text{m}$  [Ashley 1991], which does not satisfy the requirement of micro-mechanical fabrication. Another desktop manufacturing technique called Stereolithography which uses a laser to selectively solidify a photo-sensitive polymer has been used to fabricate micro-scale structures [Deitz 1990, Ikuta & Hirowatari 1993]. However, it is limited to making polymeric parts.

Clearly, a new approach for direct tooling and prototyping with high precision, fine resolution, and high material flexibility for micro-mechanical applications is necessary.

### **1.3 Method of Approach**

The basic method of this research was as follows,

1. setting a group of basic process features according to the goal described in section 1.1;
2. conceiving a basic process concept based on the process features, and develop its various process sequences ;
3. studying the feasibility of each possible process sequence in creating fully 3-D geometry;
4. investigating the process characteristics, such as rate, resolution, material strength, etc., of feasible process sequences and make a comparison with existing IC process based techniques.

In order to achieve the goal proclaimed in section 1.1, the following three basic process features were identified and used as a guideline for creating and developing the basic process concept:

- Buildup material by "additive-layer architecture" - To obtain the highest geometric flexibility, an additive-layer building architecture was adopted, where

the geometry is defined by depositing a layer and then changing the properties of a selected portion of the layer, and all layers are added before the excess material is removed in one final step. By experiences from the field of Desktop Manufacturing, this additive-layer architecture has the best geometric flexibility.

- Define geometry by light - To obtain the best precision and resolution, light was used to define the geometry of the property change in the layer, and was used to induced this property change.
- Form part by selective joining - To achieve higher throughput and geometric flexibility, the step of geometry definition and part forming should be decoupled. That is, the light patterning step only induce the property change but not necessarily join or form the part into an integrated solid. In stead, a selective joining step is applied later to join the geometry with changed property.

Each of the three features represents a technical field. Techniques and physics from these technical fields were selected and studied. Layer material deposition techniques was developed for "additive-layer architecture" to achieve fully 3-D capability. Different photo-induced metallization mechanisms were studied and tested to determine the most suitable one. Part joining methods of plating and selective sintering were studied and tested. Suitable techniques were then combined into a new technology to achieve the goal of this research. To author's knowledge, it was the first time that techniques from these three aspects were combined and a new manufacturing process based on these techniques was successfully developed.

## **2. Photo-Electroforming - Process Concept**

### **2.1 Basic Concept**

Based on the three principles in the method of approach, a process concept was conceived as the basic plan of this work, which is called Photo-Electroforming. The basic concept of Photo-Electroforming is illustrated in Fig. 1 with its four basic steps described as follows:

1. Layer material deposition - First, a thin layer of nonconductive porous material is deposited onto a porous base plate immersed in a working fluid. The porous material can be in the form of powders, porous sheets, or screens.
2. Photo-Metallization - Second, a scanning laser beam or a light pattern created by a photomask hits the layer material and the working fluid and induces metallization selectively to create conductive areas on the layer.

The steps of depositing layers of porous material and selective photo-metallization are repeated until the geometry of the complete part is defined.

3. Joining - After all the layers have been deposited and defined, a plating solution is pumped through the porous bed to plate metal onto the metallized areas of the material thereby joining the selectively defined portions. Another joining method is by enhanced sintering which functions according to the principle that a slight amount of additives can selectively change the sintering temperature of a powder material.
4. Removal/treatment of un-metallized material - After joining, the unwanted (unplated) material is removed to reveal the finished part, or is infiltrated with a liquid binder and then solidified into a block or substrate which contains a metallized internal structure.

### **2.2 Photo-Metallization**

Among many photo-induced metallization mechanisms, three mechanisms were identified as possible candidates for the photo-metallization step in Photo-Electroforming:

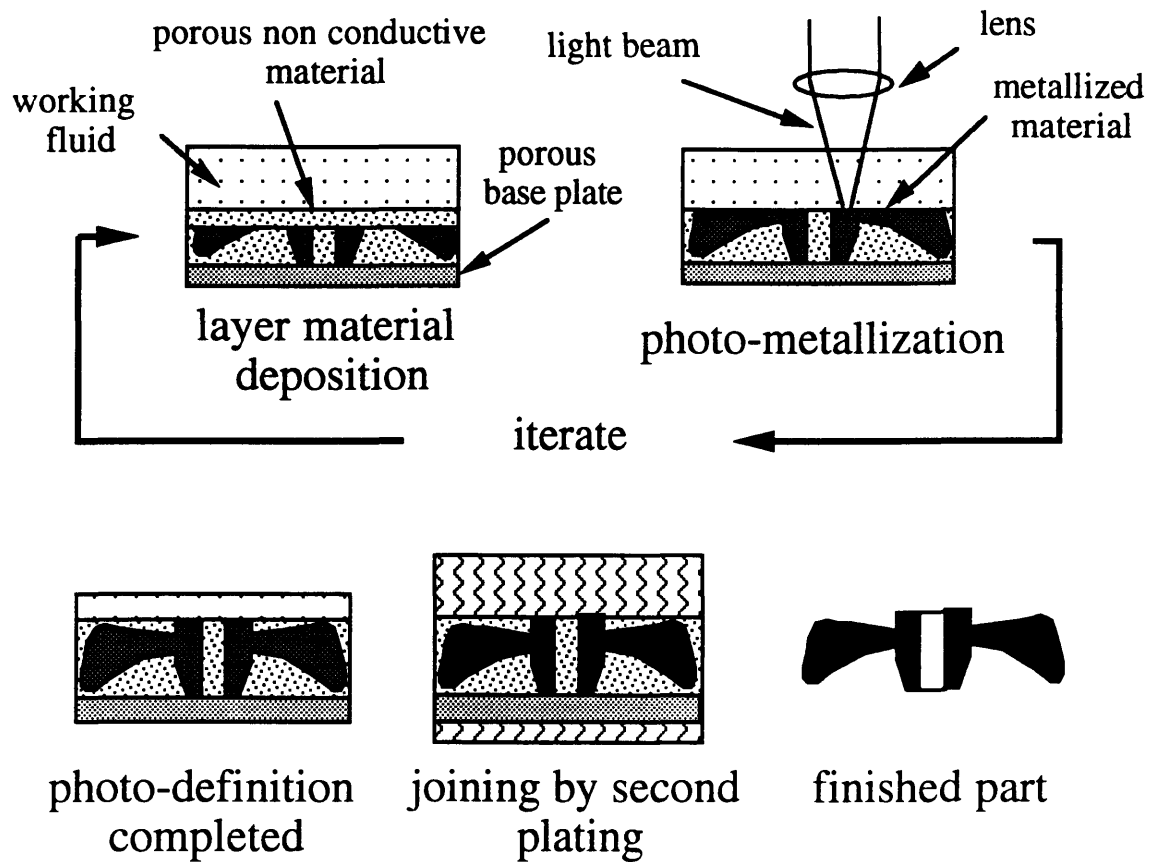


Fig. 1 Basic concept of Photo-Electroforming

- Method of electroless plating: Electroless plating solution is used as the working fluid and its photo-thermally sensitive nature enables the selective metallizing operation on nonconductive layer materials;
- Method of semiconductor: Semiconductor material is used as the layer material and a plating solution acts as the working fluid; and
- Method of silver halide: Silver halide coated material is used to build layers and photographic developer is used as the working fluid.

### **2.2.1 Method of Electroless Plating**

In an electroless plating solution, a chemical reducing agent supplies the electrons for converting metal ions to the elemental form. The reducing action can therefore occur on a catalytic surface without external current supply. Nonconductors can be metallized by electroless plating solution after a proper pretreatment. The principle, bath compositions, and sample preparation procedure of electroless nickel and copper plating are described fully in Appendix 8. The deposition rate of electroless plating process is sensitive to several factors, especially temperature. Therefore, a scanning laser beam or a light pattern generated by photomasks can selectively raise the temperature of material and create selective metallization with very fine features.

One feature of light (laser) induced electroless plating is the great rate enhancement created by the laser spot. Normally, the metal deposition rate in a hot bath is around 10-30  $\mu\text{m}$  per hour per unit area; however, a focused laser beam can increase the rate by 1000 times. A laser enhanced electroless deposition rate of 1-10  $\mu\text{m}$  per second has been reported in literature[Van der Putten 1988, Morita 1989]. This feature can be a great advantage for Photo-Electroforming.

### **2.2.2 Method of Photo-deposition on Semiconductor**

When a P-type semiconductor is immersed in a suitable electrolyte solution containing metal ions and is hit by light, metal reduction can happen at the light side of the particle and oxidation reactions can happen at the dark side. When a N-type semiconductor

is used, reduction reaction takes place on the dark side and oxidation on the light side. By choosing the redox reaction pair carefully, light induced metallization on part of a semiconductor surface can be done. This phenomenon is due to photocatalytic reaction, which means light accelerates a slow spontaneous reaction; or due to photoelectrolytic reaction, which indicates light drives an originally nonspontaneous reaction. A typical example is titanium oxide particles suspended in a solution of copper salts.[Pleskov 1986, Reiche 1979]. This photo-deposition phenomenon also works on silicon immersed in plating solutions [Kiang 1983]. Similar photoelectrochemical reactions can occur on a P-type semiconductor with part of its surface in ohmic contact with a metal. When this semiconductor-metal structure is immersed in a suitable electrolyte solution and is hit by light, the metal oxidizes to become metal ions and metal ions are reduced on the semiconductors.[Wrighton 1977] More details of the phenomenon are described in Appendix 2.

This photo-induced self-plating effect can be used as one way of photoselective metallization. Semiconductor particles with a portion of their surface coated with a metal in ohmic contact are used as the layer material, as shown in [Fig. 2](#). An electrolyte solution containing metal ions is used as working fluid. Incident light turns particles from partly metallized to fully metallized. In the final electroplating stage, those fully metallized particles can be plated into an integral object, while those partially metallized particles can not be joined together because there is not good electrical contact among them.

### **2.2.3 Method of Silver Halide**

In this approach, silver halide particles or thin film is used as the layer material, and a photographic developer, such as vanadous salts or hydroxylamine [Carrol 1980], is used as the working fluid. The layer material is first immersed in the developer and then exposed to light selectively. In the exposed region, silver forms. The unexposed particles or the portion of the film is then dissolved away by a fixer, and the silver particles remains.

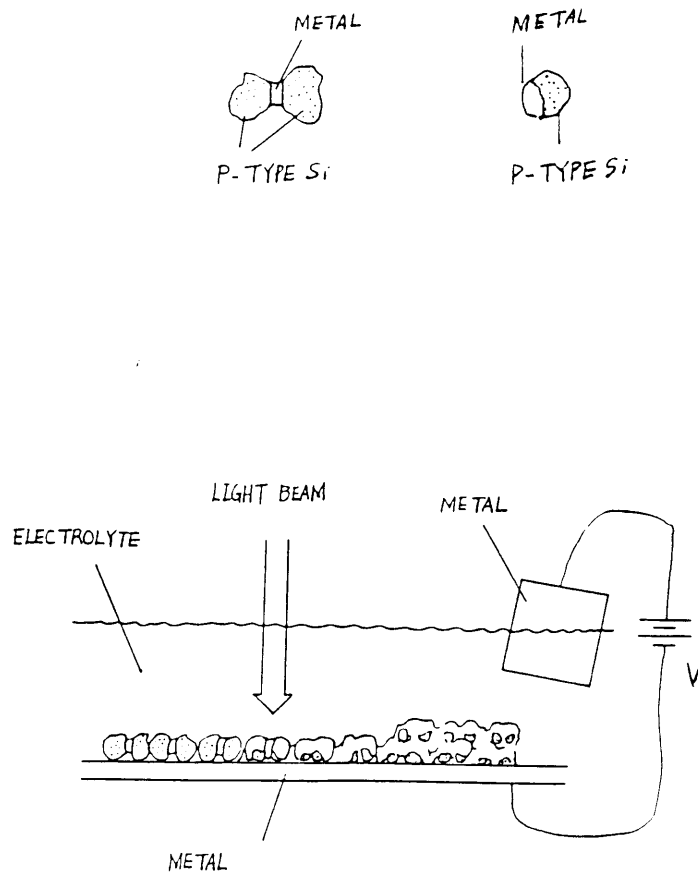


Fig. 2 Basic concept of Photo-Electroforming by semiconductor method

A planarization material is then added to fill the void, unexposed region. This selective exposure process is repeated layer by layer until the part geometry is completely defined. The silver particles can then be joined into an integral part by a second plating. And finally, the planarization material is removed to reveal the part.

## **2.3 Layer Material Deposition**

The primary requirement on the material is that it be porous and electrically non-conductive. Ceramic and plastic powders or porous sheets can be used. Metal powders with a plastic or oxide coating can also be used.

### **2.3.1 Particles**

The porous non-conductive material can be deposited in the form of particles which build up on previously deposited layers of particles. Two deposition methods can be applied: the first is to deposit particles layer by layer ex-situ (i.e. particles deposition is not in the photo-metallizing working fluid); the other is to deposit particles in-situ (i.e. together with working fluid). For convenience, the former is called sequential deposition and the latter continuous deposition, because it has the potential of continuous operation of Photo-Electroforming without interruption by layer operation.

Sequential deposition can be operated in two forms: dry deposition and wet deposition. Available techniques to perform dry deposition include dry pressing, wet pressing and firing (bonding), and techniques for wet deposition include sedimentation and casting. All the above techniques are widely used in the field of ceramics engineering (and in many cases in metal powder preparation). Description of these techniques can be found in, for example, [Richerson 1982].

In the continuous deposition, the fine particles may be transported in the working liquid, for example, as a dispersion in electroless plating solution. Fig. 3 shows a flow-

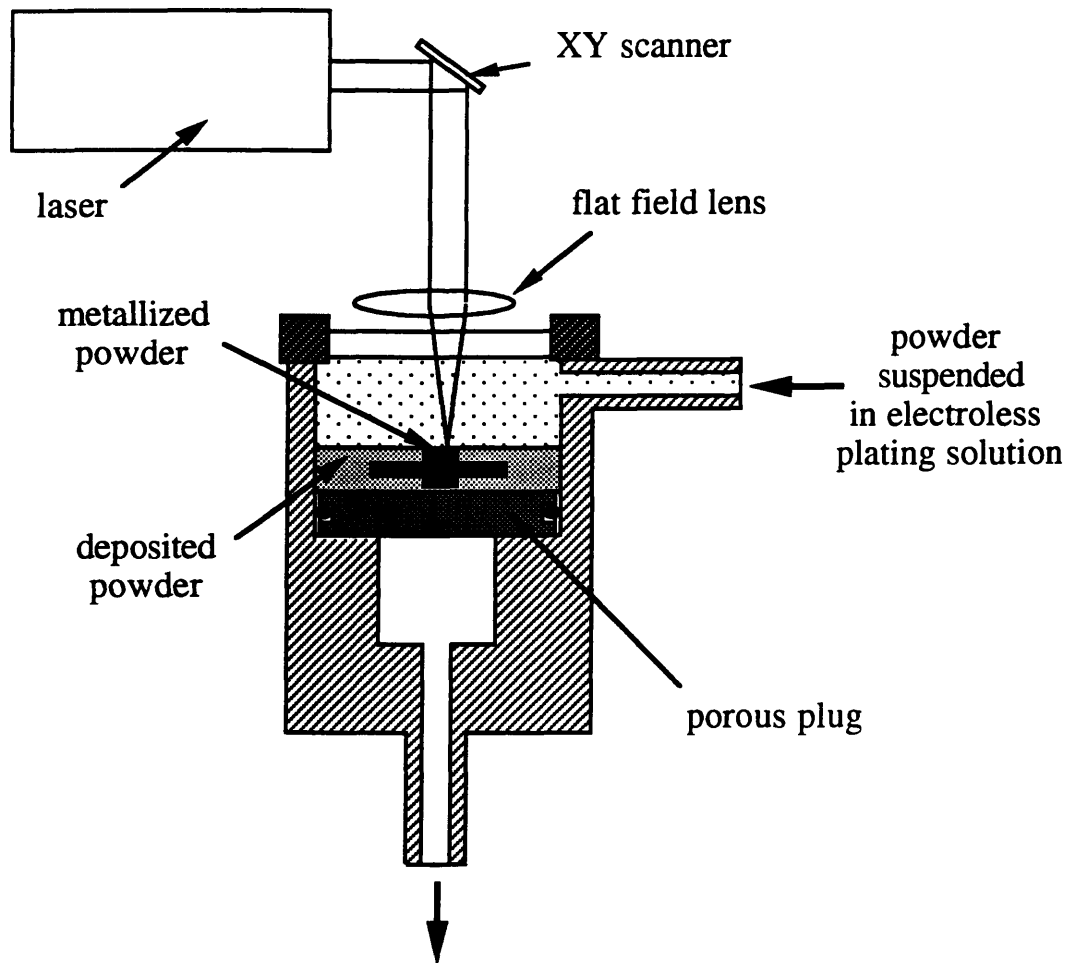


Fig. 3 Basic concept of Continuous Photo-Electroforming

through cell where the working liquid is pumped through the chamber. Discrete layers can be built up by pumping through fluid with particles in dilute suspension which are filtered by the previously deposited powder and are deposited in a manner somewhat like a snowfall. After a layer is deposited, working fluid with no particles can be pumped while a focused laser scans the deposited powder through a transparent window and through the working fluid above the surface of the deposited powder. Between layers, the chamber moves downward to keep the top surface of the powder at the focal point of the laser. The flow-through cell of Fig. 3 can also be used for a continuous version of Photo-Electroforming where the working fluid always transports particles into the system and the laser images through the dilute suspension of particles. In this case, parts can be created with steps no larger than the particle size itself. Imaging of the laser through the working fluid is possible in a case where the particle size is small and the suspension is very dilute.

### **2.3.2 Sheet**

The porous non-conductive material can also be deposited in the form of discrete sheets. The major challenge of this discrete-sheet method lies in the preparation of the sheets. There are several possible ways to prepare the porous sheets suitable for use in Photo-Electroforming. Tape casting is used to prepare ceramic sheets as thin as 10  $\mu\text{m}$ . The sheet porosity can then be controlled by varying sintering parameters. Such sheets can also be prepared by casting ceramic powder together with polymer (ex: PMMA) powder and then burning out the polymer filler and sintering the ceramics to yield a highly porous sheet. Another method is to create screens with micro scale mesh by photolithography. A thin film of photo-sensitive polyimide can be patterned by photolithography directly to make sheets with micro pores. Polyimide has high strength, high melting point, and good chemical resistance which are necessary in the processing environment of Photo-Electroforming. Still another method to create thin sheet with a fine porous structure is by Electrostatic Spinning Process. This process uses a strong static electric field to draw

droplets of polymer solution into long thin polymer fibers and weaves them into porous sheets [Berry 1993]. One issue associated with this discrete-sheet method is that a mechanism must be developed to deposit these sheets discretely.

## **2.4 Joining**

The joining step is best practiced after the entire geometry has been defined, rather than on a layer by layer basis. In this manner only one joining step is required and the joining time can be minimized. Further, any build up of stress in the component is minimized by treating the whole part at once. Two methods for joining the photo-metallized regions are described.

### **2.4.1 Plating**

To obtain the variety of materials and dimensional accuracy, plating is used as a major forming method. The metallized layer material can be joined either by electroplating or by electroless plating.

Since electroless plating is an autocatalytic process, flowing a heated electroless plating solution through a powder bed causes continuous metal deposition in regions previously defined by photo-metallization. Thus, if a high enough flow is maintained to guarantee uniform plating, high densities can be achieved. A theoretical analysis of flow-through electroless plating was done and is given in Appendix 10.

Traditionally, electroplating and electroforming has been a precise method for producing intricate parts of various sizes[Siegrist 1964]. An electroplating solution can be pumped to flow through the selectively metallized bed of layer material, thereby joining the material into an integral part by electrodeposition of metal. In this case, the layer material actually acts as a porous cathode. An analysis of electrolytic flow-through plating is also given in Appendix 10. One important advantage of using electrolytic plating as the joining

method is that different metals can be electroplated onto different portions of the photo-defined powder bed in the second plating step, as long as those portions are not connected electrically. As a result, integral assemblies can be fabricated with different materials plated in different locations.

#### **2.4.2 Enhanced Sintering**

It is known that certain metals act as "sintering aids" and greatly promote the speed of sintering. For examples, nickel activated tungsten and molybdenum can be sintered much more effectively than untreated cases [German 1990]. Accordingly, Photo-Electroforming can be used to provide sintering aids, such as nickel, to the preferred region of a powder bed. By controlling the sintering temperature, "selective sintering" of a preferred region can be achieved. The region without sintering aids can then be removed to reveal the finished parts. An advantage of this approach to joining is that a "full density" part can be attained in keeping with practice in powder metallurgy.

### **2.5 Removal/Treatment of Un-metallized Material**

The material which is not photo-metallized and joined together can either be removed to reveal the finished part, or it can be infiltrated to form a solid structure which contains electroformed regions.

#### **2.5.1 Removal**

In the layer-by-layer buildup process, the deposited powder acts as a support for subsequent layers. After the component is joined, the un-metallized powder can be removed using techniques such as selective etching and ultrasonic agitation, leaving just the photo-defined and joined component. By this technique, almost any geometry can be defined by Photo-Electroforming including overhangs, undercuts and internal volumes, as long as there is a hole for the loose powder to escape. The removal of thin layers of un-

metallized powder can function in a manner similar to the sacrificial layers used in current approaches to MEMS [Muller 1988].

### **2.5.2 Infiltration**

In some cases, it may be desirable to encapsulate a group of Photo-Electroformed structures within a block or substrate. This can be accomplished by infiltrating the bed of un-metallized powder with a liquid binder such as a polymeric binder. Such structures can be useful for electronic packaging.

## 3. Feasibility Study

### 3.1 Study of Photo-Metallization Methods - A Brief Summary

Among many photo-induced metallization mechanisms, three mechanisms were identified as possible candidates for the photo-metallization step in Photo-Electroforming:

- Method of electroless plating: Electroless plating solution is used as the working fluid and its photo-thermally sensitive nature enables the selective metallizing operation on nonconductive layer materials;
- Method of semiconductor: Semiconductor material is used as the layer material and a plating solution acts as the working fluid; and
- Method of silver halide: Silver halide coated material is used to build layers and photographic developer is used as the working fluid.

The feasibility of the above three methods were studied and the results are summarized briefly in this section (For experimental details please see Appendix 1-3).

#### 3.1.1 Laser Enhanced Electroless Plating

Laser enhanced electroless plating was found to be an excellent photo-metallization method for Photo-Electroforming except the disturbing effect of associated hydrogen gas bubbles. The ejection force created by a focused laser spot in an electroless plating solution bath is able to plow a trench on a firmly pressed powder bed. This ejection force is believed to be caused by sudden local boiling and by the continuous formation of hydrogen bubble. Firing the dry pressed powder bed in air helps to bond the particles in position during a laser exposure (see Appendix 1 for details). Line patterns were successfully created on the fired powder bed, as shown in [Fig. 4](#) and [Fig. 5](#), where laser enhanced electroless copper and nickel line patterns were defined on the surface of a silicon carbide pellet, which is created by dry pressing 1  $\mu\text{m}$  SiC powder followed by firing in air.

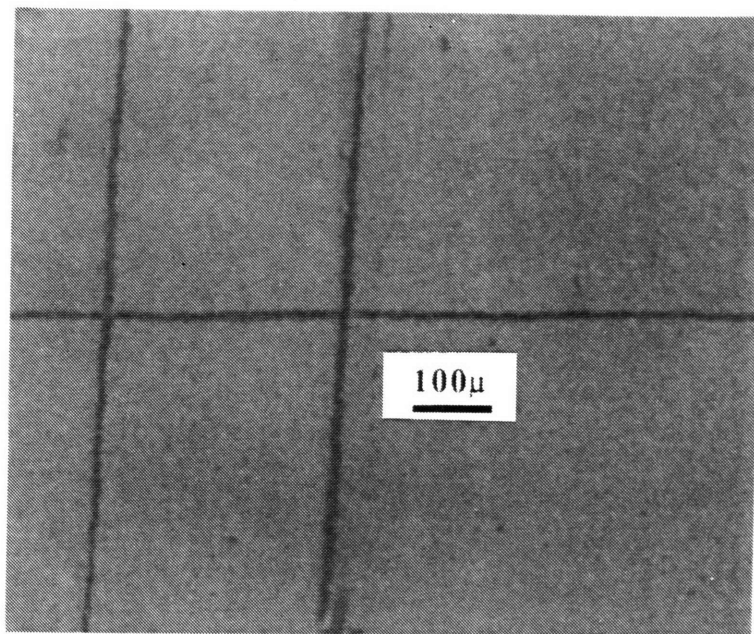


Fig. 4 Line pattern created by laser induced electroless Cu on SiC pellet, Sn/Pd pretreated, line width 10-15  $\mu\text{m}$ , laser power 0.8-1.0W, 12  $\mu\text{m}$  beam spot, scan speed 530  $\mu\text{m/s}$

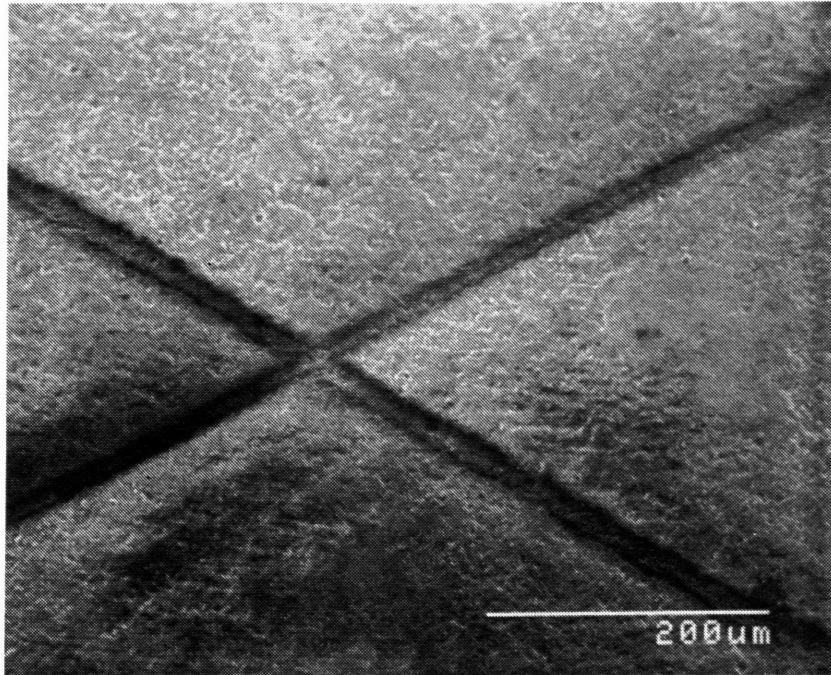


Fig. 5 Line pattern created by laser induced electroless Ni on SiC pellet, non-pretreated, laser power 1.2W, scan speed 5 cm/sec

### **3.1.2 Semiconductor Method**

The photo-metallization effect on semiconductor particles was found to be not significant enough for the purpose of Photo-Electroforming, despite that photo-metallization on bulk semiconductor is quite successful. Metal spots were created on the surface of a silicon wafer immersed in a copper sulfate solution by exposing it to a 5 mW He-Ne laser beam. But for single crystal Si particles of a size of 1-2  $\mu\text{m}$ , the photo-metallization phenomenon is much less significant and sometimes is not even observed. Details of this approach are given in Appendix 2. This decrease of quantum efficiency at particle sizes is probably caused by the increase of number of excess surface states per unit volume as the solid size decreases. The excess states associated with the dangling bonds at material surface consumes most of the excited charge carriers and therefore only a small fraction of photo-electrons react with the ions from the solution to form metal atoms.

### **3.1.3 Silver Halide Method**

Although the basic physics of photographic process is well established, technical difficulty was encountered in dissolving away unexposed silver halide without washing away reduced silver particles. Both silver bromide powder and thin film made from wet chemical reaction were tested. A pure silver image pattern was created by selective light patterning in a developer. However, the pattern was easily destroyed by the following fixing step. See Appendix 3 for more details. It is speculated that the very fine silver particles were carried away with the unexposed silver bromide being dissolved into the fixer.

### **3.1.4 Conclusion**

In conclusion, each of the three methods had their problems. In the semiconductor method, the quantum efficiency of photo-metallization decreases with particle size. If this efficiency decrease is due to increasing excess surface area to volume ratio, then single

crystal particles with perfect surfaces must be prepared to make this method work. This is obviously a complicated task. In the silver halide approach, to successfully exercise the fixing step, practical method have to be developed to dissolve the unexposed silver halide away without disturbing those tiny and loose silver metal. Since the size of silver halide grain is usually equal to or less than 1  $\mu\text{m}$ , the size of reduced silver metal particles must be on the sub-micrometer scale and therefore the practical difficulty in handling them can be extreme. The problem of hydrogen gas disturbance in the electroless plating method was comparatively less difficult to solve. Therefore, laser enhanced electroless plating was selected as the photo-metallization method, and the hydrogen bubble issue was to be solved.

## **3.2 Process Demonstration by Electroless Plating**

After selecting laser enhanced electroless plating as the photo-metallization method, the issue of hydrogen bubbles remains to be solved. Two methods of powder deposition, sequential deposition and continuous deposition, were studied. The two corresponding process sequences were called Sequential Photo-Electroforming and Continuous Photo-Electroforming respectively.

### **3.2.1 Sequential Photo-Electroforming**

#### **(1) Process Sequence**

Sequential Photo-Electroforming uses an ex-situ layer buildup scheme which bonds every new layer to the previous one by dry pressing and short firing. The bonding is strong enough to resist the disturbing force of hydrogen bubbles, yet can be selectively etched away in the final step. The process flow chart of Sequential Photo-Electroforming is shown in [Fig. 6](#), using SiC as an example. Silicon carbide powder was selected as the layer material for test because of its high absorptance of light of argon ion laser. Another

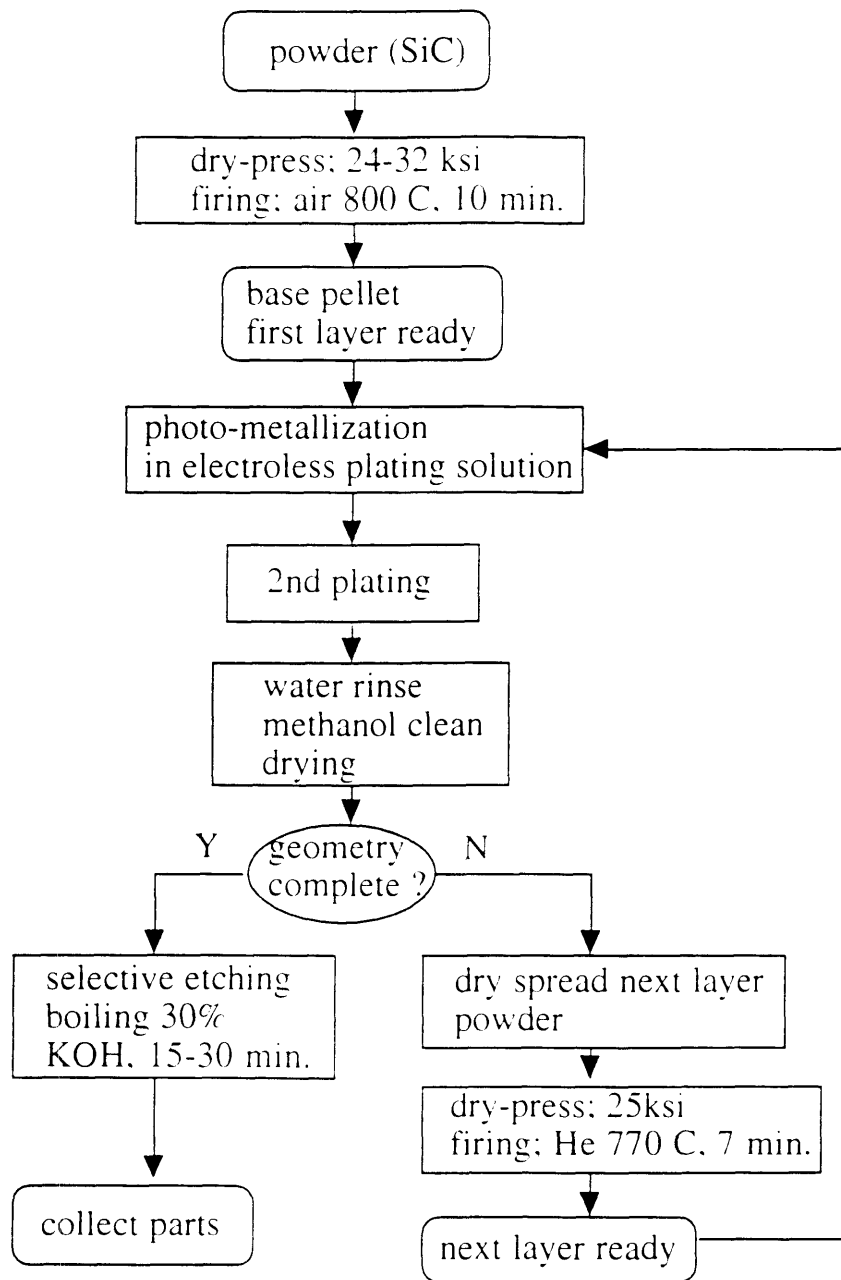
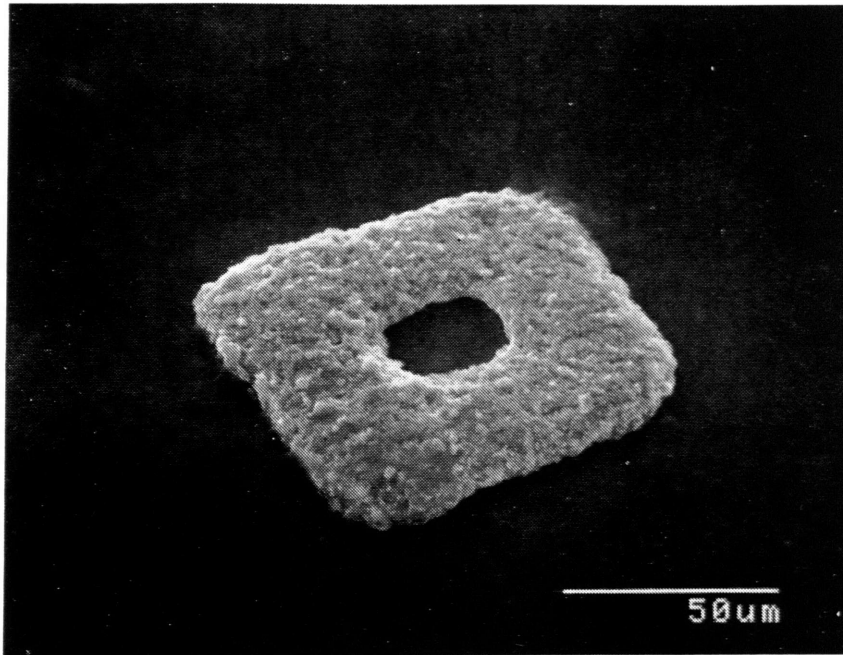


Fig. 6 Process Sequence of the Sequential Photo-Electroforming

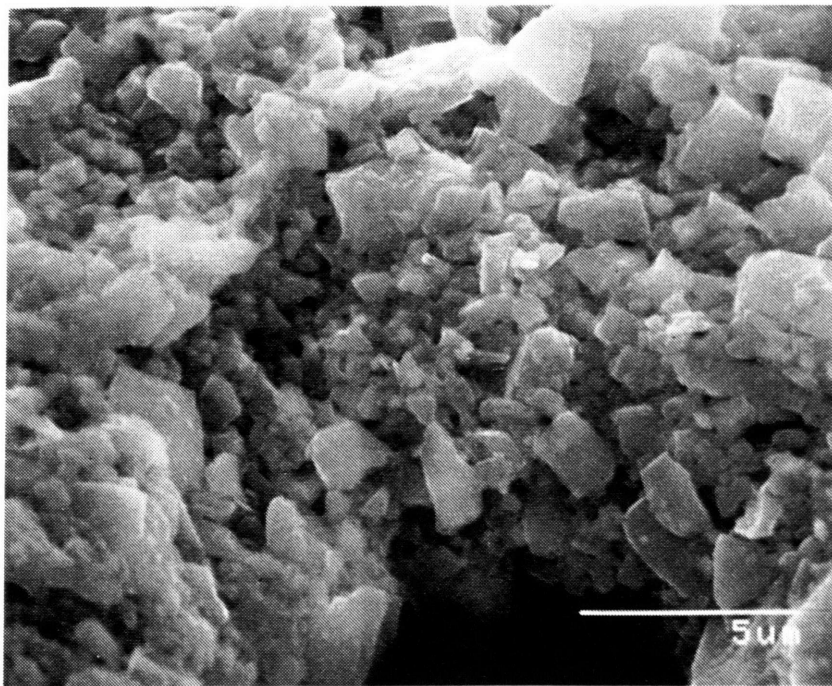
advantage of SiC is that the powder can be bonded by firing at a medium temperature, and then the bonding can be released by etching, as indicated in the process sequence. It is believed that the firing step causes the bonding of silicon dioxide on the surface of SiC particles being dry pressed into contact with each other, as the bonding can be released by etching in boiling potassium hydroxide or hydrofluoric acid, both etch silicon dioxide efficiently. In the process sequence illustrated in Fig. 6, oxidized SiC powder, which was prepared by firing in air for 15 min., was used for all add-on layers. The resulting excess silica on the oxidized surface of particles provides the necessary bonding material. The firing of add-on layers was done in helium so that the nickel metal was not oxidized. The strength of SiC pellets made of 1  $\mu\text{m}$  particles by dry press at 25 Kpsi was measured by 3-point bending and was found to be around 0.6-1.8 MPa. It was found that this strength was not able to resist the disturbing force created by the argon ion laser beam at the power density tested, 1-10  $\text{GW}/\text{cm}^2$ , in the electroless Ni plating solution. After firing in air at 800 C for 10 min., the strength can be increased to around 10 MPa, which is able to resist the laser disturbing force in electroless plating solution. Therefore, it seems that a tensile strength of several MPa is required to resist the disturbing force induced by laser enhanced electroless plating on SiC. For experimental details such as lasers and optics, electroless plating solutions, and sample preparation please see Appendices A1 and A8.

## (2) Results

In order to assess the feasibility of the Photo-Electroforming technique, some high resolution patterns and micro-mechanical parts were produced. [Fig. 4](#) shows a pattern of 15  $\mu\text{m}$ -wide copper/silicon carbide lines created by laser-induced electroless plating on a porous silicon carbide substrate. [Fig. 5](#) shows 25  $\mu\text{m}$ -wide Ni/SiC lines on a SiC substrate. [Fig. 7](#) shows a lifted nickel matrix silicon carbide square frame with a side to side dimension of 75  $\mu\text{m}$  and a thickness of approximately 8  $\mu\text{m}$ . And [Fig. 8](#) shows a dual-layer simple geometry.



(a)



(b)

Fig. 7 (a) Stand-alone single-layer part created by Sequential Photo-Electroforming; electroless Ni/SiC powder (b) Closer view

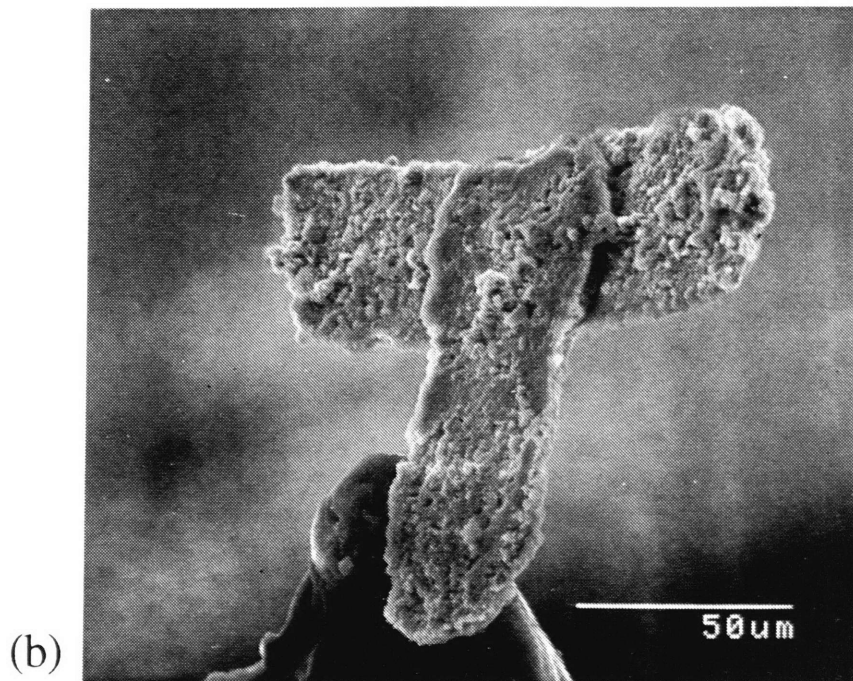
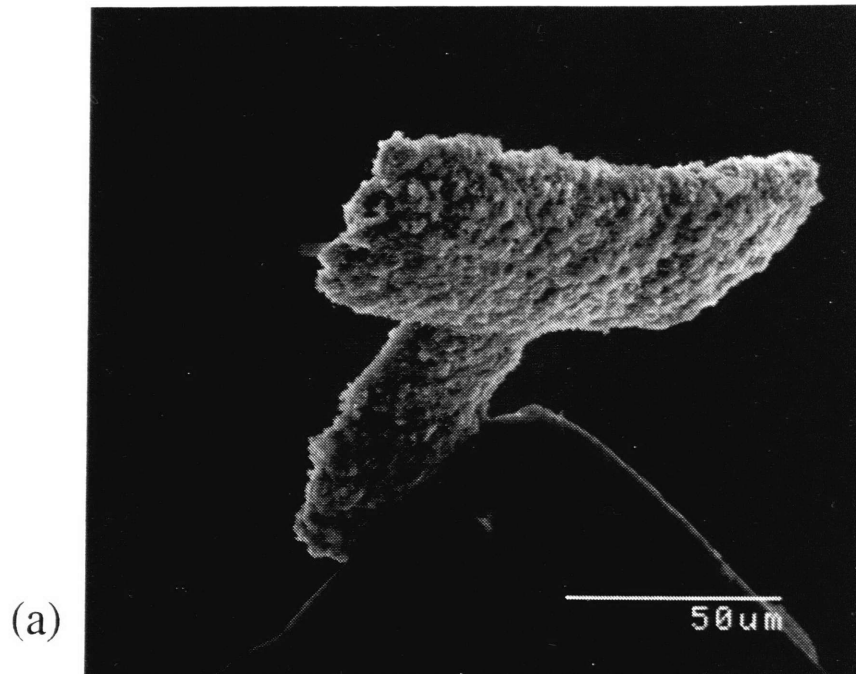
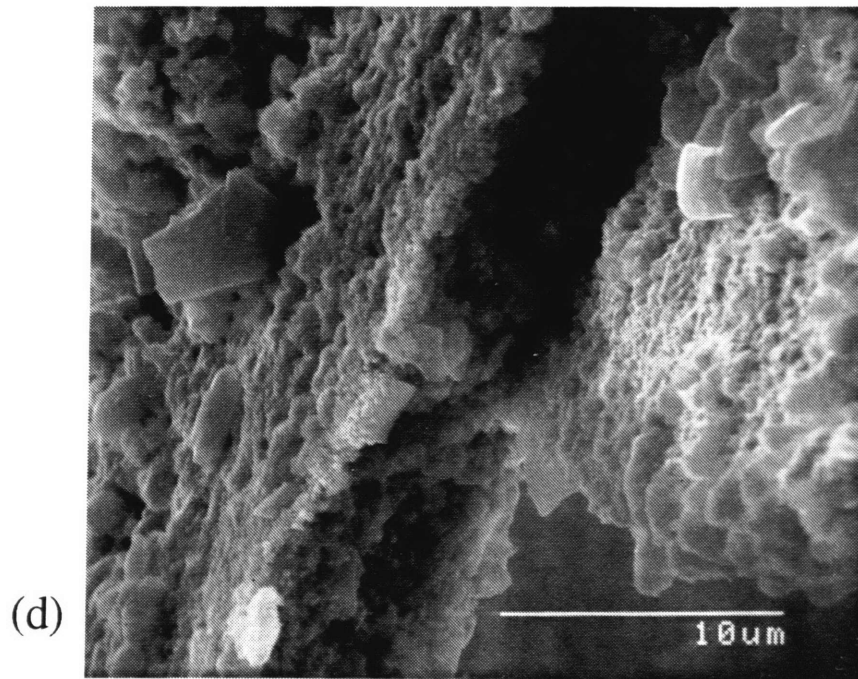
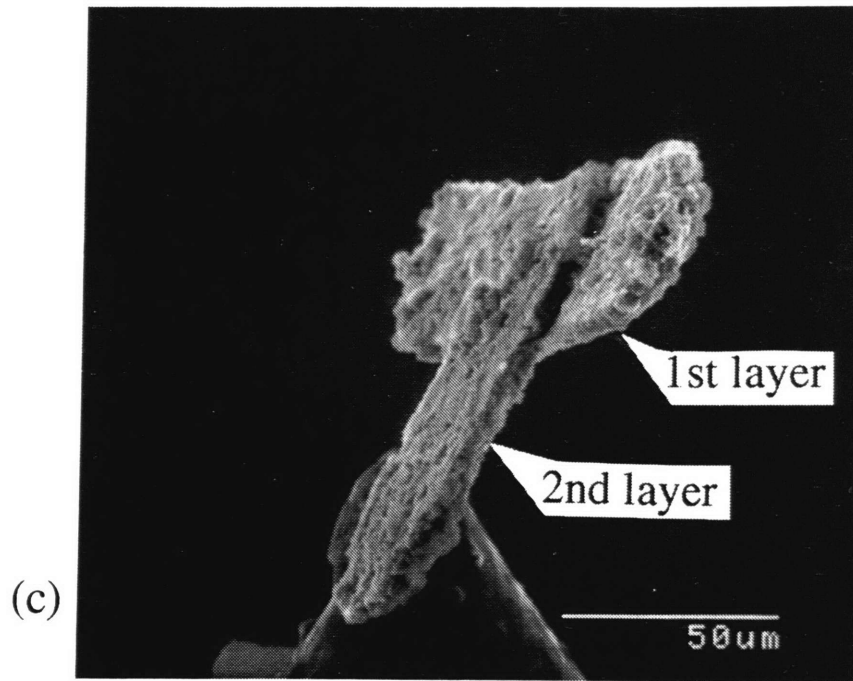


Fig. 8 (a) (b) (c) Stand-alone dual-layer part created by Sequential Photo-Electroforming; electroless Ni/SiC powder, photos taken from different angles (d) Closer view



The Cu/SiC lines in Fig. 4 were created at a laser power output of 0.8-1.0 W and a scanning speed of 530  $\mu\text{m}/\text{sec}$ , using a 12  $\mu\text{m}$  beam spot. It was found that a power as low as 0.3 W can create satisfactory lines of width 10 to 15  $\mu\text{m}$ .

Electroless plating on non conductive materials usually requires a stannous/palladium chloride pretreatment to activate the material surface (see Appendix 8), but it was found that laser enhanced electroless plating works on non pretreated SiC, while hot bath electroless plating does not. A possible explanation is that superheating of the material by the focused laser beam results in thermal activation of electroless plating (the laser superheating was investigated and is reported in section 4.1). This "laser activation" phenomena gives Photo-Electroforming great advantage, since no pre-activation is necessary and the second plating can be easily done. Demonstrative parts and line patterns as shown in Fig 5, Fig. 7 and Fig. 8 were created by utilizing this property. The lines in Fig. 4 were created at a laser power output of 1.2 W and a scanning speed of 5 cm/sec, using a 12  $\mu\text{m}$  beam spot. The square frame shown in Fig. 7(a) was created by laser enhanced electroless nickel plating. After the sample was patterned, it was immediately transferred into a bath of the same electroless nickel plating solution at a temperature of 75-85°C. Electroless nickel deposition continued on the square pattern, but not on the non metallized portion. This second stage joining lasted for 10 min. The sample was then cleaned in distilled water before being subjected to selective etching to lift the part. A boiling 20% potassium hydroxide solution was used as the selective etching agent which etches the silica holding the SiC substrate but does not attack the nickel. Fig. 7(b) is a closer view of the part. It shows 1  $\mu\text{m}$  SiC particles joined together by nickel deposition and a part thickness of about 8  $\mu\text{m}$ , which indicates that the laser induced metallization did penetrate to a depth of several particles as did the second stage electroless plating.

The simple dual-layer geometry shown in Fig. 8(a) was created following the process sequence to demonstrate the interlayer bonding. At the second layer, a layer of 10

$\mu\text{m}$  thick powder was spread manually on top of the first layer pattern, and then was dry pressed and fired. A closer view in Fig. 8(d) shows a layer thickness of about  $5\ \mu\text{m}$ . In general, a pre-press thickness of  $10\text{-}15\ \mu\text{m}$  resulted in  $5\text{-}10\ \mu\text{m}$  of after firing thickness.

Combining the capabilities of pattern formation, selective etching and interlayer joining, the basic elements for creating fully 3-D geometry are demonstrated.

### **3.2.2 Continuous Photo-Electroforming**

#### (1) Experiments

This approach makes use of a downward flow drag to hold powder particles on a porous base so the laser induced gas bubbles do not disturb the powder bed. Pressurization is required to force the solution to flow through the porous powder bed and can also reduce the size of gas bubbles thereby further decreasing the disturbing effect. A flow-through cell system was constructed to investigate issues of the Continuous approach. The cell contains a porous plug for powder deposition and windows for laser scanning and visual observation. Due to the complexity of the fully Continuous approach, simplified tests were carried out to investigate several fundamental physical issues,

- the uniformity of powder deposition,
- the effect of flow-through,
- interlayer bonding, and
- patterns and parts creation.

Spherical nickel powder of  $5\ \mu\text{m}$  size was used as layer material because it is self-catalytic for electroless Ni plating and therefore no pretreatment was necessary, also because this particle size requires only a moderate pressure to create the necessary flow drag. The powder deposition was done discretely while the flow stopped for simplicity.

## (2) Results

Very crude single layer parts and patterns were created. Fig. 9 shows a short bar created by directly joining the nickel particles with laser induced electroless nickel plating. A 12  $\mu\text{m}$  focused argon laser beam of 0.3 W was scanned at 5  $\mu\text{m}/\text{sec}$  to create this short bar. The chamber pressure was 100 psi and the flow rate was about 8 cm/sec. Fig. 10 shows patterns created on a powder bed. To assess the ability for multi-layer parts, inter-layer joining was demonstrated by bonding a single layer pattern to a substrate made of the same Ni powder, as shown in Fig. 11. Both Fig. 10 and Fig. 11 were created by the dual beam setup (described below), with a total laser power of 0.8 W, scanning speed 2  $\mu\text{m}/\text{sec}$ , chamber pressure 150 psi, and the flow-through speed of 5 cm/sec.

To create a smooth powder bed, the powder deposition was done by spreading the particles through a long tube filled with water before they reached the porous plug. Brownian motion spreads the particles more evenly during the passage through the tube.

It was found that a minimum chamber pressure of 70 psi and a flow velocity of 5 cm/sec is required to hold the 5  $\mu\text{m}$  particles, for laser power no larger than 0.3 W, with a 12  $\mu\text{m}$  beam size. The corresponding flow drag per unit area over the powder bed was estimated to be about 1 KPa. The flow drag was estimated by using Stoke's law of flow drag over a sphere, [Gerhart & Gross 1985]

$$D_p = 3\pi\mu(2R)U_o,$$

where  $\mu$  is fluid viscosity,  $R$  is particle radius, and  $U_o$  is flow-through velocity; and drag per unit area was estimated by

$$D_p / \pi R^2 = 6\mu U_o / R.$$

A whisker structure was frequently observed during the process, as shown in Fig. 12. It was determined that a continuous laser exposure at the tip of any protruding deposits might cause a continuous growing of a whisker, as the laser heats the tip most effectively.

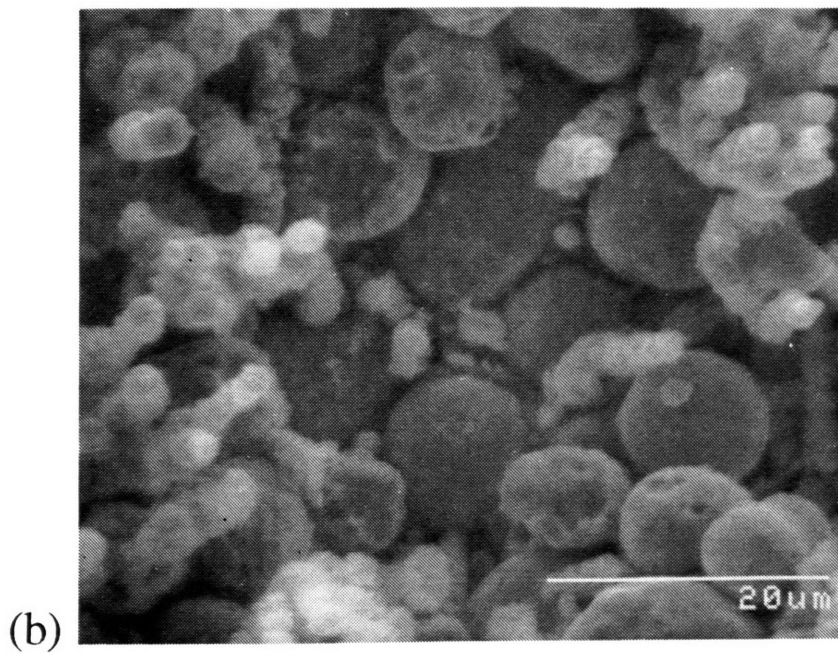
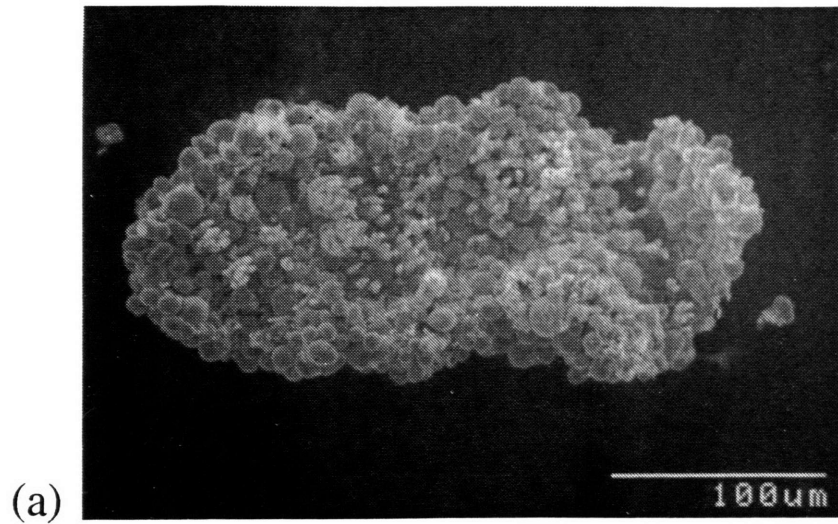


Fig. 9 (a) Stand-alone single-layer part created by Continuous Photo-Electroforming; electroless Ni/Ni powder (b) Closer view



Fig. 10 Simple patterns created by Continuous Photo-Electroforming on the Ni powder bed; electroless Ni

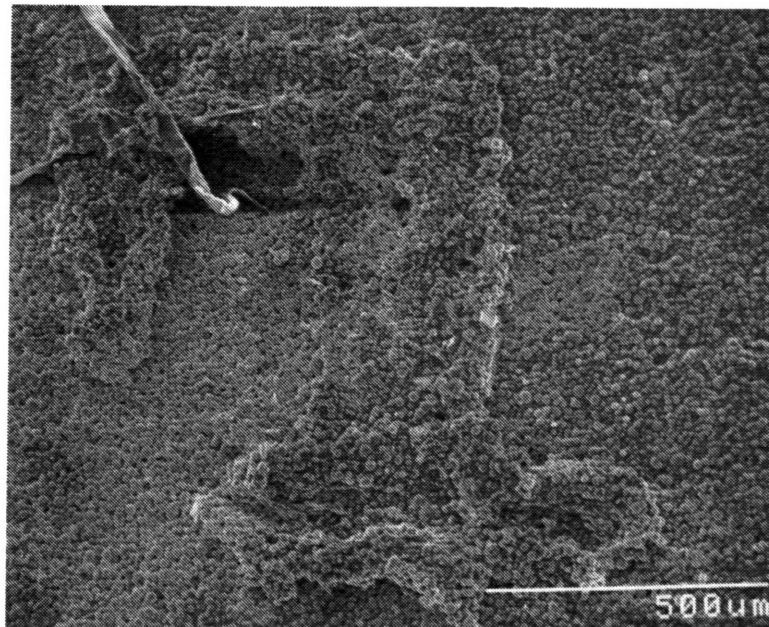
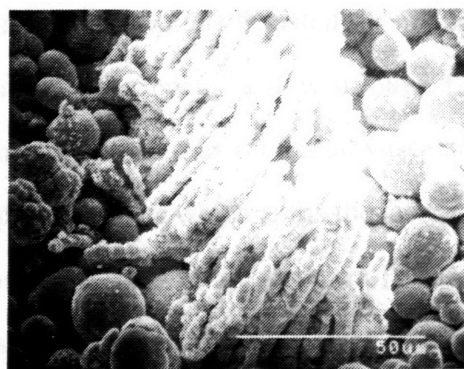
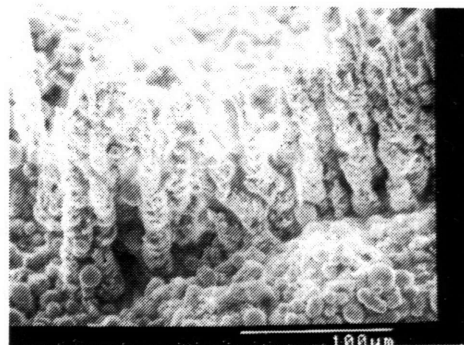


Fig. 11 A single-layer pattern joined to a base of Ni powder; Continuous Photo-Electroforming; electroless Ni/Ni powder



10 μm

**Fig. 12**  
**Whisker structures formed by single beam**  
**Continuous Photo-Electroforming; electroless Ni/Ni**  
**powder**

It was estimated that the focused laser beam of 12  $\mu\text{m}$  spot size had a depth of focus, if defined at 5% spot radius increase from the beam waist, greater than 50  $\mu\text{m}$  (see Appendix 1 for details of laser optics). Therefore, a laser power density close to full power density at the beam waist extended longer than 50  $\mu\text{m}$  in the vertical direction. This extended full power zone explains the continuous heating and forming of long whiskers. The whisker diameter observed varied from several micrometers to tens of  $\mu\text{ms}$ , and the length was from 50 to 200  $\mu\text{m}$ . Higher cell pressure tends to create finer whiskers. In the case where there is no flow-through, whiskers were not usually observed. It is speculated that bubble formation, local boiling and upward bubble detaching could destroy the continuous growth of long whiskers, while in the presence of a flow-through field, boiling and bubble size was suppressed and bubble detaching was forced downstream so that continuous growth became possible. An improved optics which splits the laser beam and then brings them to intersect each other at their focal points, as shown in [Fig. 13](#), solved this problem. The dual beam setup reduces the full power heating zone to a confined dimension which is much smaller than the depth of focus of the single beam setup, as illustrated in the figure.

### **3.2.3 Conclusion**

From above results, it is concluded that both the Sequential approach and the Continuous approach are feasible in terms of making fully 3-D geometry. To distinguish the pros and cons of both approach, the mechanism and process characteristics must be investigated.

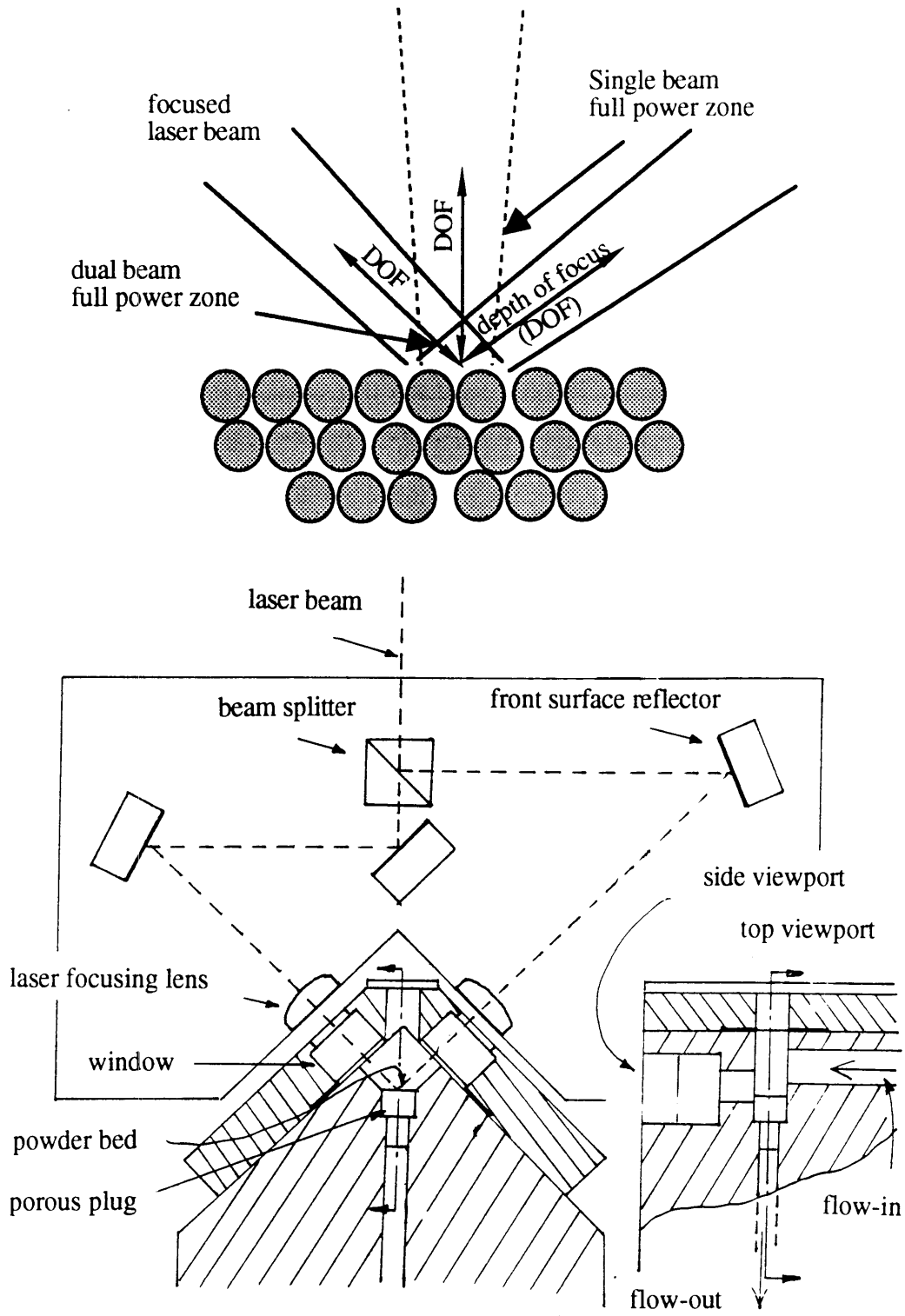


Fig. 13 Dual-beam concept and its setup

## **4. Process Mechanism Understanding**

This chapter discusses the possible mechanism and major issues of laser induced electroless plating, which is important for understanding the basic process characteristics of Photo-Electroforming. The major issues that may affect the process characteristics, especially rate and resolution, are surface temperature, rate controlling mechanism, and gas bubble effect. The investigation presented in this chapter is mainly for laser induced electroless plating in an open bath. The Continuous Photo-Electroforming is more complicated, since a pressurized flow field is involved, but can be understood in a comparative base by using the open bath cases as a reference.

### **4.1 Surface Temperature: Ni-glass experiments**

A first understanding of the surface temperature during laser induced electroless plating was estimated from thermal conduction models, which indicates that a focused laser beam can heat up the material surface to a very high temperature within a very short time. Fig. 14 shows the calculated surface temperature increase with time, estimated by a pure conduction model and a conductive-convective model (see Appendix A4 and A5 for details of the models), on two typical samples used in this work, heated by a 12  $\mu\text{m}$  laser beam of 0.1 W. The estimation shows that the focused laser beam can easily heat up the sample surface to several hundreds of degree C in less than fractions of a millisecond. This estimation is supported by the observation of melting of various materials during laser induced electroless plating experiments, such as polymer targets and nickel film coated glass.

Since to measure the surface temperature directly under the laser beam in-situ the photo-metallization process may require a technology beyond the scope of this work, an indirect approach of observing the morphology of nickel-film on glass slides at known temperatures was used to estimate the surface temperature. The test samples were prepared

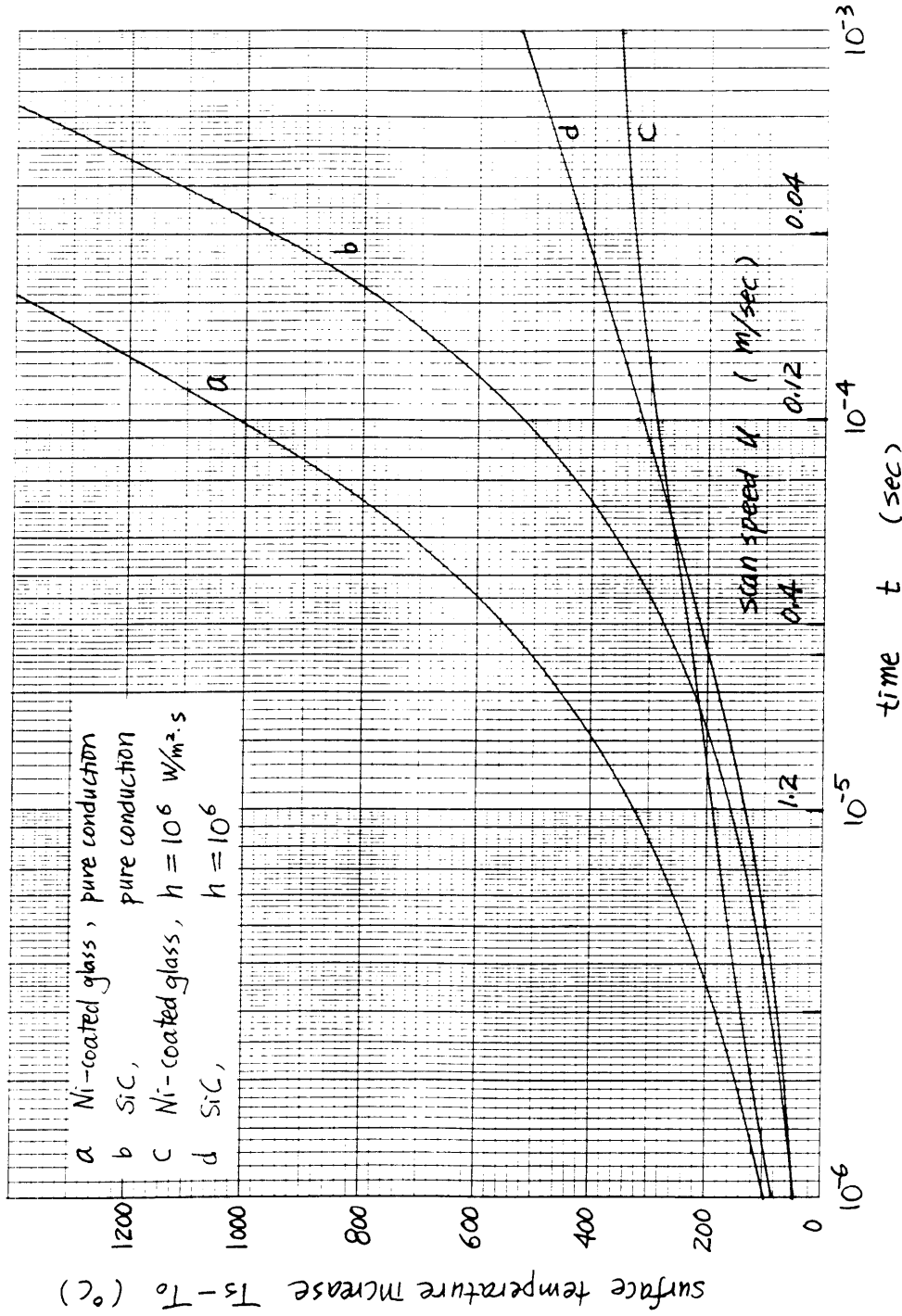


Fig. 14 Surface temperature increase estimated by pure conduction model and by conductive-convective model; power 0.1 W, beam size 12 $\mu\text{m}$  (see Appendix A4 & A5 for details of model)

by sputtering 0.2  $\mu\text{m}$  thick Ni film on glass slides. Nickel was used because of its selfcatalytic property of accepting electroless Ni plating. A laser beam was scanned over the Ni-glass sample immersed in the electroless Ni plating solution at different power outputs to create lines of deposition, as shown in [Fig. 15](#). The scanning was done both on the back and the front side using a turn table. [Fig. 16](#) illustrates the setup. Lines of nickel deposits, in the form of tiny white dots in the SEM photos, were observed in scans where laser power was higher than 0.16 W (corresponding to an apparent power density of about 1  $\text{GW}/\text{m}^2$ ). Laser power density lower than this value did not create visible lines at this scanning speed, 6.28  $\text{cm}/\text{sec}$ . The estimated peak surface temperatures at different laser powers is shown in [Fig. 17](#). This estimate is based on the following observations:

- The melting of Ni-film, as shown in photo 1.0 W in [Fig. 15\(b\)](#), means a peak surface temperature was at least at the melting point; 1425 C of Ni.
- The starting of the deformation of Ni-film, as shown in photo 0.24 W in [Fig. 15\(a\)](#), as compared to the undeformed case of photo 0.16 W, is taken as the onset of material recrystalization. Therefore, the temperature was at least 375 C, the recrystalization temperature of nickel [[Metals Handbook 1979](#), pp. 777].
- The temperature increase corresponding to power zero is zero.

The deformation of Ni-coating requires more explanation. Firstly, when a metal, such as nickel or iron, is heated up, it first reaches recovery temperature, where the dislocations in the material microstructure adjust their positions and the internal stress is released, and then it reaches the recrystalization temperature where crystal grains change their boundaries and start growing [[Smith 1981](#)]. Secondly, because of continuous hydrogen gas bubble formation and evolution caused by the laser scanning, the material surface must be frequently subjected to quenching by the solution. It seems that recrystalization causes a possible local volume change of the Ni-film, and a subsequent quenching of the material caused film detachment and deformation. If this is correct, then the starting of Ni-film deformation can be viewed as sign of recrystalization temperature. This temperature estimation was confirmed in a separate simulation experiment. Ni-glass samples were

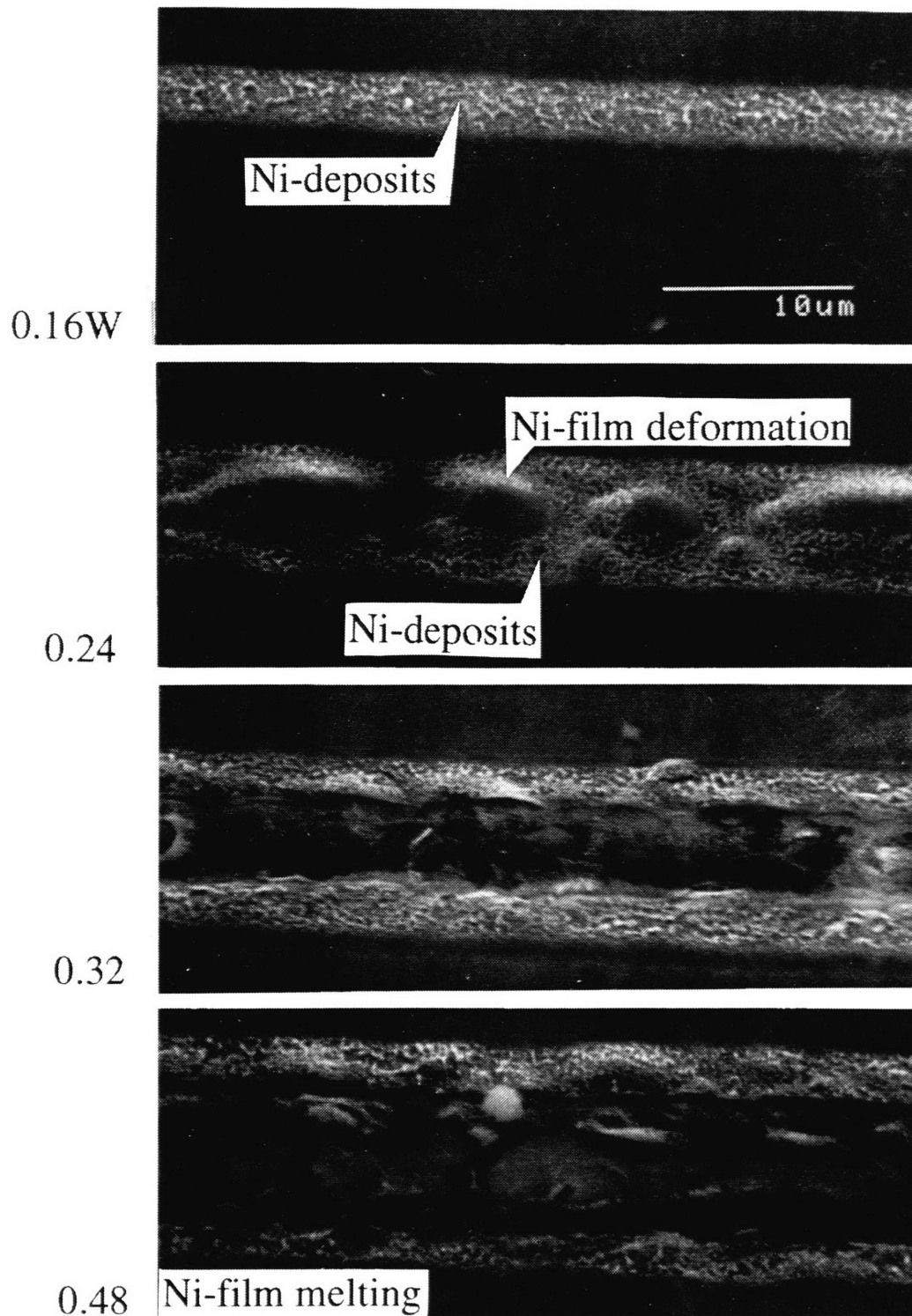


Fig. 15(a) Lines created by laser induced electroless Ni plating on sputtered Ni-film on glass at different power; back scan speed 6.28 cm/s; Ar<sup>+</sup> laser; beam size 12 μm; 45° view

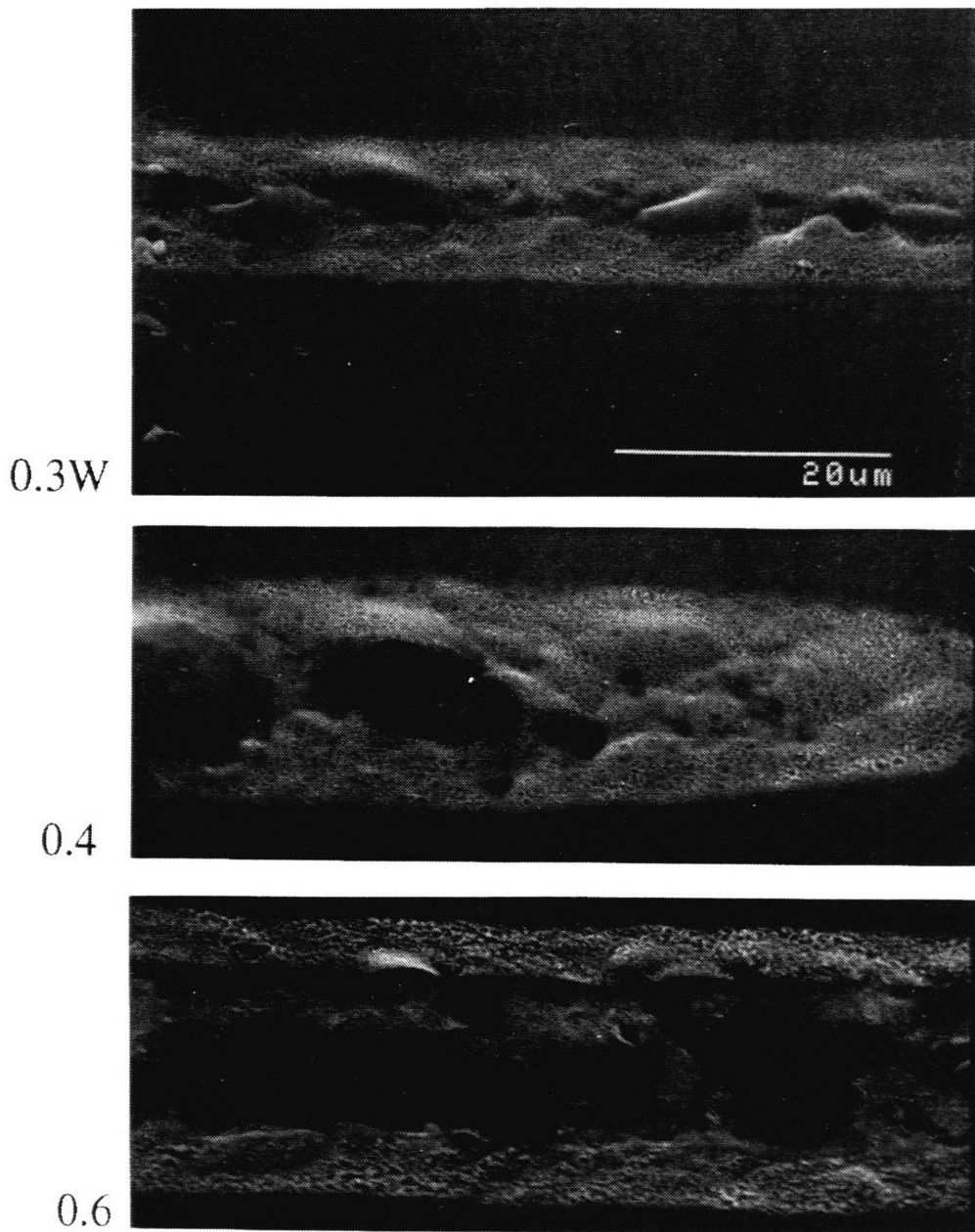
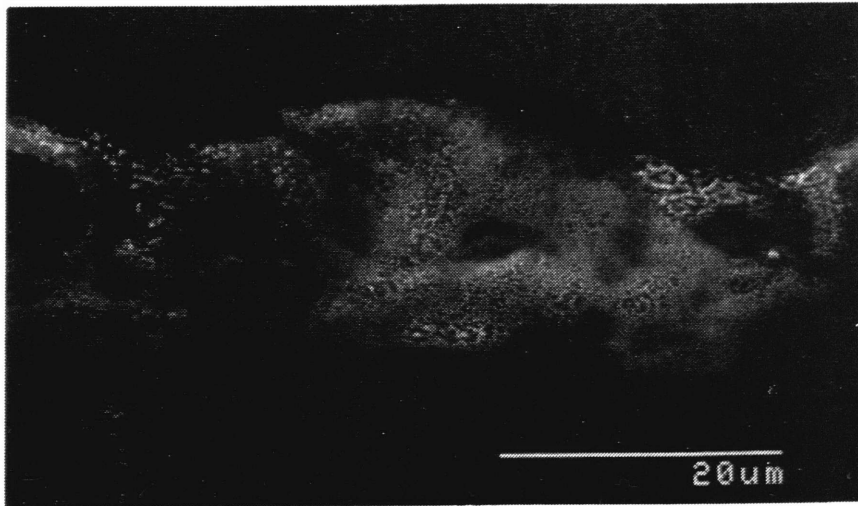


Fig. 15(b)

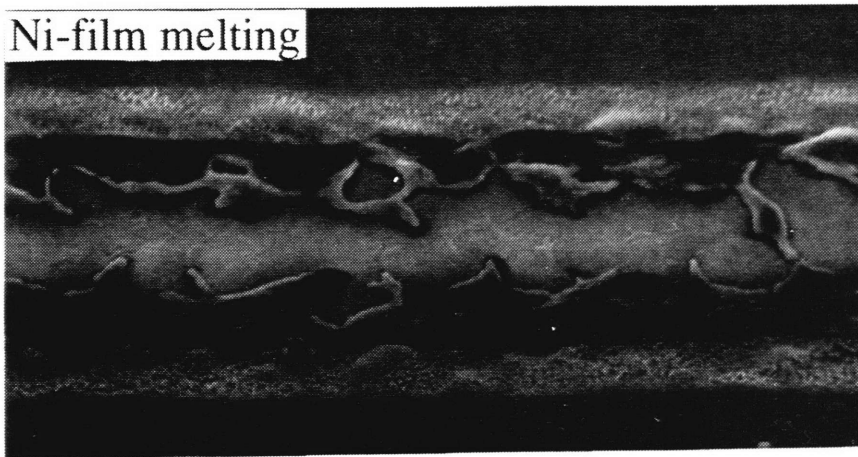
Lines created by laser induced electroless Ni plating on sputtered Ni-film on glass at different power; front scan speed 6.28 cm/s; Ar<sup>+</sup> laser; beam size 12 μm; 45° view

0.8W

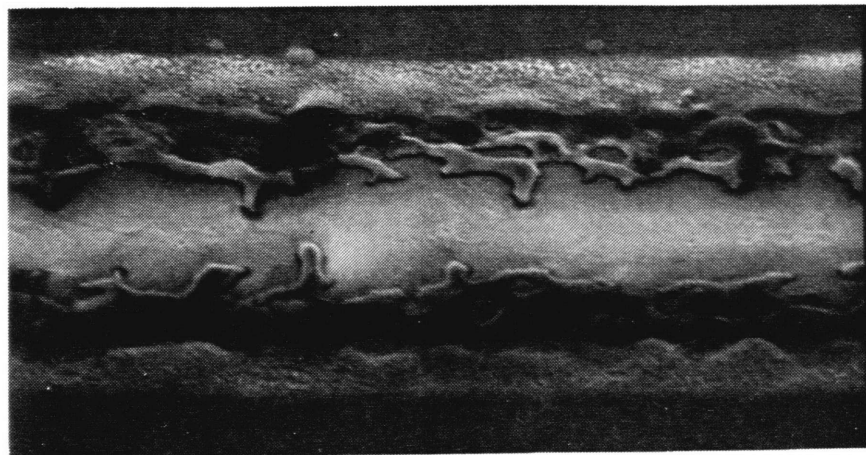


Ni-film melting

1.0



1.2



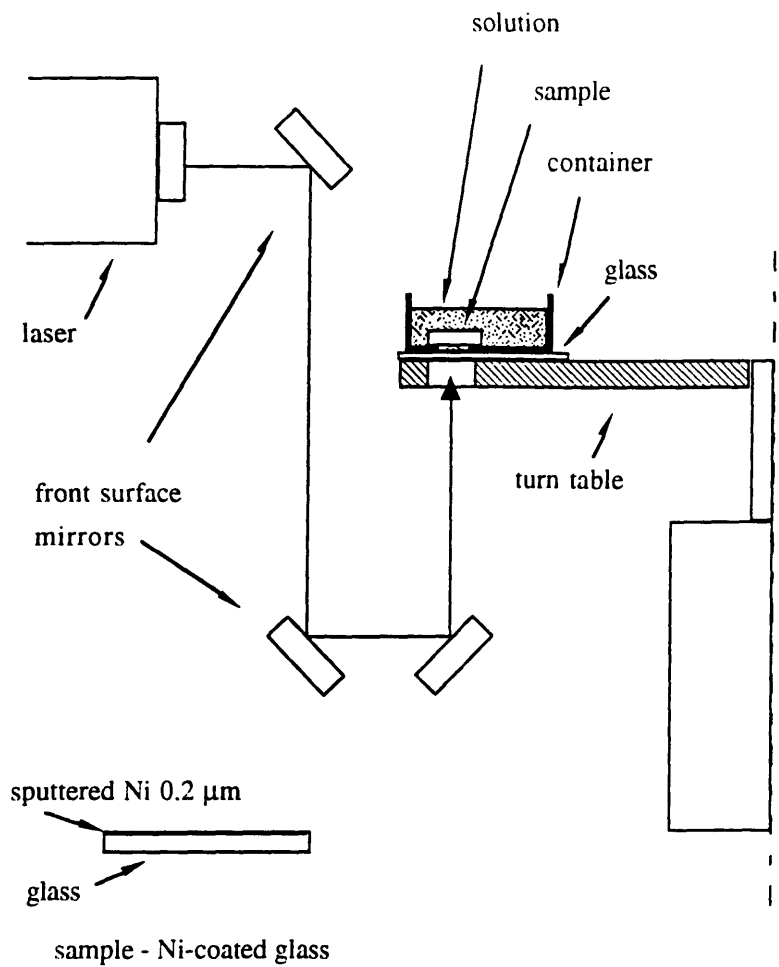


Fig. 16 Turn table setup for scanning test

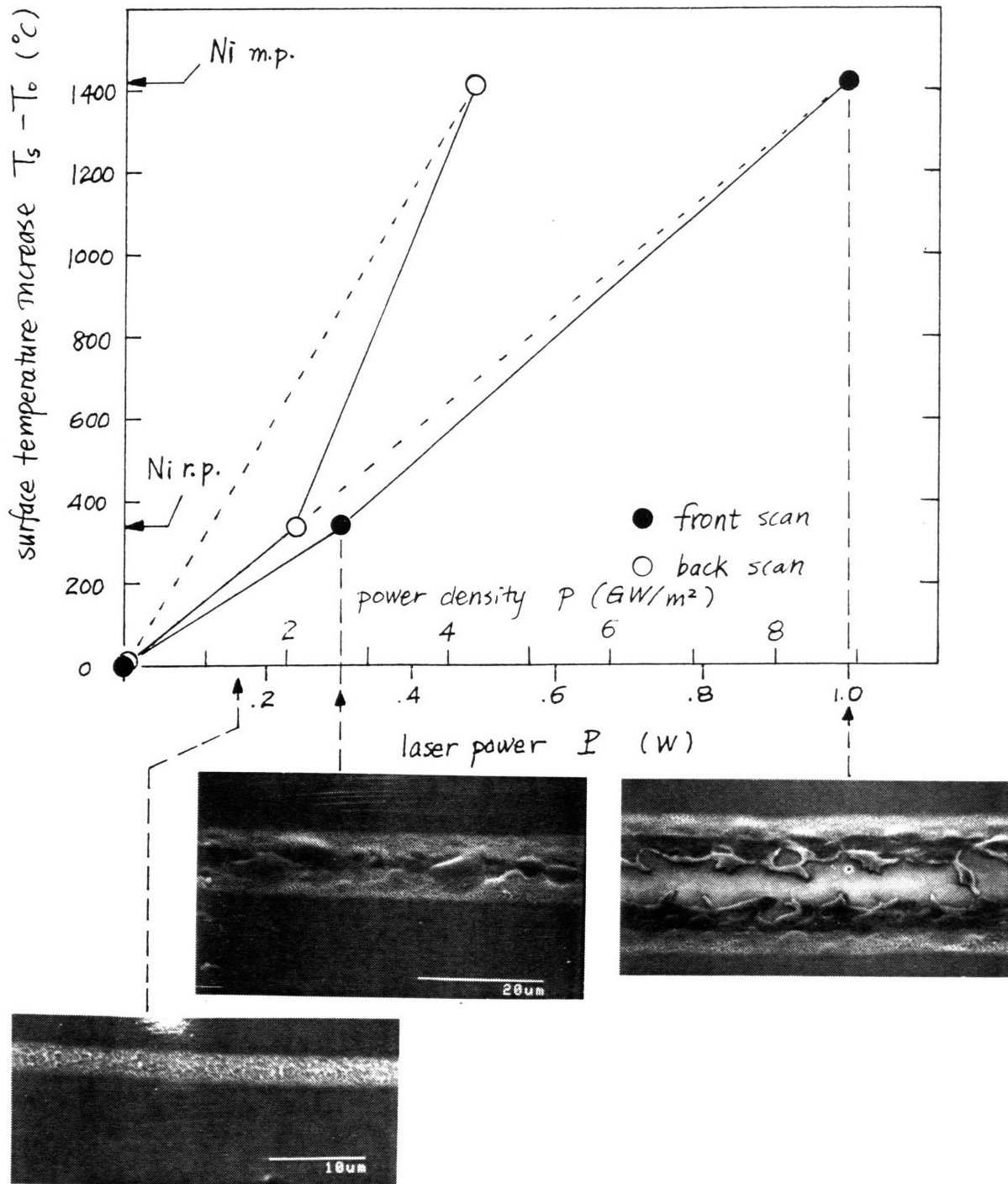


Fig. 17

Experimental surface temperature increases on Ni-coated glass; back scanning and front scanning; estimated by surface morphology observation

heated to different temperatures in air in a furnace and then were quickly dropped into water at room temperature. The morphology was observed and compared. Only when the sample was heated over 500 C, a deformation morphology similar to that induced by laser was observed after water quenching, as shown in [Fig. 18](#). As a result, it is believed that [Fig. 17](#) is quite a reasonable estimate of the temperature to laser power relation of the Ni-film experiment.

To estimate the surface temperature of the silicon carbide samples, used in the demonstrative experiments in chapter 3, under laser enhanced electroless plating is more difficult since morphology observation may not work. However, a reasonable estimation can still be done after more insights of the process mechanism were obtained. The estimation of SiC surface temperature under laser enhanced electroless plating is discussed later in section 4.4.

## **4.2 Deposition Rate Controlling Mechanism**

It has been speculated that the process of laser enhanced electroless plating is mass transfer controlled. Microscopic observation shows thickness of deposits does not change significantly over the range of laser power tested, given similar other conditions, as shown in [Fig. 15](#), laser induced electroless Ni on Ni film, as well as on [Fig. 19](#), laser induced electroless Ni on SiC. Similar phenomenon was also observed in laser induced electroless Cu plating on AlN samples, as reported by [Morita et al. 1989]. To determine if the process is mass transfer limited (diffusion-controlled) or is controlled by surface reaction rate (activation-controlled), the effect of both temperature and mass transfer condition on the deposition rate was investigated.

### **4.2.1 Temperature Effect**

The experimental results of temperature effect on laser enhanced deposition is summarized in [Fig. 20](#). These data were summarized from the Ni-film experiments. The

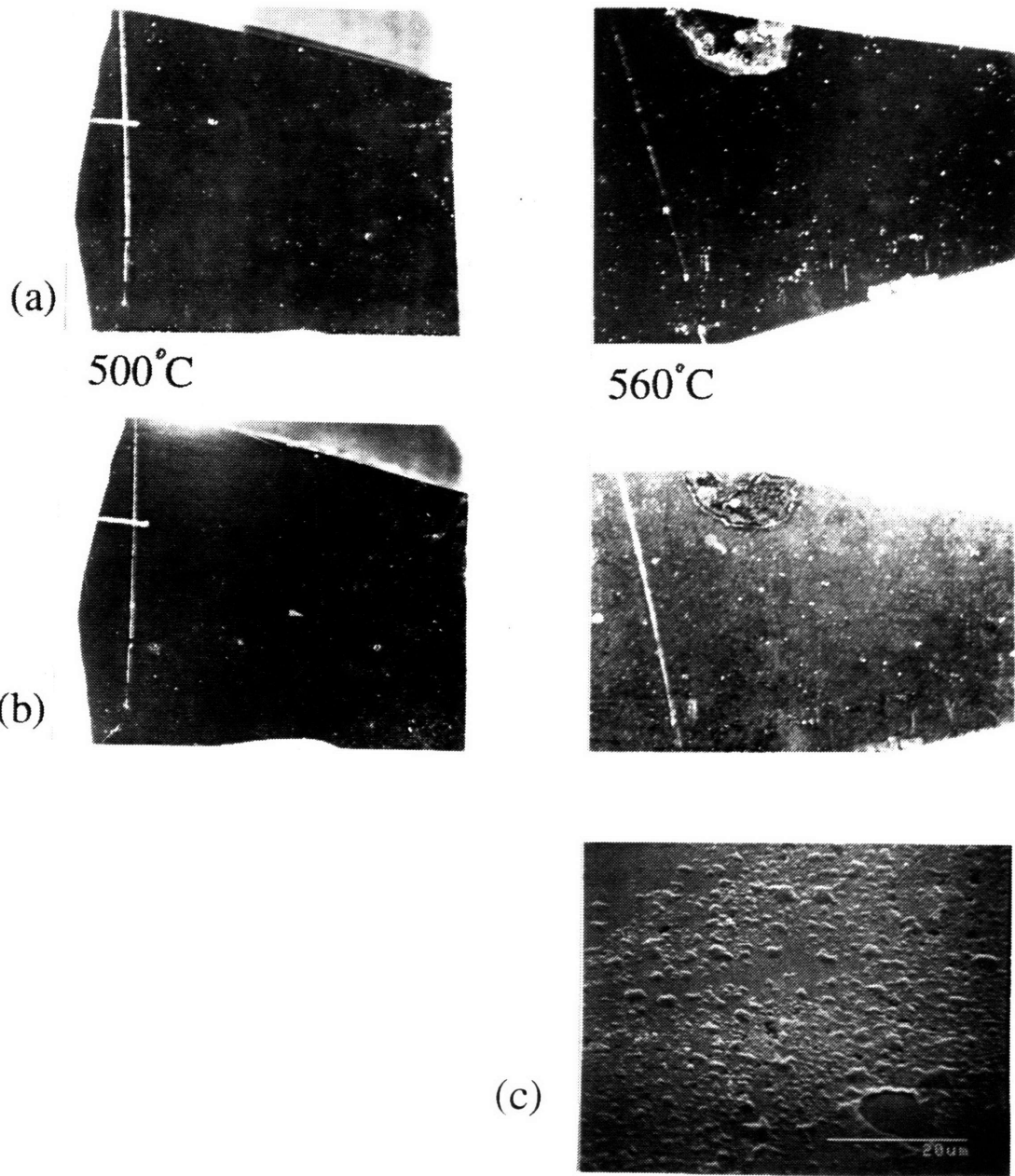


Fig. 18

(a) Ni-coated glass before test; (b) after firing followed by water quench; (c) SEM of the 560°C case; coating deformation

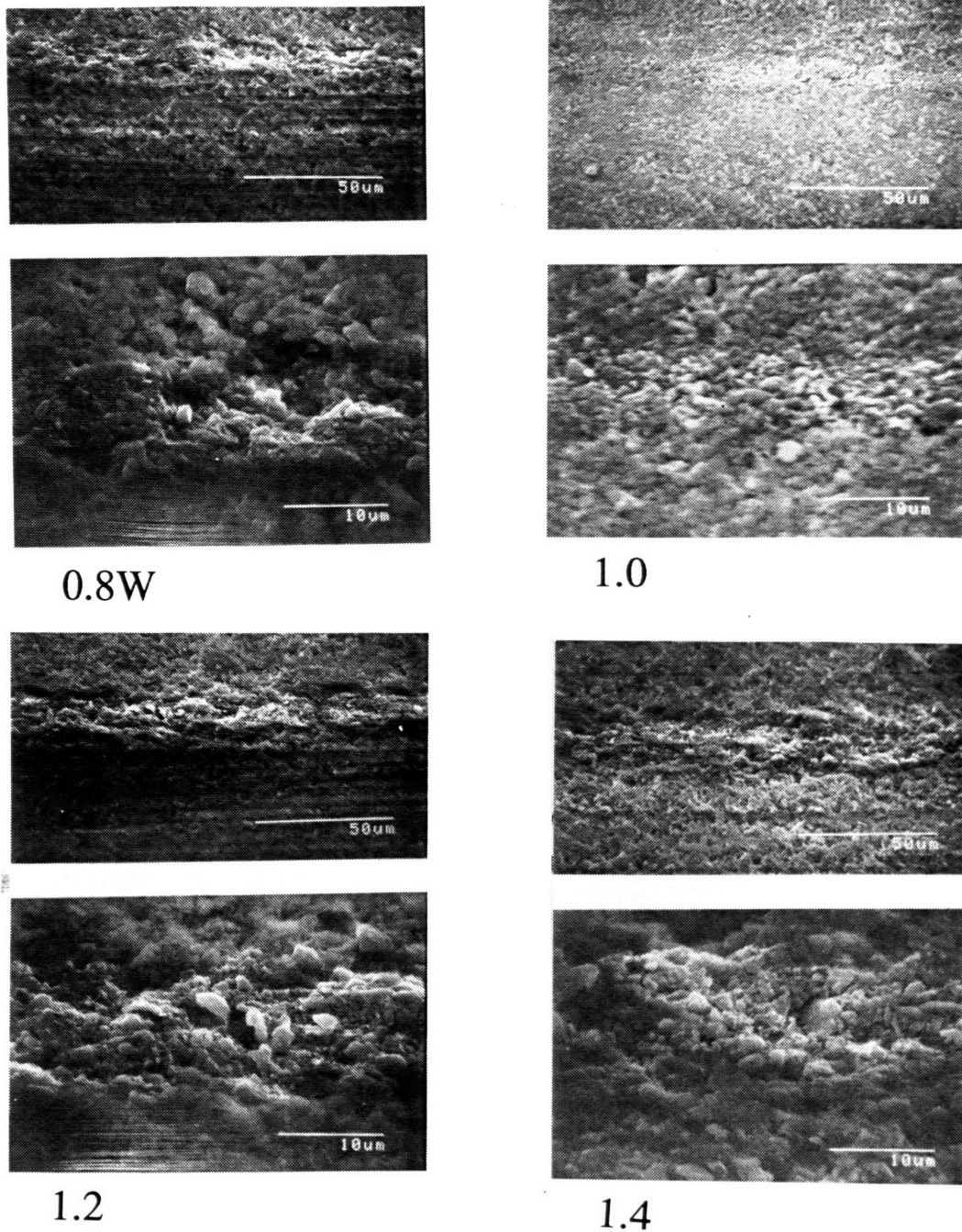


Fig. 19

Close-up of lines created by laser enhanced electroless Ni on SiC pellet at different power; scan speed 5cm/s; Ar laser; beam size 12 µm

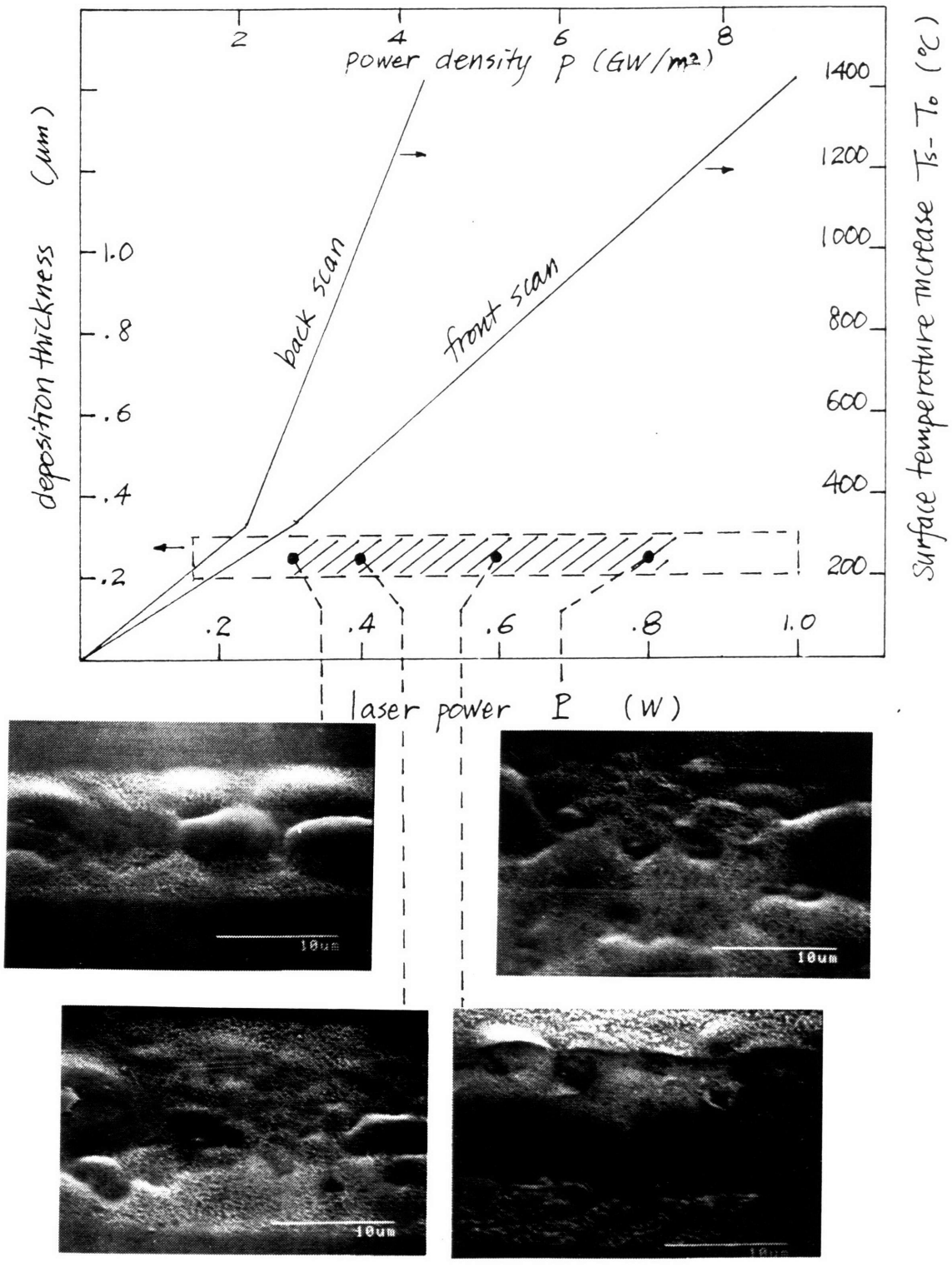


Fig. 20 Deposition thickness of laser induced electroless Ni on Ni-coated glass at different powers; scan speed 6.28 cm/s; Ar laser; beam size 12 μm; 45 view

range of deposition thickness was obtained by measuring the size of Ni deposits granules (white tiny dots) on the Ni-film, as shown in the inserted SEM photographs in Fig. 20. The results suggest that the temperature effect on deposition thickness is not significant.

It can be deduced, from above results, that the temperature effect on deposition rate is also insignificant. To obtain the deposition rate from the above thickness results is somewhat difficult, because the total deposition time at one spot on the line is unknown, which can be much longer than the laser exposure time because of a slow cooling period after laser exposure. However, a qualitative analysis shows that higher laser power should give longer total deposition time, since the peak temperature obtained is higher and the corresponding cooling period is longer. This is illustrated in Fig. 21. Therefore, higher laser power gives higher average temperature and longer plating time. This qualitative observation is true even the heat transfer condition may vary with temperature. Knowing that deposition thickness does not change significantly, it can therefore be deduced that deposition rate does not increase with temperature over the range of laser power tested.

Comparing the above results with the temperature sensitivity of the reaction rate constant of electroless plating, it was found that the deposition rate is not controlled by the known kinetics. According to previous researchers [Pearlstien 1974, Gutzeit 1959], the activation energy of nickel formation in standard electroless nickel plating is,

$$E_a = 14,000 \text{ cal/mol,}$$

over the temperature range from room temperature to 100 C. If mass transfer does not limit the deposition rate, then the deposition rate variation with temperature should follow the trend of reaction rate constant  $k$ , since

$$\text{Ni deposition rate} = k [\text{H}_2\text{PO}_2^{2-}] = [\text{H}_2\text{PO}_2^{2-}] A e^{-E_a/RT}$$

by Arrhenius law. The temperature sensitivity of this deposition rate is illustrated in Fig. 22, where the rate increases more than two order of magnitudes with increasing laser

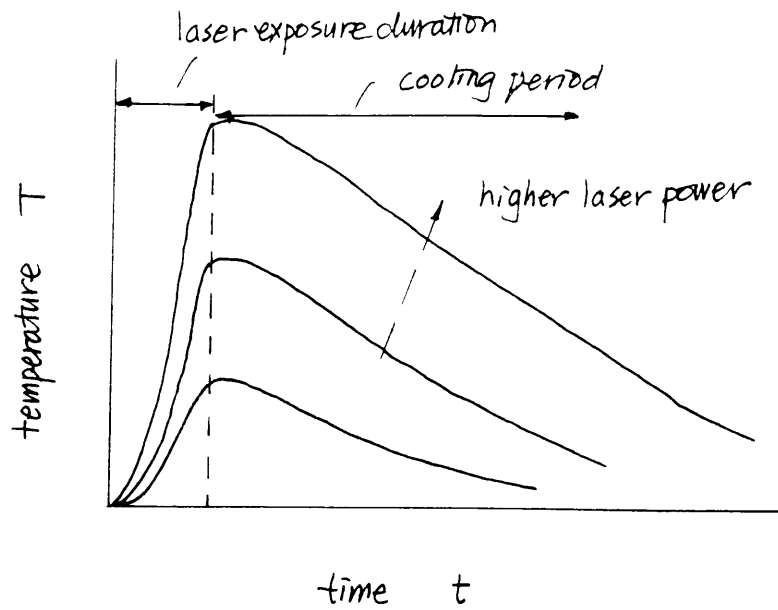


Fig. 21

Qualitative temperature history in laser enhanced electroless plating at different powers; indicating total plating times

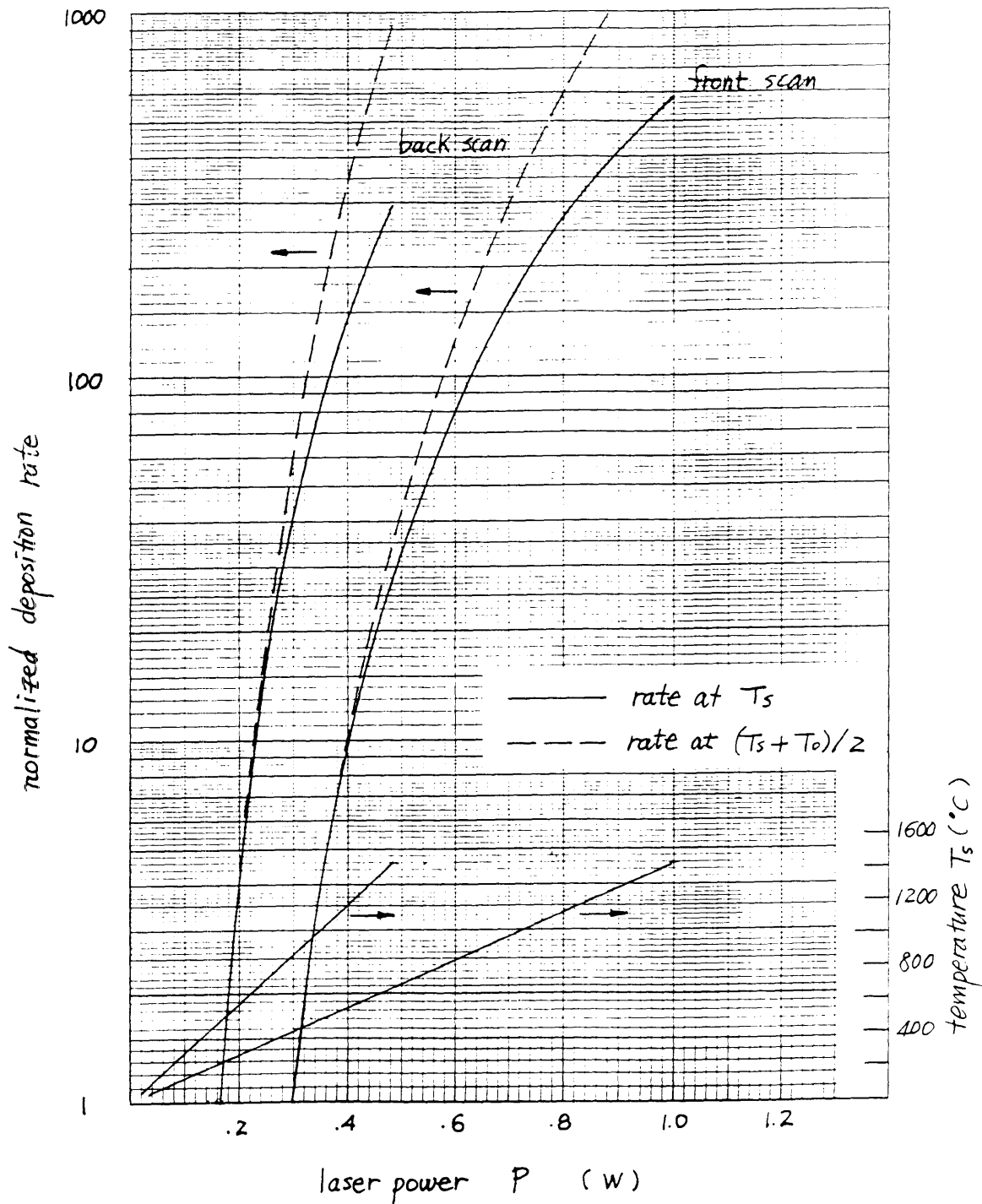


Fig. 22 Temperature sensitivity of electroless Ni deposition rate; assuming known low-temperature reaction mechanism valid, laser power to temperature relation taken from Fig. 16

power. This stands in contrast to the above experimental results. Therefore, either the deposition rate is controlled by mass transfer or the laser enhanced electroless plating has a different mechanism with a very small activation energy.

#### **4.2.2. Mass Transfer Effect**

To further understand the process mechanism, the laser enhanced deposition rate of electroless nickel was investigated. As mentioned previously, the total deposition time at any spot on the laser path contains a laser exposure period followed by a cooling period, as illustrated in [Fig. 23](#). The laser exposure period can be estimated from scan rate, while the cooling period depends on heat convection transfer which is difficult to estimate. This cooling period changes not only with laser power but also with the length of exposure period. To avoid the difficulty of estimating the nickel deposition rate and the length of cooling period at high scan speeds, experiments at low scan speeds were performed to estimate the cooling period and to measure the deposition rate. [Fig. 24](#) shows the time periods of continuing gas bubble generation after a one second laser exposure on silicon carbide pellet samples. Continuous gas bubble forming was observed after the laser was turned off, as an example shown in [Fig. 25](#). The average cooling period of this one second shot is 2.5 second, quite independent of laser power. The deposition rate was then estimated by measuring the thickness of nickel deposits at a slow scan speed, which gives a laser exposure time close to 1 sec, and averaging the thickness over the entire plating period. The results is shown in [Fig. 26](#). Some photos of the deposited lines are shown in [Fig. 27](#). It can be seen that the nickel deposits were mostly granules of several micrometers, and occasionally spikes of about 20  $\mu\text{m}$  high formed. In conclusion, the laser enhanced electroless plating has an averaged rate of 0.6 - 3  $\mu\text{m}/\text{sec}$ , and an occasional spike forming rate of 6 - 10  $\mu\text{m}/\text{sec}$ , quite independent of laser power, for laser power density from 1 to 10  $\text{GW}/\text{m}^2$ .

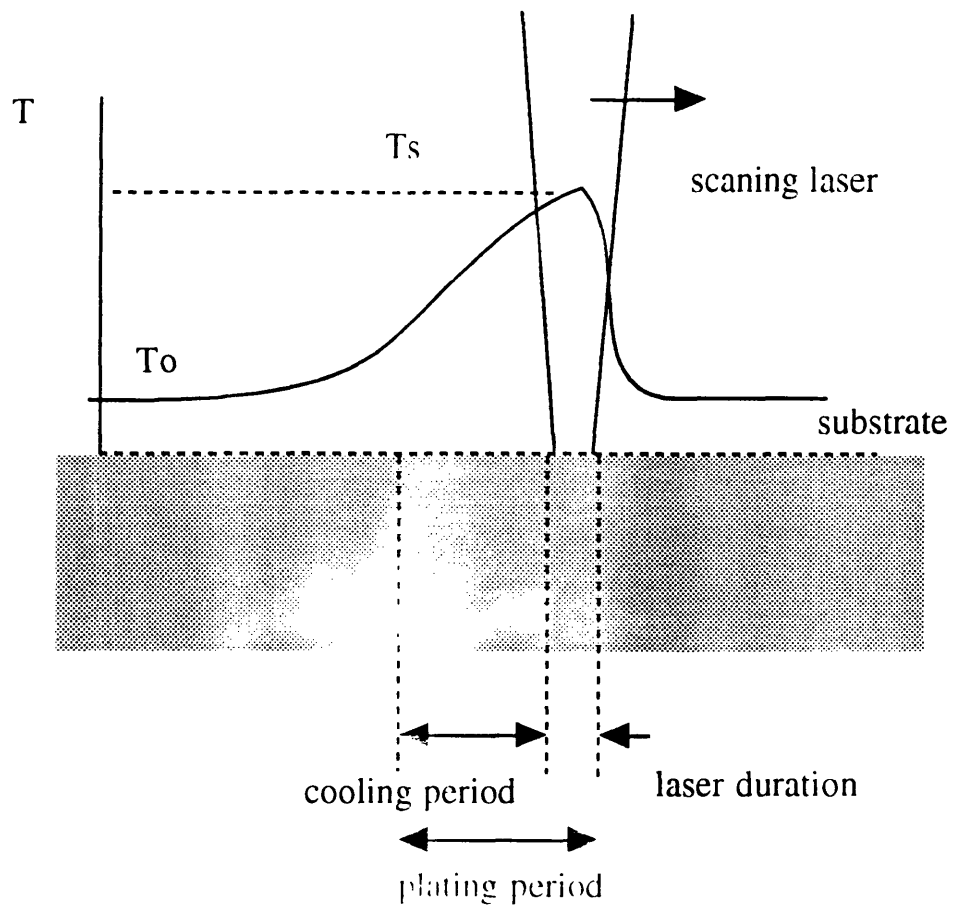


Fig. 23 Qualitative surface temperature profile indicating laser exposure duration and cooling period

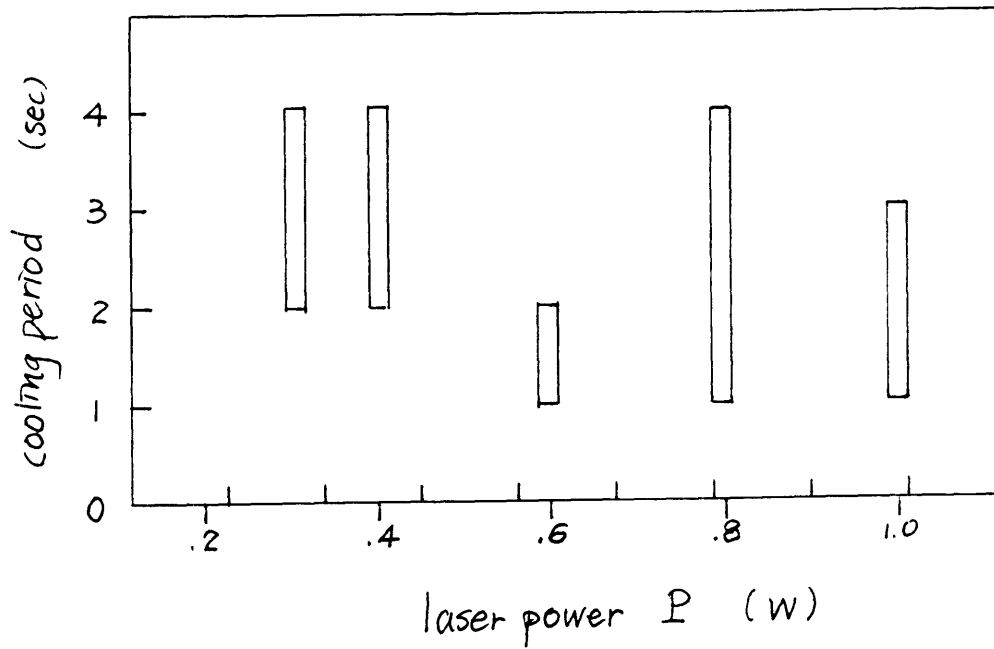
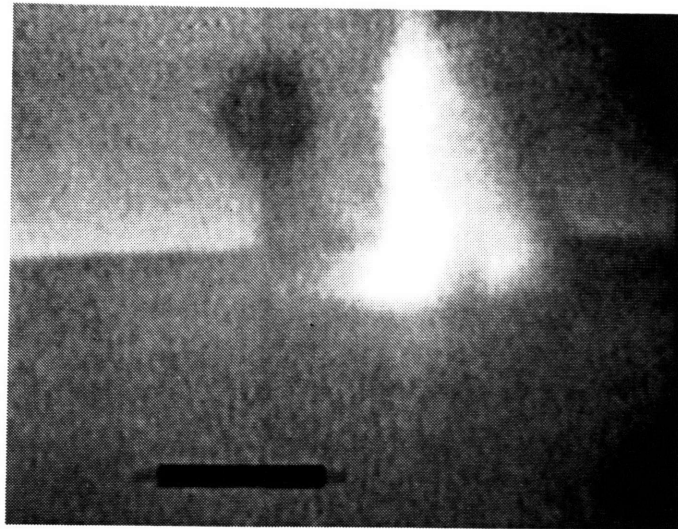
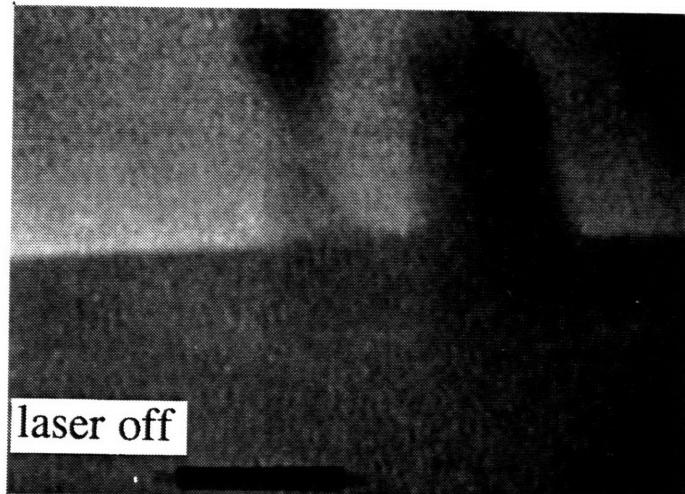


Fig. 24

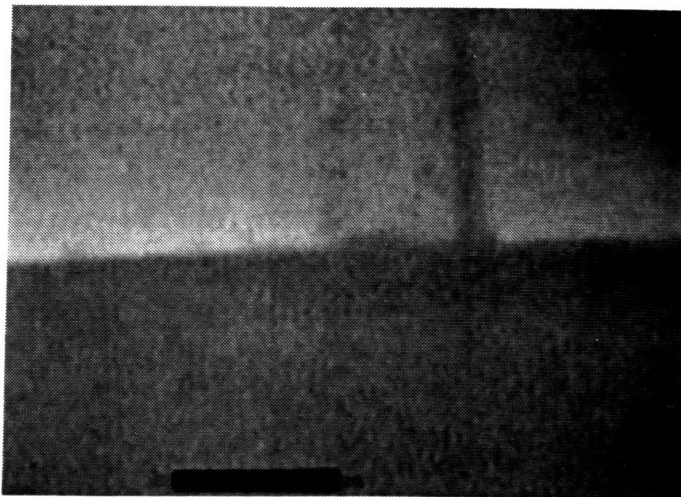
Observed cooling period on SiC pellet; 1-sec Ar laser shots at different power; beam size  $12 \mu\text{m}$



25/30 s



26/30



45/30

Fig. 25 Continuing deposition in cooling period, in-situ observation of stationary laser exposure on SiC pellet in electroless Ni solution; laser power 0.8W, beam spot 12  $\mu\text{m}$ , scale bar 250  $\mu\text{m}$

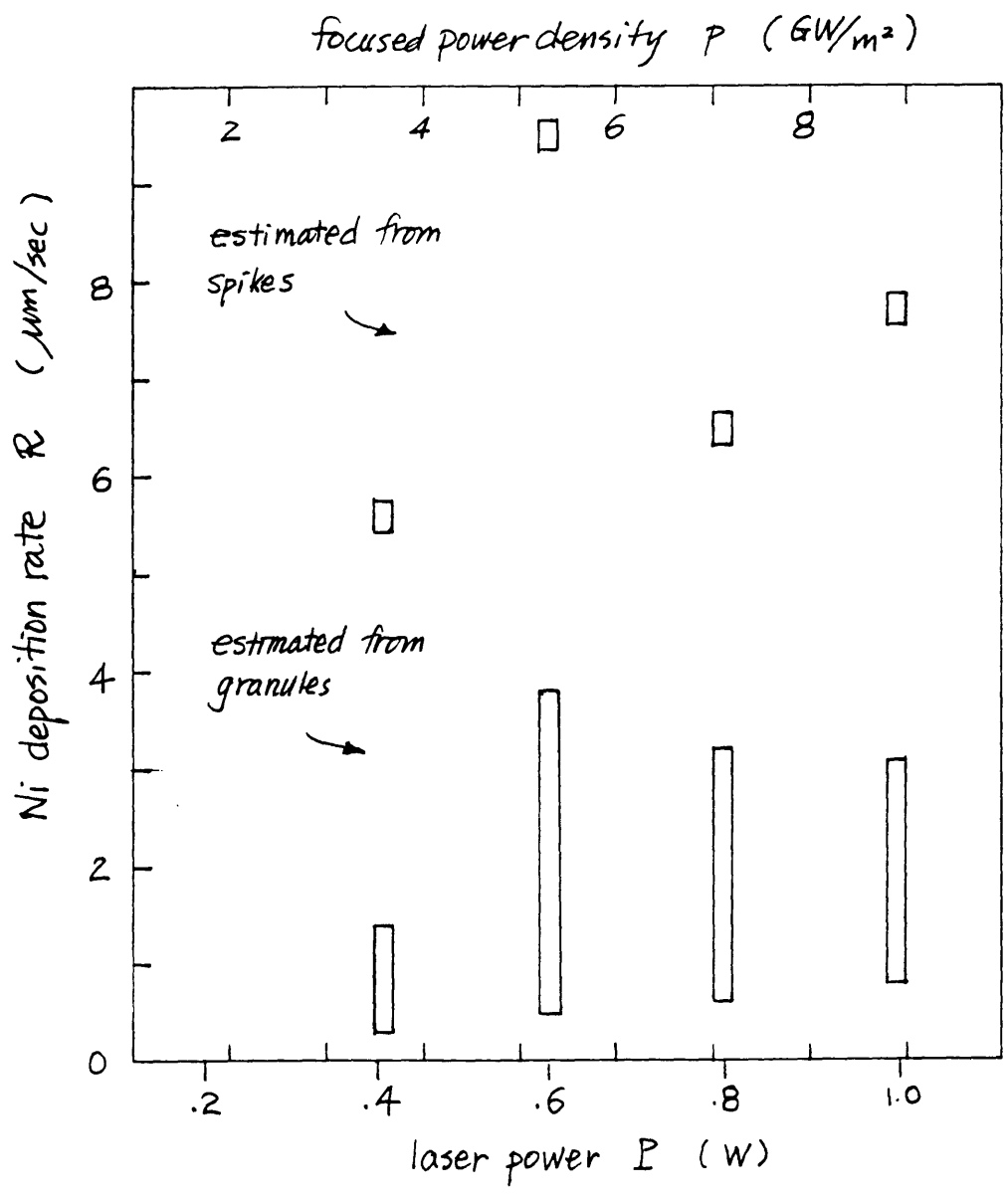


Fig. 26

Experimental laser induced electroless Ni deposition rate; estimated from cooling period observation and deposits sizes on SiC

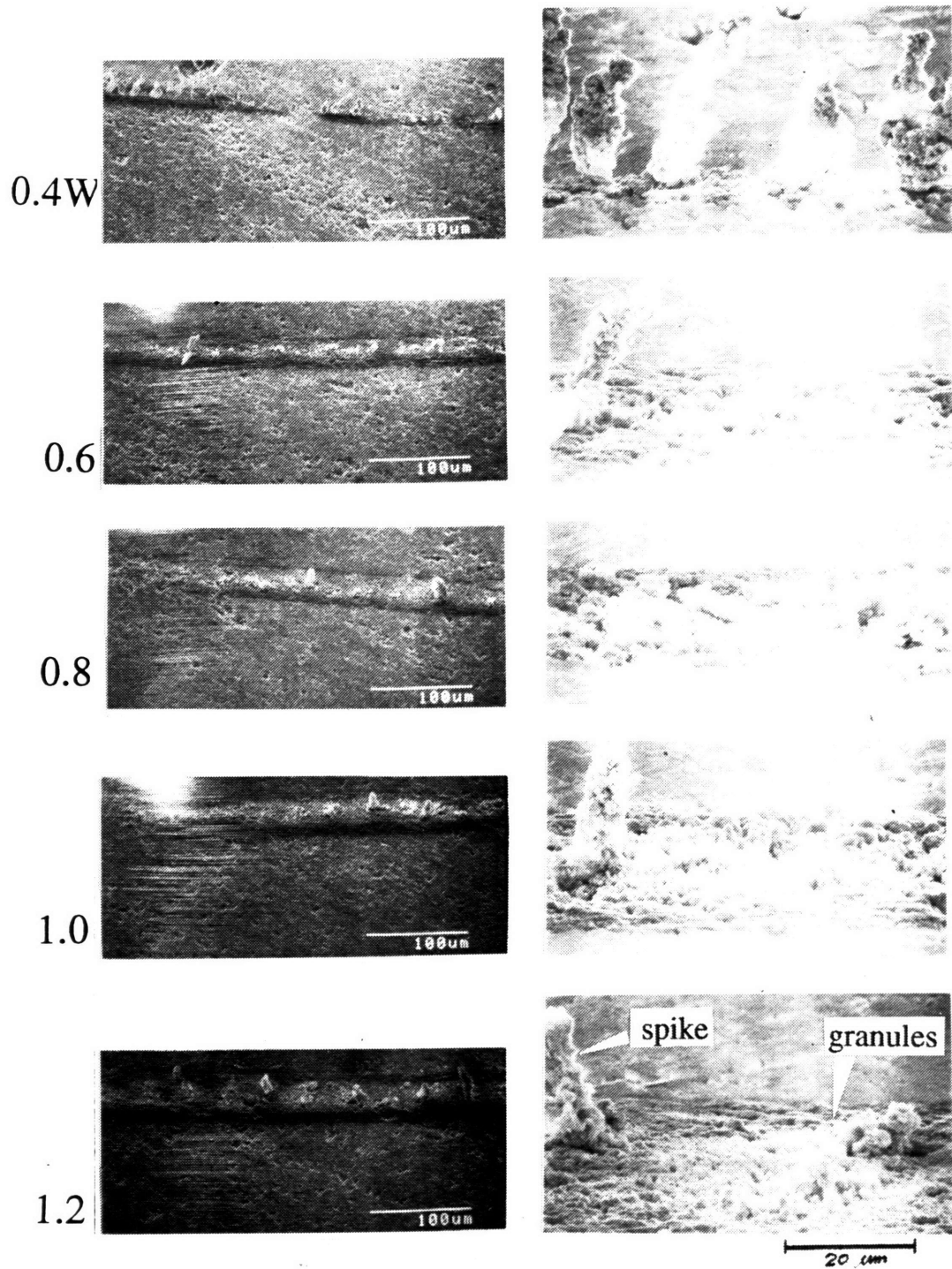


Fig. 27

Laser induced electroless Ni deposition on SiC at different powers; scan speed 20 µm/s; Ar laser; beam size 12 µm; 45 view

A convection-diffusion flow analysis was performed and indicates that to support a metal deposition rate of 1 - 10  $\mu\text{m}/\text{sec}$  requires a very fast convective flow which was not seen in in-situ video observation of the laser enhanced electroless plating. This implies there must be a very effective microscopic mass transfer mechanism different from convective flow. To estimate the magnitude of flow velocity required to create the diffusion driving force to support the deposition rate, both the required diffusion layer thickness and the hydrodynamic boundary layer thickness were estimated. Appendix A6 gives the details of such an estimation. For both the sequential and continuous approaches, the diffusion layer thickness was estimated from known metal deposition rate, and then the hydrodynamic boundary layer thickness was estimated from the diffusion layer thickness and the known Schmidt number ( $\nu/D$ ). In summary, a free stream flow with a speed on the order of 10-100 cm/sec, either vertical or parallel to the sample surface, is required to support the measured nickel deposition rate. However, by observing the bubble rising speed from video frames, the maximum flow speed in the region of several hundred  $\mu\text{m}$ s around the laser spot was found to be on the order of 1-10 mm/sec, which is far from enough to create the required thin diffusion layer. Accordingly, there must be a different but more effective mass transfer mechanism which is created by the laser and is very possibly the deposition rate limiting factor. This speculation is further supported by deposition rate data from Continuous Photo-Electroforming experiments. The Ni deposition rate in the Continuous Photo-Electroforming experiments was estimated from observing the height of the whisker structure, as described in section 3.2.2, formed at a known scan speed. Fig. 28 shows the rate data at several different cell pressures and corresponding flow-through speeds. The rate, 10-50  $\mu\text{m}/\text{sec}$ , is about one order of magnitude larger than the theoretical convective-diffusion limited rate, as plotted on the figure. This theoretical convective-diffusion rate was estimated by stagnation flow theory with a known free stream velocity (i.e., the flow-through velocity) over the powder bed of 5  $\mu\text{m}$  Ni particles, assuming bubble formation has no effect on mass transfer (see

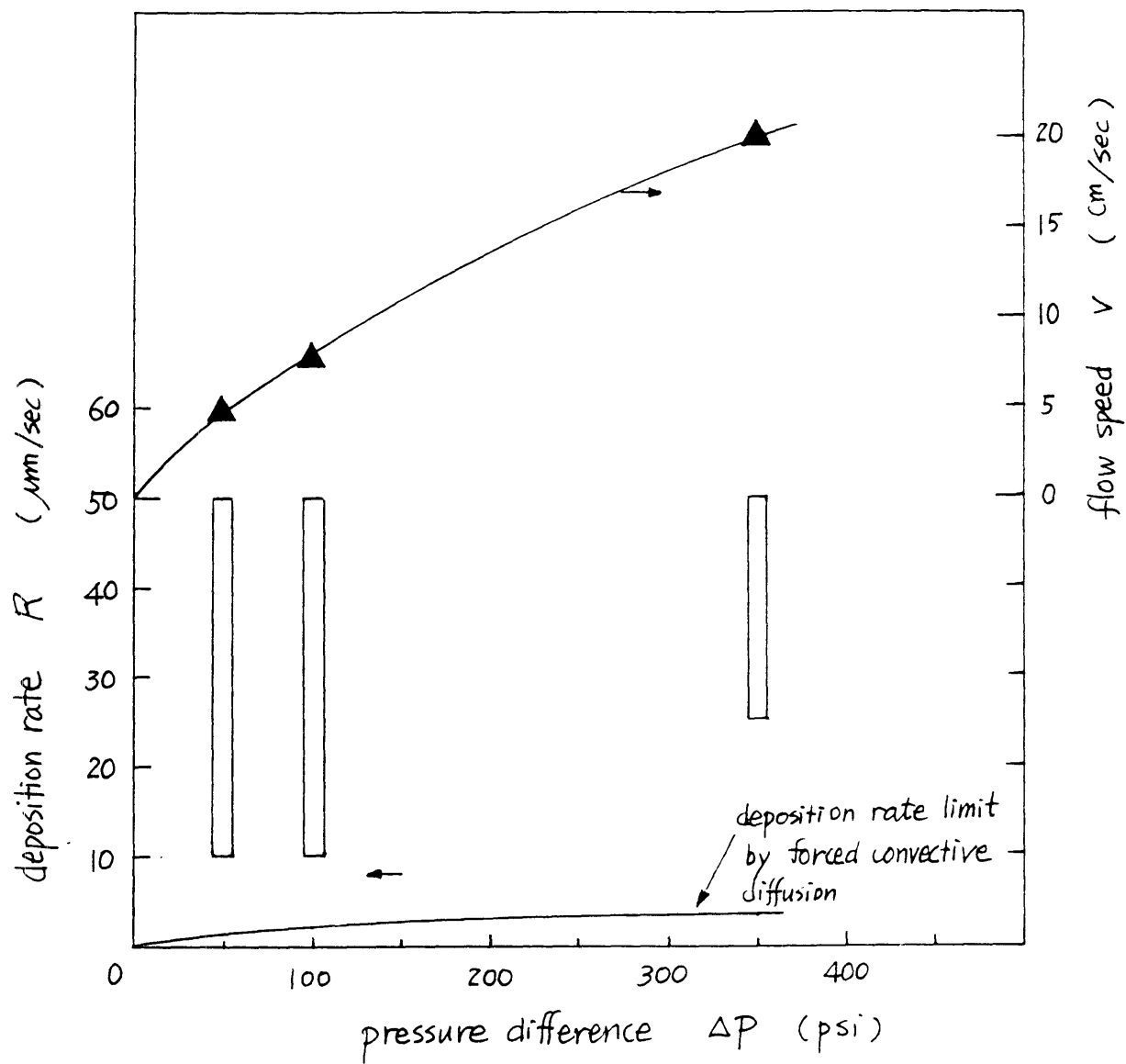


Fig. 28 Ni deposition rate in Continuous Photo-Electroforming at different cell pressures, compared with theoretical mass transfer limit by forced convective diffusion at corresponding flow speeds; 5  $\mu\text{m}$  Ni powder, laser power 0.3W, 12  $\mu\text{m}$  beam spot, rate estimated from rate of whisker formation

Appendix A6). This strongly implies a laser induced mass transfer mechanism is controlling the deposition.

Mass transfer mechanism at a gas evolving electrode has been studied by several researchers and models have been proposed [Ibl & Venczel 1970, Janssen & Hoogland 1970, 1973]. A bubble displacement model proposed by Ibl and Venczel is simple and explicit, and has been proved to be quite successful for hydrogen evolving electrode. In this work, it was found that this model can be applied to explain the deposition rate limit of laser enhanced electroless plating. According to the model, the mass transfer limited reactant flux is determined by the gas generation rate and the size of detaching bubbles, as

$$j_l = \sqrt{\frac{12vD}{\pi d_{bl}}} C \quad (4-1)$$

where  $v$  is volume of gas generated per unit area per unit time,  $d_{bl}$  is the size of gas bubble,  $D$  is diffusivity and  $C$  is bulk concentration(See Appendix 7 for details). From reaction stoichiometry, the gas generation rate can be estimated from measured deposition rate. From video observation, the bubble size can also be estimated. Therefore, the limiting deposition rate can be estimated from eqn.(4-1) and can be compared with the measured deposition rate to see if the laser enhanced electroless plating rate can be described by the model. Experimental deposition rate data from Fig. 26, both averaged rate and rate of spike forming, were used to estimate the hydrogen gas generation rate. The bubble size was estimated from in-situ video observation of the same experiments. The bubbles were found to be so small, as shown in [Fig. 29](#), that their size range can only be estimated as no larger than one or two TV lines on the video screen, which is around 5-10  $\mu\text{m}$ . The estimated limiting rate and the measured deposition rate are plotted in [Fig. 30](#) for comparison, which shows the bubble displacement model gives quite a good estimation of the real rate. Fig. 30 also shows the deposition rate limited by free convective diffusion, based on the observed flow speed of 1-10 mm/sec around the laser spot, which is orders of magnitude below the actual deposition rate.

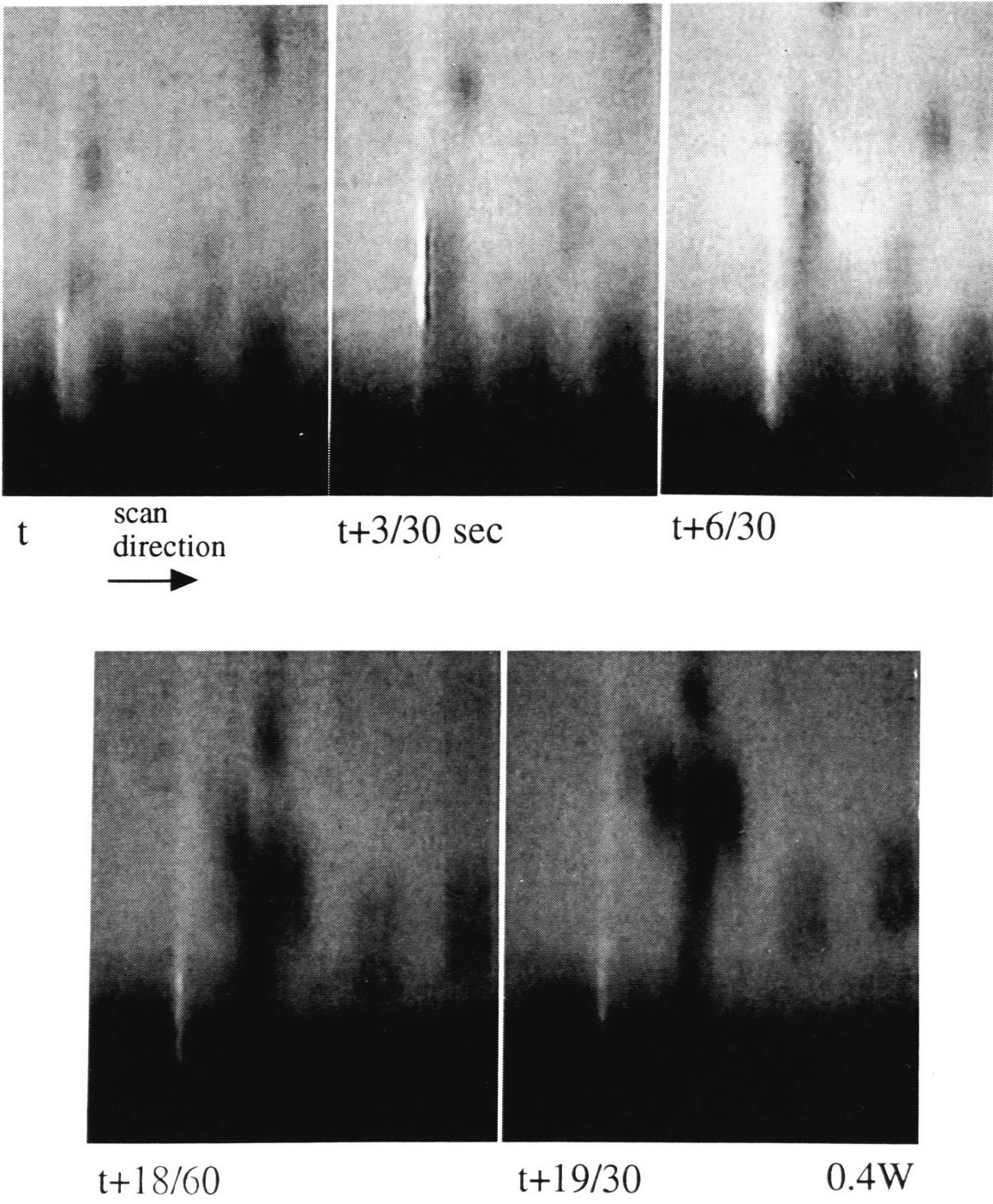


Fig. 29  
 Successive image frames of slow laser scanning across SiC pellet in electroless Ni solution; scan speed 20  $\mu\text{m/s}$ ;  $\text{Ar}^+$  laser; beam size 12  $\mu\text{m}$ ; scale bar 250  $\mu\text{m}$

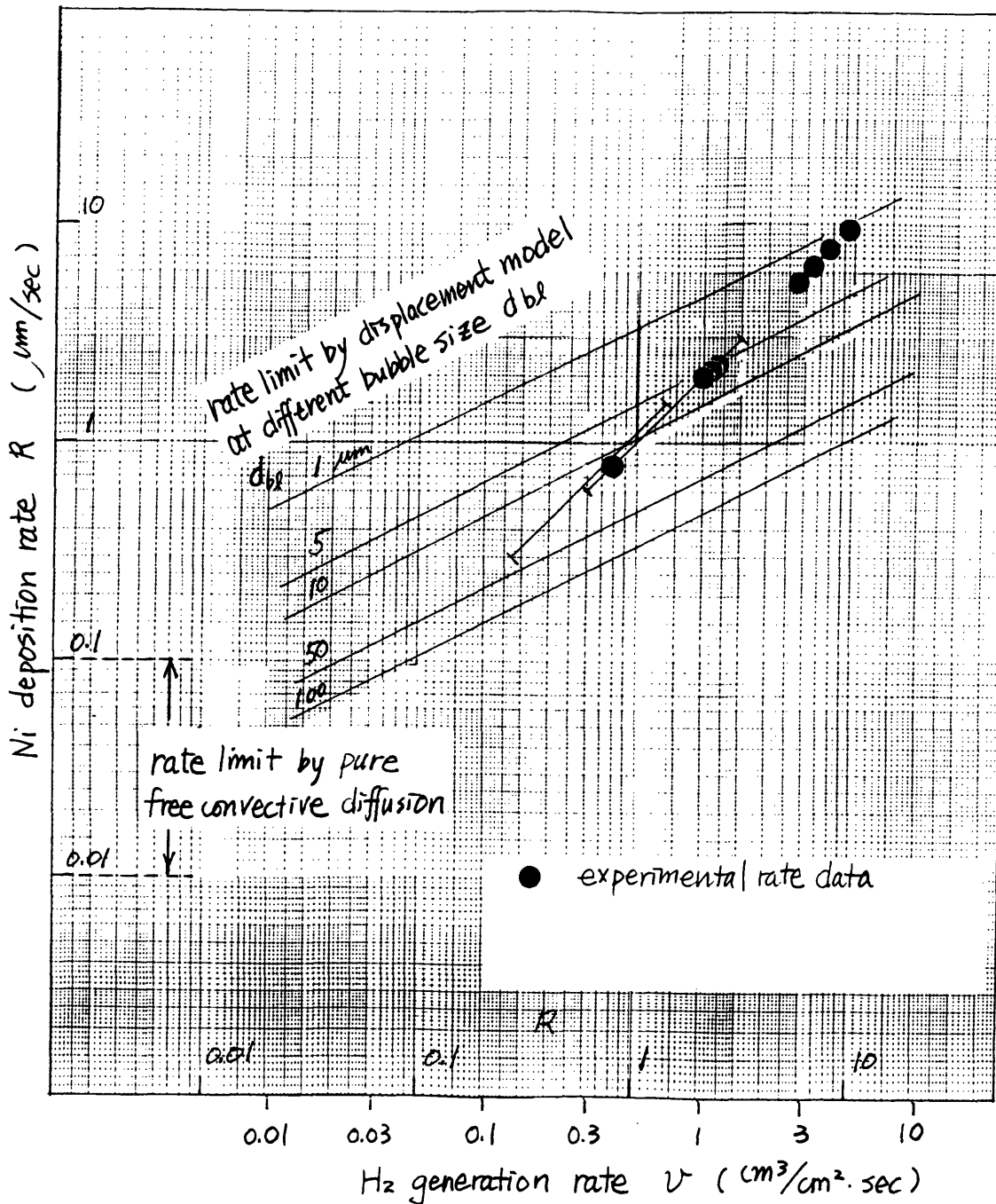


Fig. 30

Comparing experimental deposition rate of laser induced electroless Ni with mass transfer limits by displacement model and by free convective diffusion

In conclusion, the process is very possibly controlled by mass transfer and the mass transfer mechanism is strongly related to laser induced hydrogen gas formation, which could be explained by the bubble displacement model.

### 4.2.3 Laser Enhancement

In summary, the experiments covered a range of laser power density from 1 to 10 GW/m<sup>2</sup>, and surface temperature ranging from 200 C up to the melting point of nickel was achieved, while nickel deposition rate was always in an averaged range of 0.6 - 3.0 μm/sec, with a spike formation rate of 6-10 μm/sec. Comparing this rate to normal electroless nickel plating rate which is about 30 μm/hr in hot solution bath, the laser enhancement factor is about 100-1000 times. Fig. 31 plots some normal electroless Ni rate data, which were activation controlled rate data taken from the literature, together with this enhanced rate range on a log (rate) to 1/T graph. The slope of the extrapolation of "normal" rate data was according to the known activation energy of electroless Ni reaction (see Appendix A8). From Fig. 31, it is clear that the focused laser beam brings up deposition rate from a steep activation controlled region to a region where rate does not change significantly with temperature. The transition zone is around 200-300 C, provided that the fundamental kinetics does not change. It is recalled that Fig. 20, results of Ni-glass experiments, also showed that the laser enhancement starts at about 200-300 C or around apparent power density 1 GW/cm<sup>2</sup>. The insensitiveness of the laser enhanced rate to temperature implies the process is controlled by mass transfer. Mass transfer control may also explain the two distinctive enhanced rate data zones on the plot, as the higher rate associated with spike-formation may be due to occasional local gas bubble explosion or detaching which temporarily made mass transfer more effective.

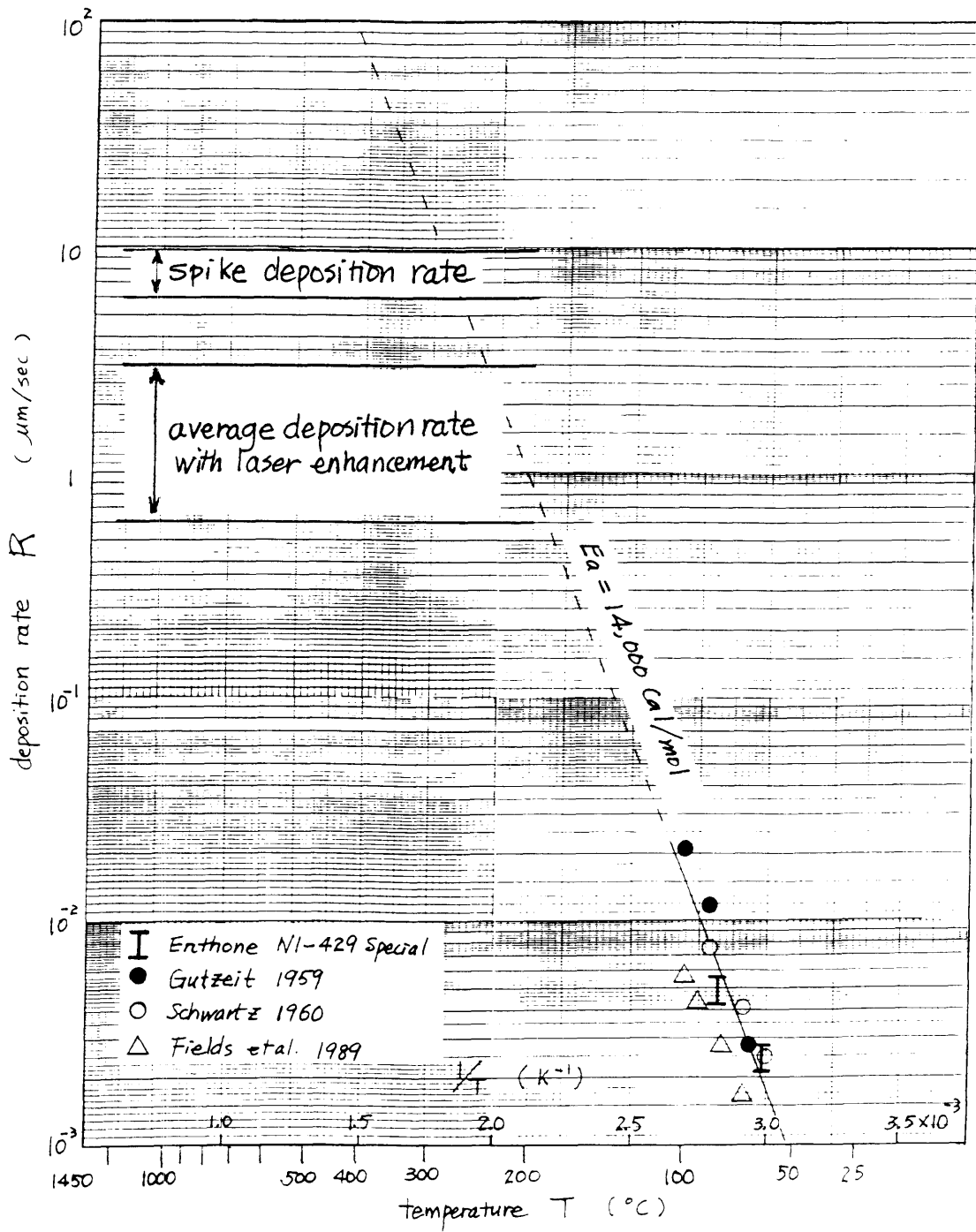


Fig. 31 Ni deposition rate in log scale vs.  $1/T$  plot

### 4.3 Gas Bubble Effects

The formation and detaching of hydrogen gas bubbles under the laser spot can shield and diverge the beam and reduce the effective power input. A successive image frames taken from video observation shows the phenomena, as in [Fig. 32](#). Comparing the relation of temperature to laser power in both back and front laser scanning over Ni-film, [Fig. 17](#), it can be seen that the bubble shielding effect reduced the effective input power to 50-80%. [Fig. 33](#) shows the bubble shield that may have caused this reduction.

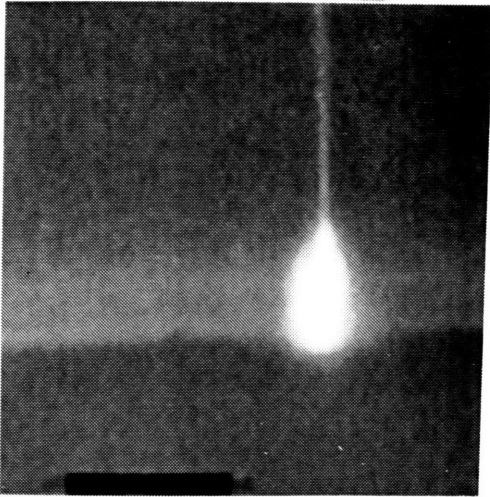
Observation has shown that the detaching hydrogen bubble size is around 10  $\mu\text{m}$ , which is about the size of the laser beam. A simple ray tracing analysis shows that one gas bubble may act as a diverging lens and thus expend the laser beam and reduce incident beam power density to 25%, and two successive bubbles may reduce it to 3%, as illustrated in [Fig. 34](#). This diverging effect may explain the above effective power reduction.

The diverging effect may also affect resolution. Experiments indicate that lines created by back scanning on Ni-film have finer resolution than those created by front scanning at same powers, as shown in [Fig. 35](#). Simple refraction analysis can again explain this phenomena.

### 4.4 Surface Temperature: SiC samples

To estimate the surface temperature of silicon carbide under laser scanning is more difficult since morphology observation may not work. However, with the knowledge of the laser enhancement transition temperature of 200-300 C, as described in section 4.2.3, an approximate estimation can be made.

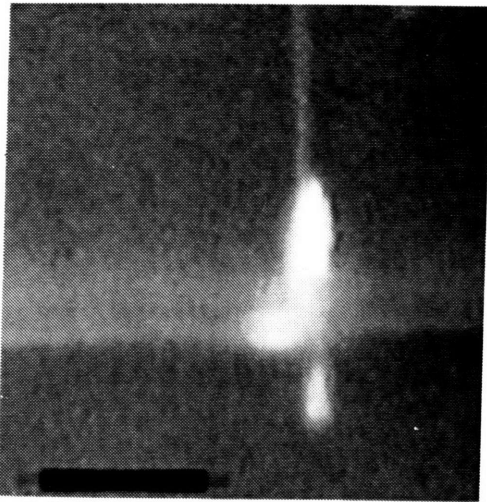
Experiments of laser induced electroless nickel plating on non-pretreated SiC pellets were performed. The laser optics and SiC sample preparation were similar to those



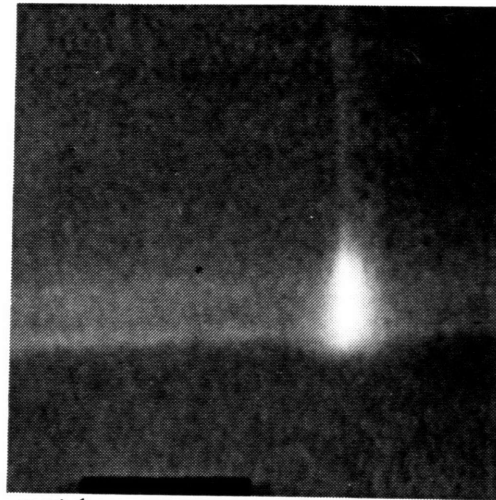
1st frame



+15/30



+1/30 sec



+11/30



+2/30

Fig. 32 Bubble shielding effect; same condition as Fig. 27, except laser power 0.4W

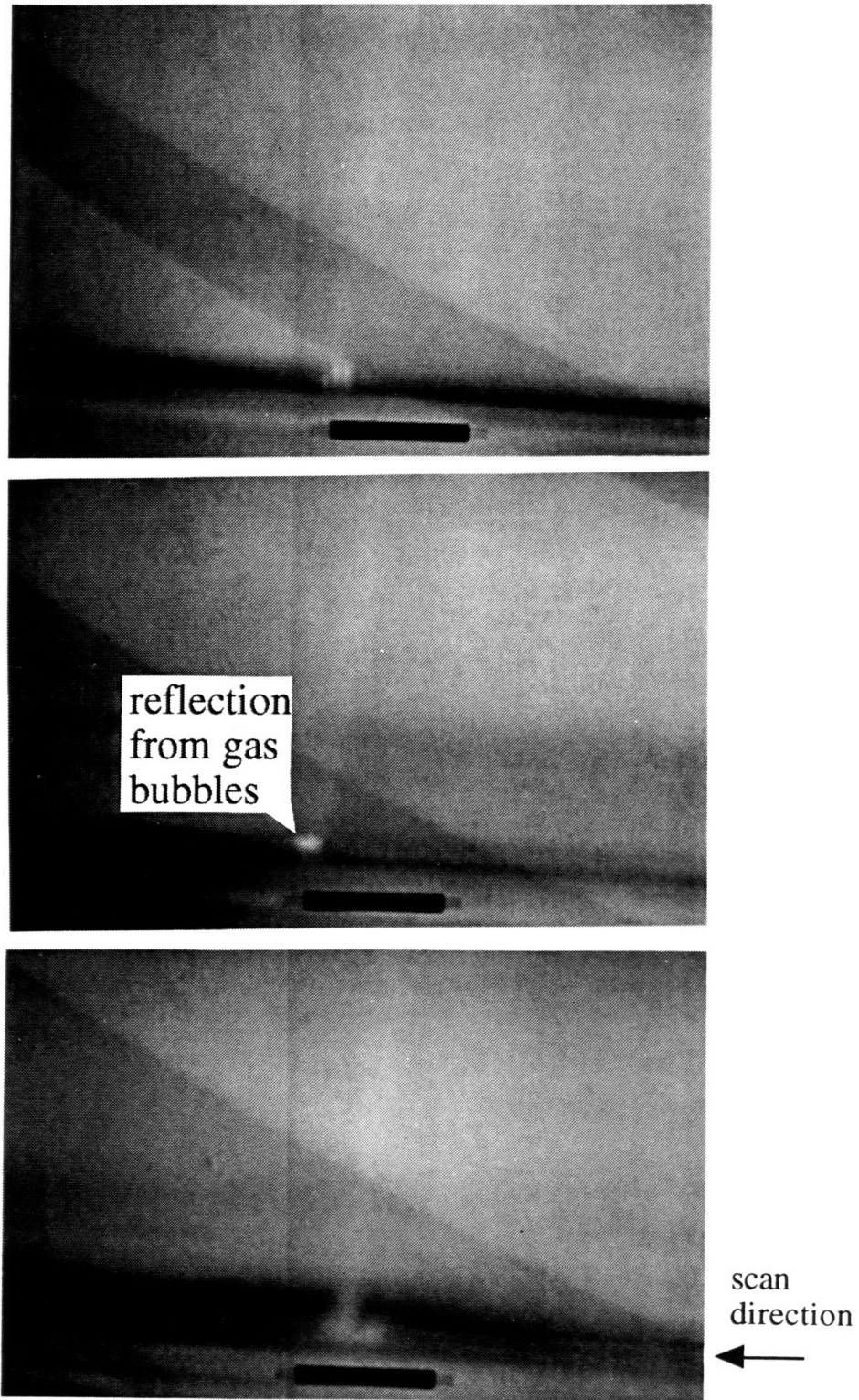


Fig. 33  
Successive image frames of laser scanning across Ni-film on glass in electroless Ni solution; scan speed 6.28 cm/s; Ar<sup>+</sup> laser; beam size 12 μm; 0.8W; scale bar 250 μm

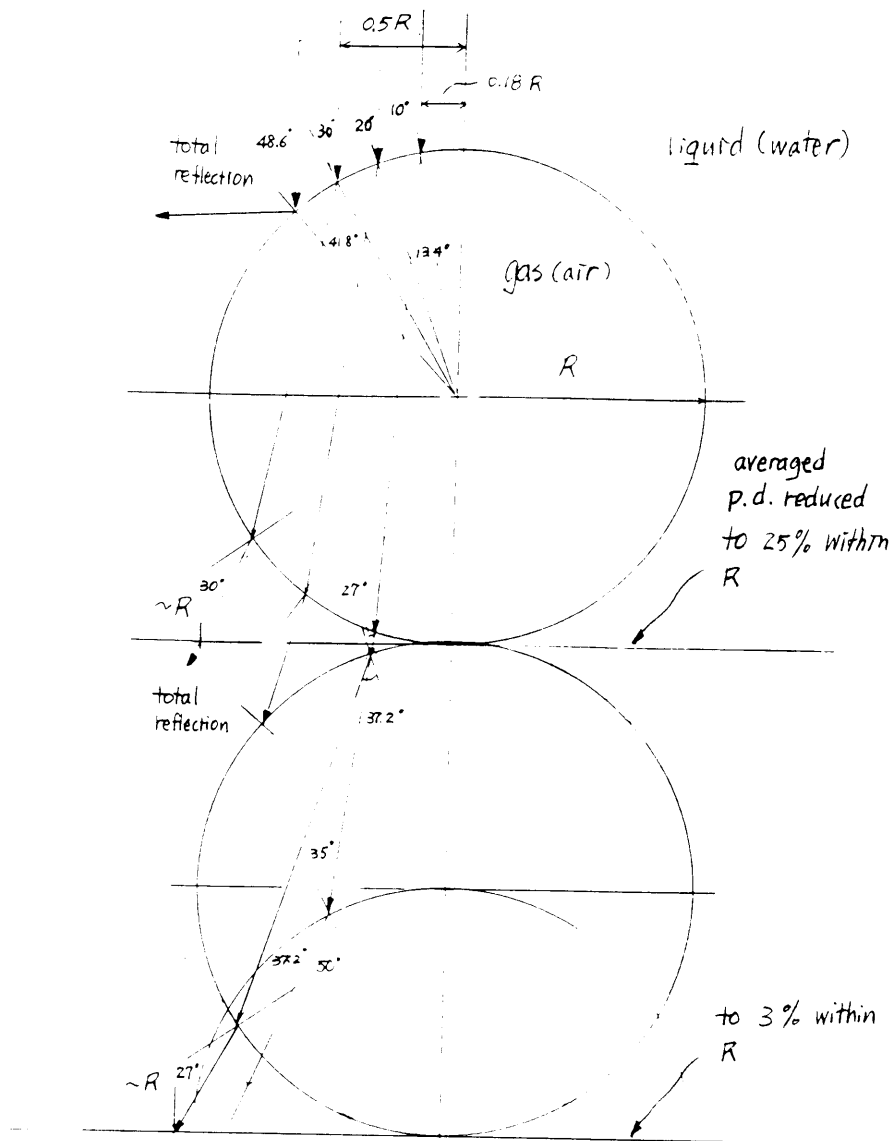


Fig. 34 Ray tracing analysis to explain bubble shielding and diverging effect

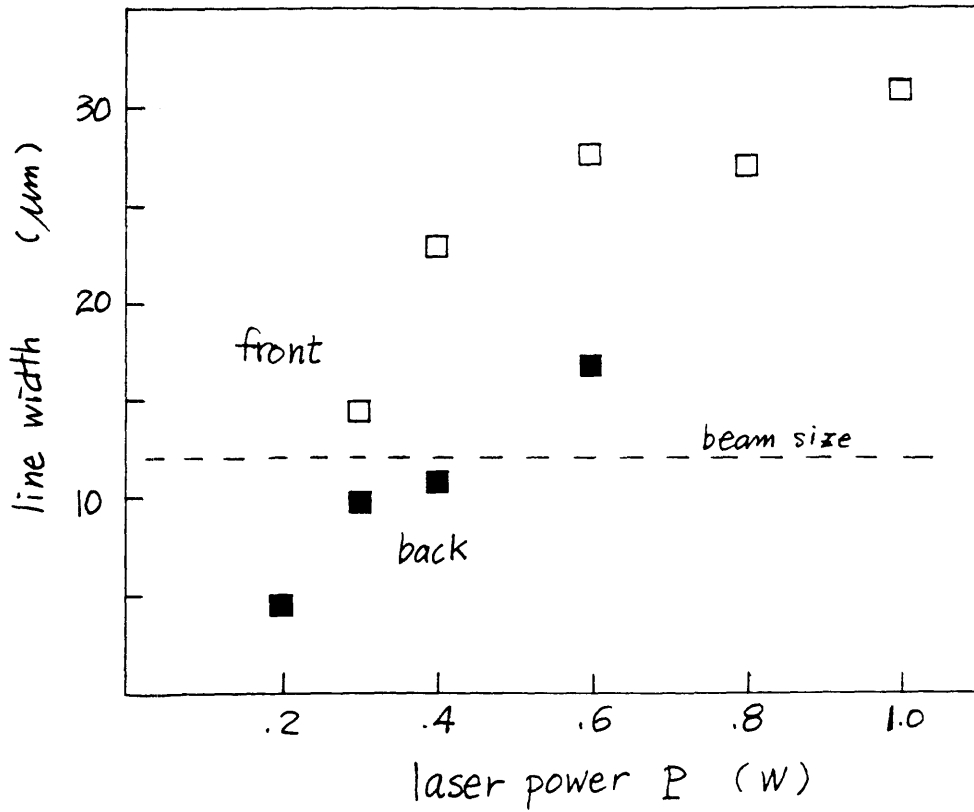


Fig. 35

Comparing resolutions of back scanning and front scanning of laser induced electroless Ni on Ni-coated glass; scan speed 6.28 cm/s; Ar laser

described in section 3.2.1, or in Appendix 1. Fig. 19 shows the lines created by the laser beam scanning at 5 cm/sec, at different power. It was found that, for laser power lower than 0.6-0.8 W, the line deposition became almost invisible. This implies that the nickel deposition rate started to fall below the laser enhancement level at this power range. Therefore, this power range corresponds to the transition temperature, 200-300 C. Knowing that surface temperature increase is generally proportional to laser power, as shown in the Ni-glass experiments, Fig. 17, an approximate surface temperature curve on SiC can be plotted, as shown in Fig. 36.

Comparing Fig. 17 and Fig. 36, SiC had a lower surface temperature than Ni-glass did, when the laser scanned at the same power and at similar speeds. This observation can be explained by two major factors. First, the thermal diffusivity of SiC is higher than that of glass so that SiC conducts heat away faster. Second, comparing frames of in-situ video observation of both cases, as shown in Fig. 33 and 37, the bright spot above the laser exposure area on the SiC surface was much larger and brighter than in the Ni-film cases. This implies that more hydrogen bubbles were generated on SiC than on Ni-film, as more bubbles reflected more laser light, and the real laser power (effective power) on SiC surface might be lower or the convection heat transfer coefficient might be higher, both tend to reduce surface temperature increase. This also implies that the SiC samples may have a better catalytic effect for electroless Ni than sputtered Ni film, at elevated temperatures.

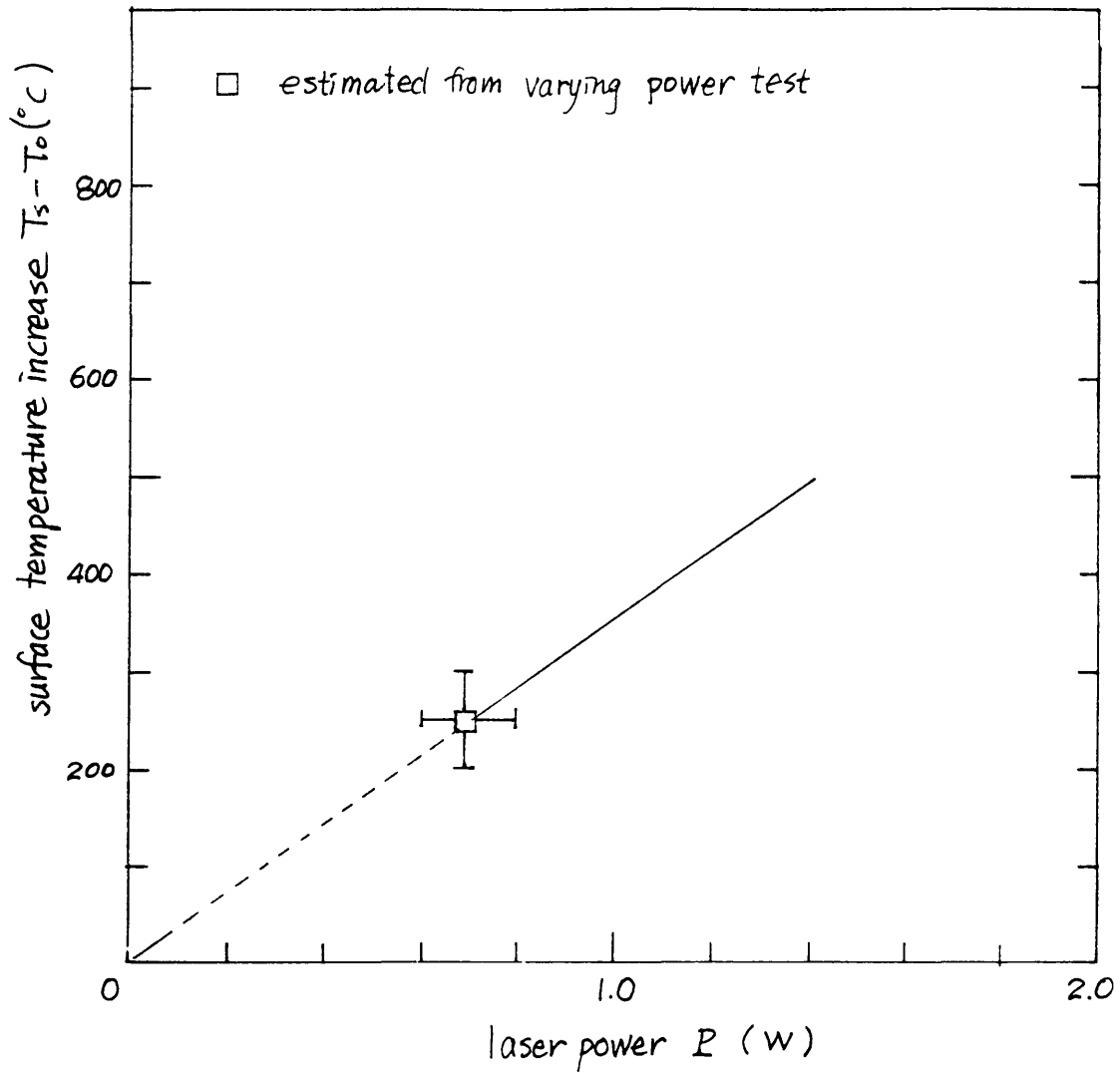


Fig. 36 Estimated temperature increase on SiC pellet in electroless solution, scan speed 5 cm/sec, laser beam size 12  $\mu\text{m}$

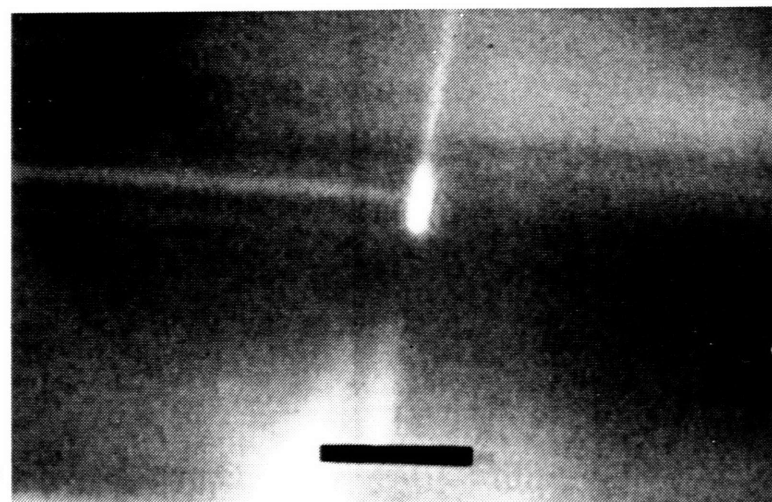
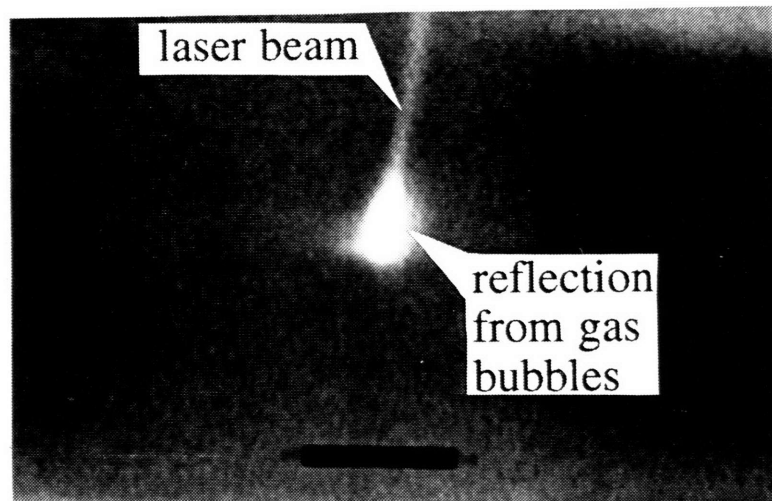
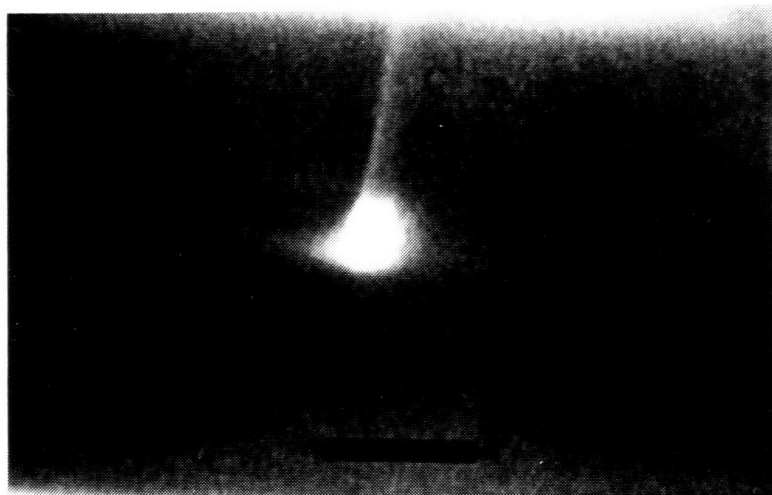


Fig. 37  
Successive images frames of laser scanning across SiC pellet in electroless Ni solution; scan speed 5cm/s; Ar laser; beam size 12  $\mu\text{m}$ ; 0.8W; scale bar 250  $\mu\text{m}$

## 5. Process Characteristics

In summary, the major process characteristics achieved by the equipment and optics used in this research are as follows,

### Rate

- laser writing speed: 24 cm/sec by 1.5 W laser with 12  $\mu\text{m}$  beam in electroless nickel on SiC;
- laser enhanced nickel metal deposition rate: 0.6-3  $\mu\text{m}/\text{sec}$

### Resolution

- planar resolution: 10-15  $\mu\text{m}$  line width by 12  $\mu\text{m}$  laser beam in electroless copper on SiC;
- layer thickness: 5-10  $\mu\text{m}$  SiC layer

### Materials

- nickel/SiC; copper/SiC; nickel.

The actual process limits can be further improved with improved facilities, e.g. optics capable of finer laser beam spot. This chapter discusses the limits of the process characteristics and the major factors that affect these characteristics.

## 5.1 Rate

### 5.1.1 Sequential Photo-Electroforming

Because the laser enhanced electroless plating rate reaches a limiting value when the surface temperature exceeds a transition value, which is around 200-300 C as described in section 4.2.3, the fabrication rate of Sequential Photo-Electroforming will depend on how fast the to-be-patterned regions can be heated up to the desired temperature range and how long it will stay within that range. In Appendix 5, a simple one-dimensional transient conductive-convective model was derived to approximate the stationary laser heating of a solid. The resulting expression of the surface temperature under the laser spot is

$$\frac{T_s(t) - T_c}{\frac{P}{h}} = 1 - e^{-\alpha\beta^2 t} \operatorname{erfc}(\beta\sqrt{\alpha t}) \quad (5-1),$$

where

$$\beta = \frac{h}{2k} \tag{5-2}$$

and  $h$  is convective heat transfer coefficient,  $k$  is solid thermal conductivity,  $p$  is effective input power density, and  $\alpha$  is solid thermal diffusivity. The above equation can be applied to investigate how laser scan speed and power density can affect surface temperature, using the following approximate relation to convert laser exposure duration  $t$  to scan speed  $u$ ,

$$u = d_b/t, \tag{5-3}$$

where  $d_b$  is laser beam size. The resulted relation between a dimensionless temperature and a dimensionless time (or scan speed) is illustrated in [Fig. 38](#). This relation indicates that at constant power density, higher scan speed brings down surface temperature increase, which means shorter cooling period and less metal deposited. If a desired temperature increase is to be maintained while the scan speed is increased, then the laser power density should be increased.

A set of fast scan experiments was performed to investigate the scan speed limit, and the result of electroless Ni on SiC pellets is summarized as follows,

scan speed	power	observation
5 cm/sec	0.8-1.4 W	continuous line w/ good deposits of 0.4-0.7 $\mu\text{m}$
24 cm/s	1.4-1.6W	continuous line w/good deposits > 0.1 $\mu\text{m}$
32	1.5	broken line w/ light deposits
40	1.5	broken line w/ light deposits
48	1.5	no significant deposits.

[Fig. 39](#) shows the line at 24 cm/sec. These results indicate a maximum scan speed, in terms of generating good continuous lines, exists around 25 cm/sec for laser power around 1.5 W, and the deposits becomes invisible as scan speed approaches 50 cm/sec. The experimental scan speed limit of electroless Cu under similar conditions was found to be

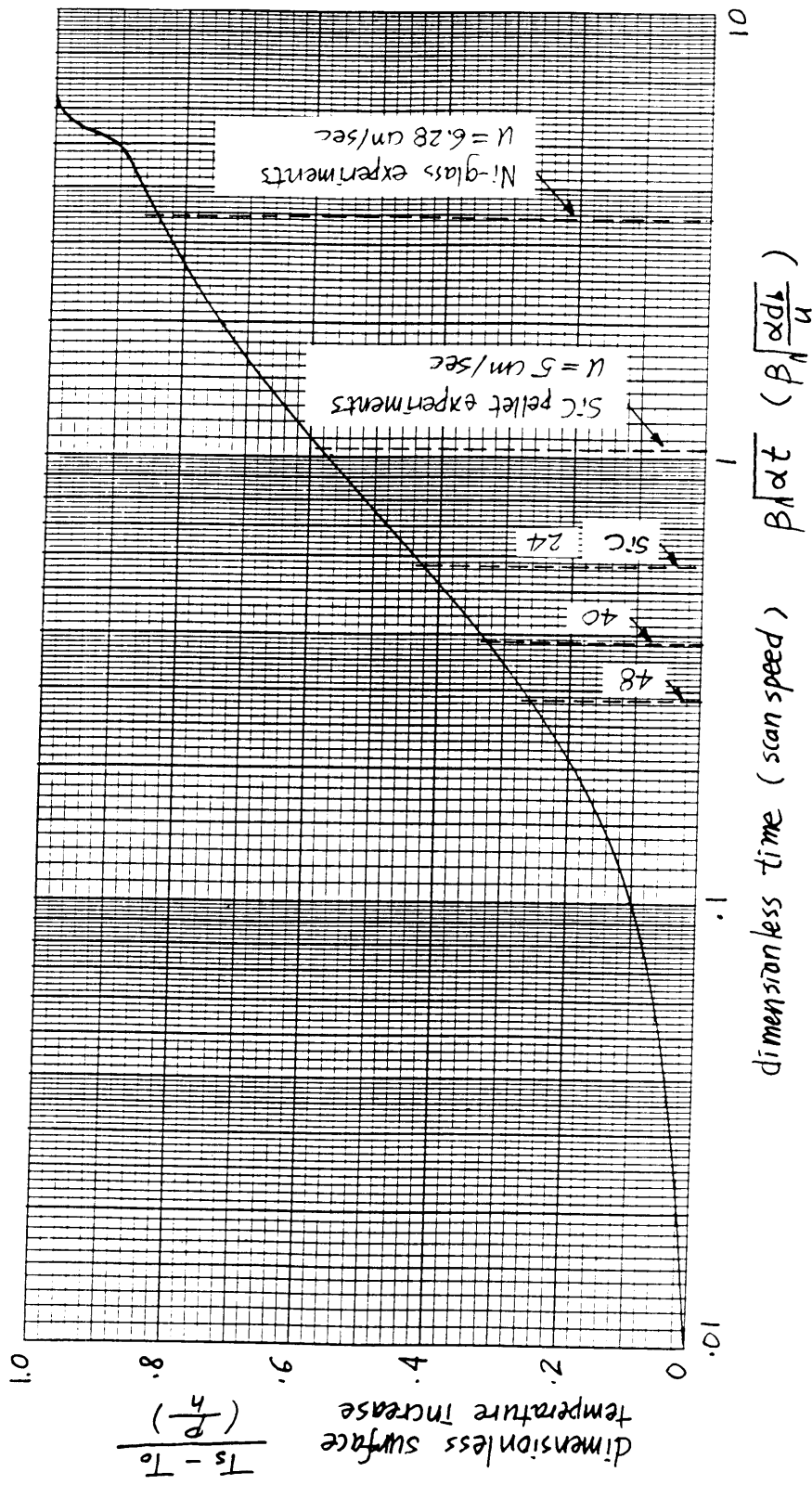


Fig. 38 Dimensionless solution of conductive-convective model of laser heating (scanning) (see text)

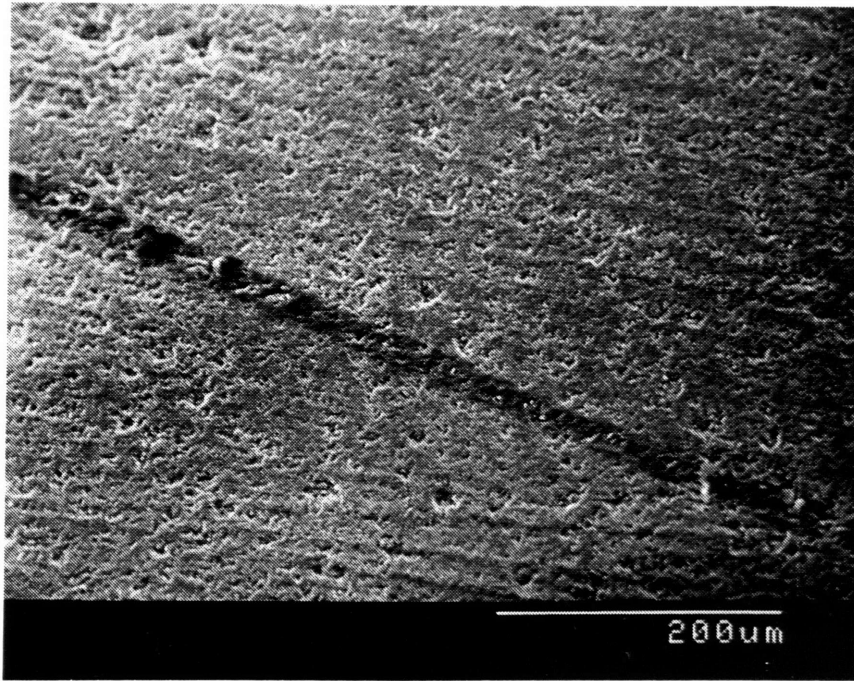


Fig. 39 A Ni/SiC line created at scan speed 24 cm/sec, laser power 1.4W, beam spot size 12  $\mu\text{m}$

around 10 cm/sec. The approximate locations of scan speeds of the above experiment as well as the Ni-glass experiments, section 4.1, are plotted on Fig. 38 to show how scanning speed affects surface temperature. To plot those scan speeds onto this dimensionless chart, a heat transfer coefficient  $h$  of  $10^6$  W/m<sup>2</sup> sec, estimated from the known peak surface temperature in the Ni-film back scanning experiments, was used for all cases (see Appendix 5 for details). It should be noted that, due to the limitation of the model (Appendix 5), this heat transfer coefficient  $h$  actually represents an overall convective cooling effect concentrated at one spot, i.e. the laser beam spot, since other portion of the surface was assumed to be thermally insulated for simplicity.

It was described in section 4.2 that a long cooling period may follow a laser exposure and enhanced electroless deposition can continue during that cooling period. When laser scans fast, the ratio of the cooling period to the laser exposure duration becomes very large such that most of the deposition forms after the laser exposure duration. This is how the maximum scan speed can reach 25 cm/sec. By measuring the thickness of laser induced nickel deposition, the length of the cooling period can be estimated from the known laser enhanced electroless deposition rate obtained in section 4.2. From Ni-film experiments shown in Fig. 20, the laser induced Ni deposition thickness was estimated to be 0.2-0.3  $\mu\text{m}$ . Dividing by 1-10  $\mu\text{m}/\text{sec}$ , the mass transfer limited rate from section 4.2, this deposition thickness corresponds to a total plating period of 0.02-0.3 second; while the scanning speed of the 12  $\mu\text{m}$  laser spot, 6.28 cm/sec, corresponds to an exposure duration of only 0.19 ms for any point along the path of scanning. Therefore, the cooling period is 100 to 1000 times longer than laser exposure duration. Similar result also applies to SiC experiments at 5 cm/sec scan speed.

### **5.1.2 Continuous Photo-Electroforming**

The laser patterning rate of the Continuous Photo-Electroforming approach will be much lower than the Sequential approach since the flow-through liquid has a strong

convective cooling effect on the powder bed. This convective cooling effect tends to increase the rise time of laser heating and reduce the after exposure cooling period, resulting in a decrease of scan speed.

From observing nickel deposition in the flow-through cell experiments, the deposition rate was estimated and the maximum laser scan speed can be deduced. The nickel deposition rate was estimated from observing the height of the whisker structure, as described in section 3.2.2, formed at a known scan speed. In-situ observation from the side window of the flow cell shows that the whisker formation occurs basically within the laser exposure duration and no cooling period plating was observed. Fig. 28 summarizes the rate estimation, which indicates a rate range from 10 to 50  $\mu\text{m}/\text{sec}$ . Assuming a deposition thickness of several thousands of angstrom is enough for the photo-metallization step, then the corresponding maximum scan speed is around 1 mm/sec for a 12  $\mu\text{m}$  laser spot. This scan speed limit is far less than that of the Sequential approach, due to the lack of the long cooling period after laser exposure.

## 5.2 Resolution

### 5.2.1 Sequential Photo-Electroforming

There are two factors that may affect process resolution: thermal diffusion and gas bubble diverging effect. The effect of thermal diffusion can be examined by estimating the thermal diffusion distance using the thermal conductive-convective model. In Appendix 5, the transient relation between solid temperature and distance from the laser beam at different heat transfer condition was derived. The relation is

$$\frac{T(r,t) - T_0}{T_s(t) - T_0} = \frac{\text{erfc}(A) - e^{-A^2} [e^{(A+B)^2} \text{erfc}(A+B)]}{1 - e^{B^2} \text{erfc}(B)} \quad (5-4),$$

where

$$A = \frac{x}{\sqrt{4\alpha t}} \quad x = r - r_b,$$

$$B = \beta\sqrt{\alpha t} . \quad \beta = \frac{h}{2k}$$

$r_b$  is beam radius,  $h$  is convective heat transfer coefficient,  $k$  is solid thermal conductivity,  $\alpha$  is solid thermal diffusivity, and  $T_s$  is surface temperature at  $x=0$ . Again, eqn. (5-1) can be used to convert laser exposure time  $t$  to scan speed  $u$ . The solution is summarized in dimensionless forms in [Fig. 40](#). A set of experimental resolution data is plotted in [Fig. 41](#), together with corresponding thermal diffusion distances estimated from [Fig. 40](#). The estimation was based on the following assumptions:

- The values of  $T_s-T_0$  were taken from [Fig. 17](#) for Ni-film experiments, and from [Fig. 36](#) for SiC experiments. These are experimental results.
- $(T-T_0)=225$  C, the transition temperature, was used to define the thermal diffusion distance. That is, the edge of the patterned line is assumed to be at the transition temperature.
- For simplicity,  $B$  is assumed constant for all cases, since the variation of  $B$  does not affect the solution of temperature profile very much, as can be seen on [Fig. 38](#). From [Fig. 35](#),  $B$  was estimated to be 1 for SiC experiments at scan speed 5 cm/sec, and 3.5 for Ni-film experiments at 6.28 cm/sec. Therefore,  $B=1$  can be a reasonable approximation.

The thermal diffusion distance  $x$  was then obtained from solution of A. The corresponding line width  $2r$  was plotted in [Fig. 41](#). The plot shows that the real resolution is much finer than the thermal diffusion distance. This is probably because the heat induced flow over the surface area around the laser beam cools the surface down, which is not considered in the simplified model. In conclusion, the real resolution can be much finer than the thermal diffusion distance and approaches the beam size. For example, [Fig. 4](#) shows a pattern of 15  $\mu\text{m}$  wide lines created by laser enhanced electroless copper plating.

It has been shown in [Fig. 35](#) that lines finer than the laser beam size were created by laser scanning from the backside of the Ni-glass samples, as there was no bubble diverging effect; while front scans created coarser lines at the same powers. This result

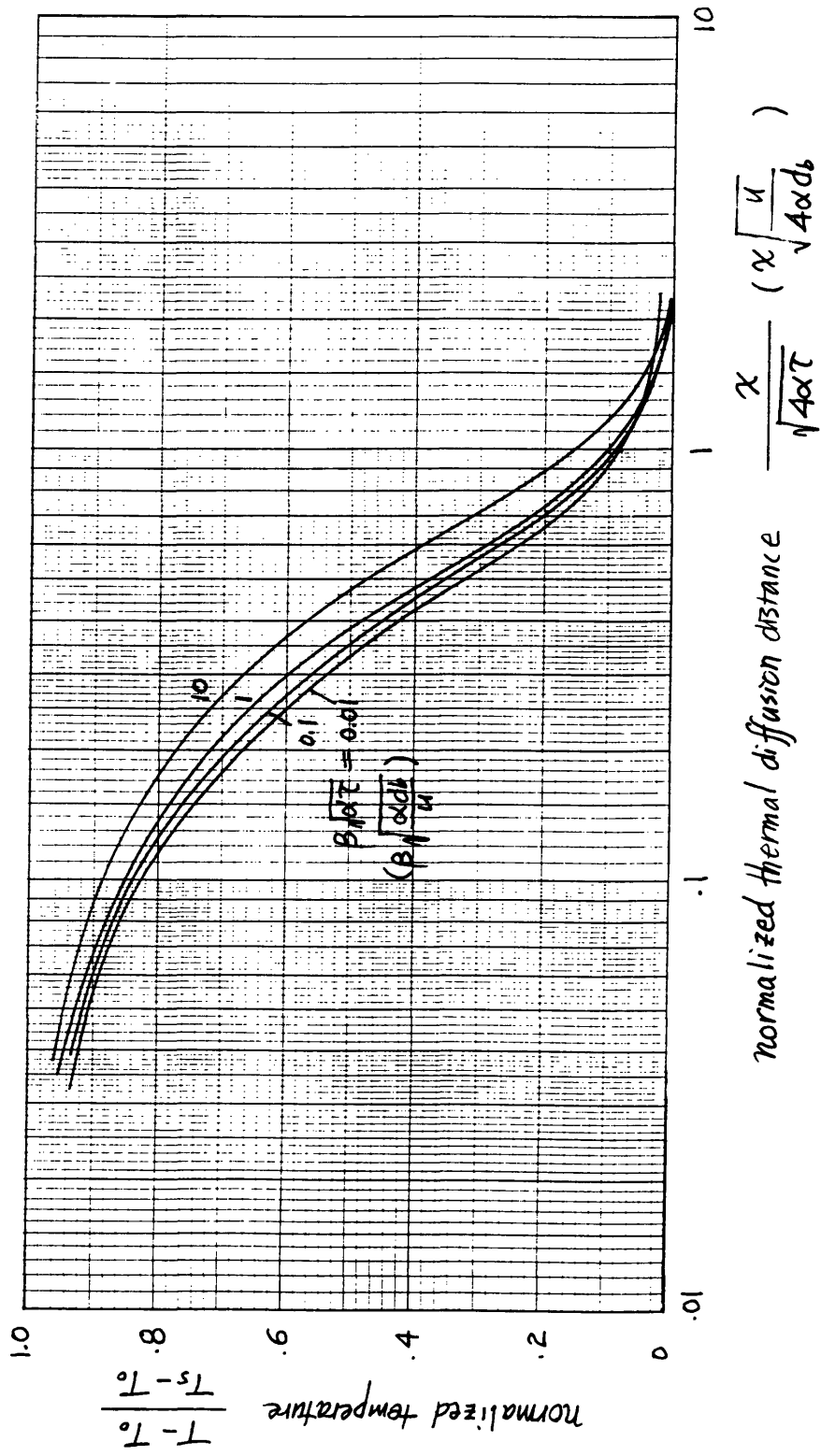


Fig. 40 Dimensionless thermal diffusion distance by conductive-convective model of laser heating (scanning) (see text)

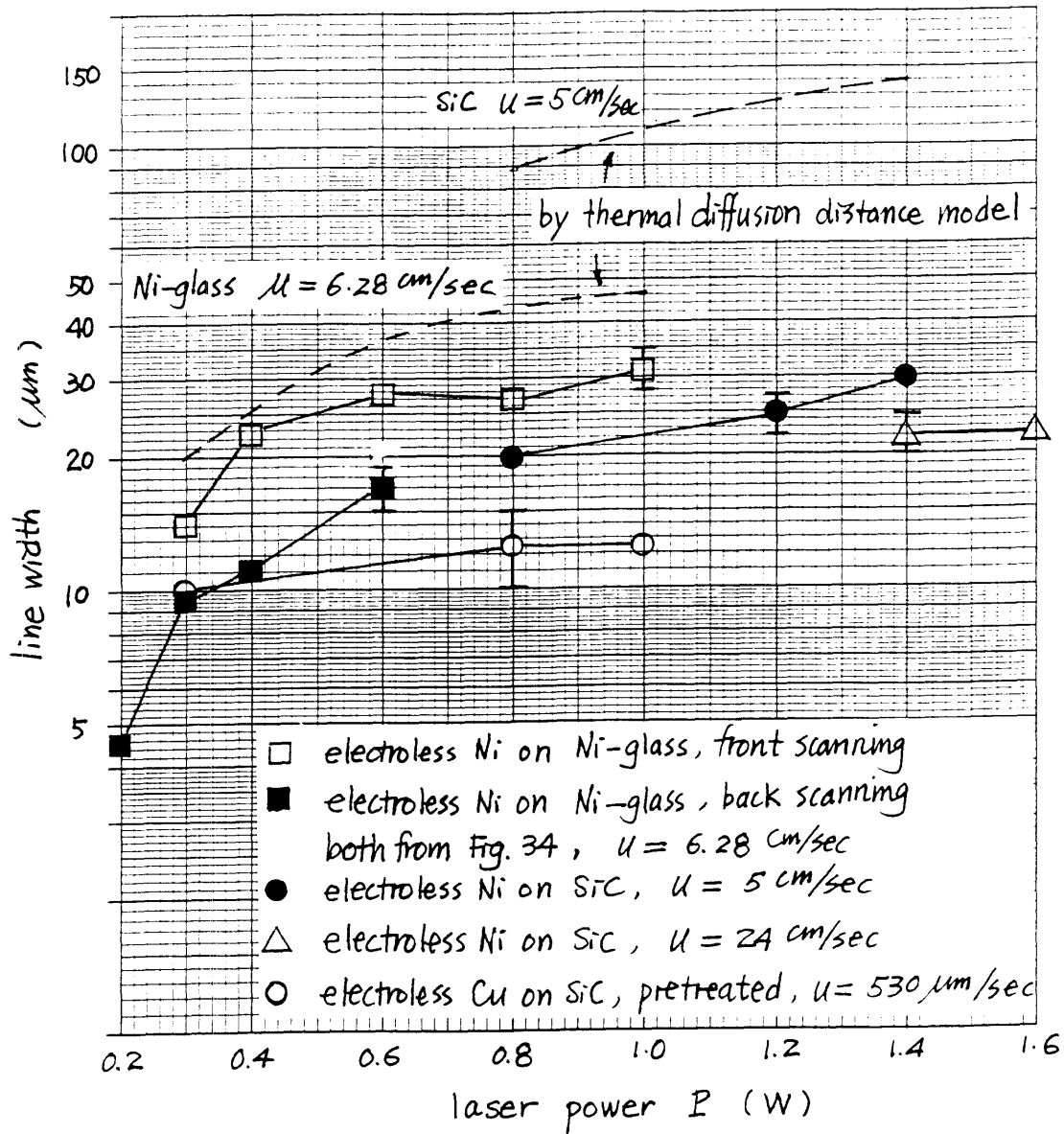


Fig. 41

Comparing experimental resolution and theoretical thermal diffusion distance

further implies that the convective cooling over the surface area around the beam is effective and also implies that bubble diverging effect may be the dominant resolution limiting factor.

Finer resolution can be obtained by reducing laser beam size. Line width as fine as 2  $\mu\text{m}$  created by laser enhanced electroplating has been reported by using better optical setup [Puipe et al. 1981].

### **5.2.2 Continuous Photo-Electroforming**

The gas generation effect has a different form in Continuous Photo-Electroforming as the gas bubbles are carried downward by the flow instead of flowing upward. If the bubbles are carried away efficiently, then the diverging effect may be less severe than the Sequential approach, which means a better resolution. However, if bubble coalescence occurs close to the exposure area, then a gas film may form directly under the laser beam which may shield and diversify the downward flow and become the resolution limiting factor. The coarse resolution of 100-200  $\mu\text{m}$  observed in the patterns and parts formed by the Continuous approach, section 3.2.2, was probably caused by this effect. It could also be due to thermal diffusion since the scanning speed used was low, 2  $\mu\text{m}/\text{sec}$  as described in section 3.2.2. Unfortunately, the resolving power of the observation optics used in this work was not high enough to reveal the details under the laser beam spot. Further observation with improved optics is required to determine the limiting factor of resolution.

### **5.3 Material Strength**

The tensile strength of lift-off line segments created by Sequential Photo-Electroforming has been tested to obtain a preliminary understanding of the material strength. The samples were created from pellet of 1  $\mu\text{m}$  silicon carbide powder with laser enhanced electroless nickel deposition, followed by 2-5 min. second plating of the same electroless Ni solution at 80-90 C. The laser scanned at 15-20  $\mu\text{m}/\text{sec}$  and had a power of 0.6-1.2 W. The results in [Fig. 42](#) shows the averaged tensile strength of these parts is

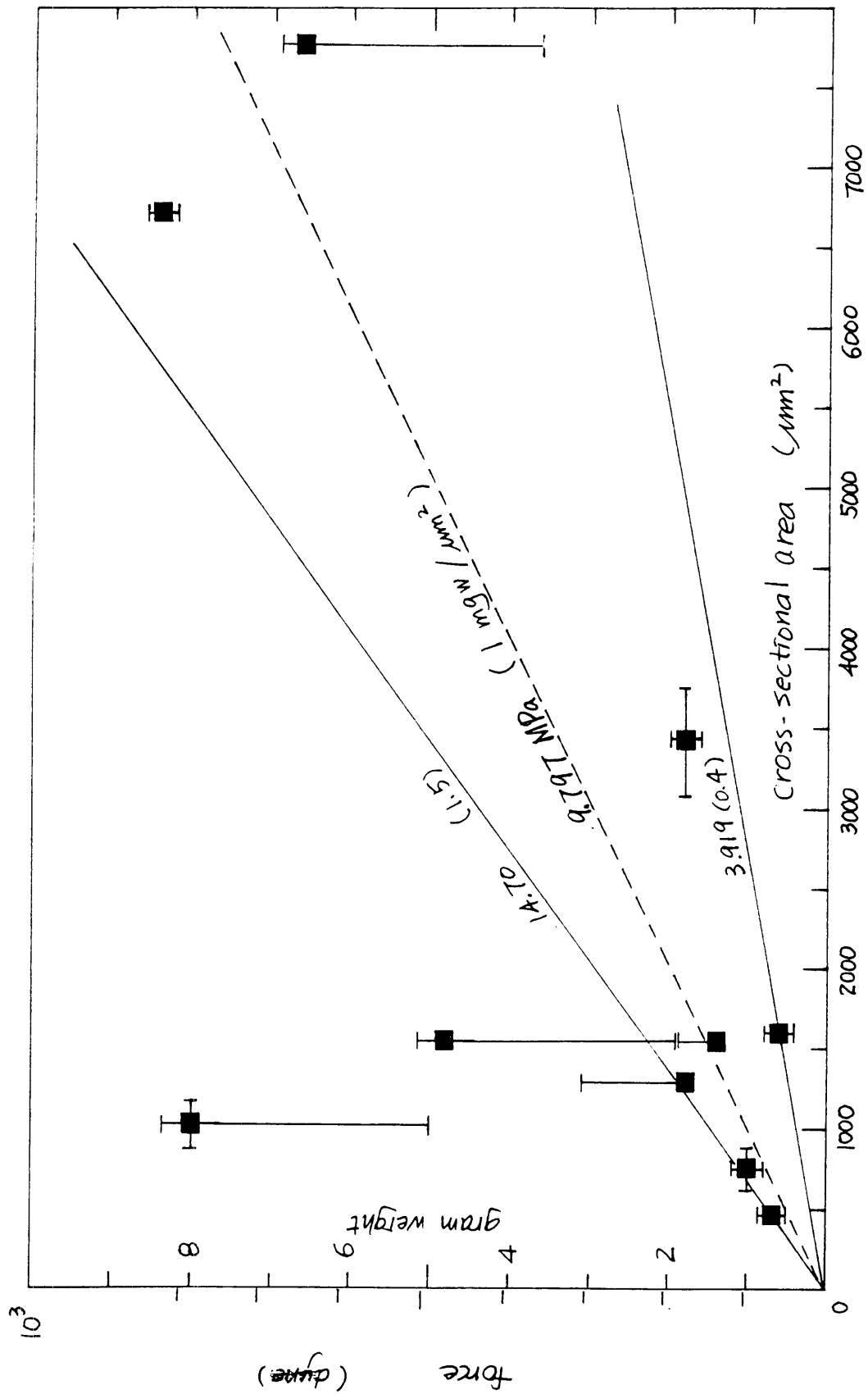


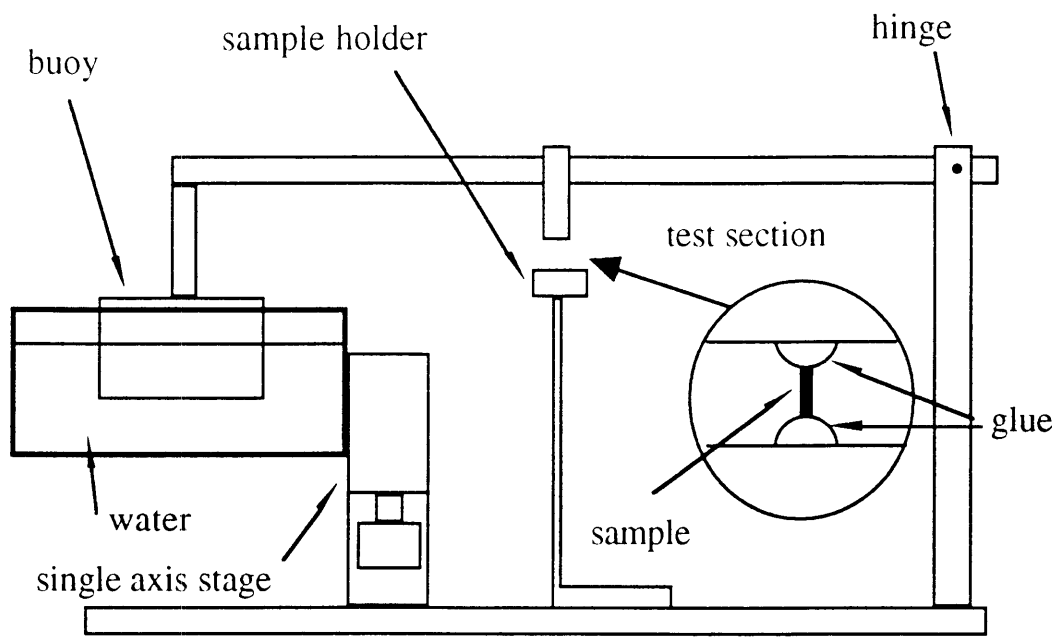
Fig. 42 Tensile strength of micro bars formed by Sequential Photo-Electroforming; no post treatment

around 10 MPa. This value is compared with some related strength data in [Table 2](#). The strength of the part is close to the pull strength of electroless Ni on ceramic substrate, and is stronger than the pull strength of nickel film sputtered or evaporated on glass substrates. The value is also close to the maximum tensile strength of fired SiC pellet, which was determined by 3-point bending as described in section 3.2.1. Therefore, the strength is probably a combination of Ni adhesion on SiC and the bonding among SiC particles due to the firing step in the Sequential approach. As already mentioned in section 3.2.1, it is believed that the firing step causes the bonding of silicon dioxide on the surface of SiC particles being dry pressed into contact with each other. It should be pointed out that those test samples were not post treated in any way. The strength of electroless Ni deposits itself and the strength of sintered SiC are both very high. Therefore, a post treatment of more electroless Ni plating can be applied to increase the strength of those parts. Also, a post sintering process can be developed, after a systematic study on the effect of sintering on Photo-Electroformed parts. Related strength data are listed in [Tab. 2](#) for reference.

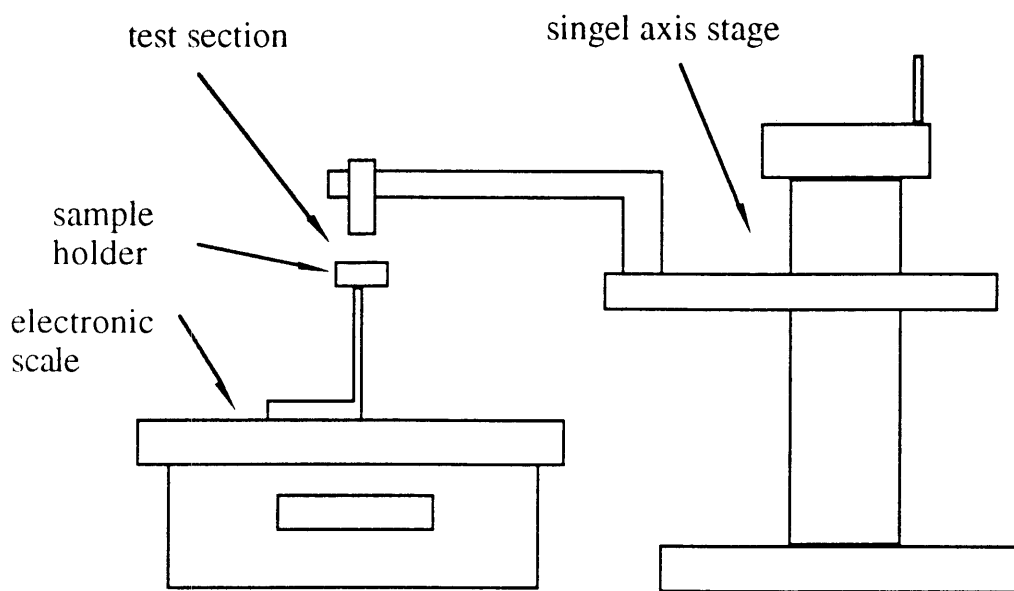
Two apparatus were used to measure the tensile strength of those lift-off line segments. The first apparatus is shown in [Fig. 43\(a\)](#), where a water-buoy setup was used as a spring and the immersion depth of the buoy in the water was pre-calibrated with known weight into force. A sample was glued on both ends at the test section and tension was applied by raising the water tank until the sample was broken. The breaking force was then read out from the change of immersion depth of the buoy. A second apparatus used an electronic weight scale and the breaking force was read out from the scale at the moment of breaking directly, as shown in [Fig. 43\(b\)](#). The second apparatus gave more precise numbers but required more careful reading. [Fig. 44](#) shows a picture of the broken cross-section of a typical sample.

Table 2 Strength of Photo-Electroformed parts in comparison with other related materials

material	substrate/structure	strength	reference
Photo-Electroformed bars	Ni/SiC	~10 MPa (tensile)	this work
electroless Ni	alumina plate	7-29 (pull)	Honma & Kanemitsu 1987
sputtered Ni	glass plate	7-10 (pull)	Dini 1993
evaporated Ni	glass plate	<0.7 (pull)	Dini 1993
SiC pellet (dry pressed & air fired)		~10 MPa (fracture)	this work
SiC (sintered 2% porosity)		450-520 (fracture)	Richerson 1982
electroless Ni deposits		200-900 MPa (tensile) depending on %P	Parker 1992



a.



b.

Fig. 43 Apparatus for tensile test

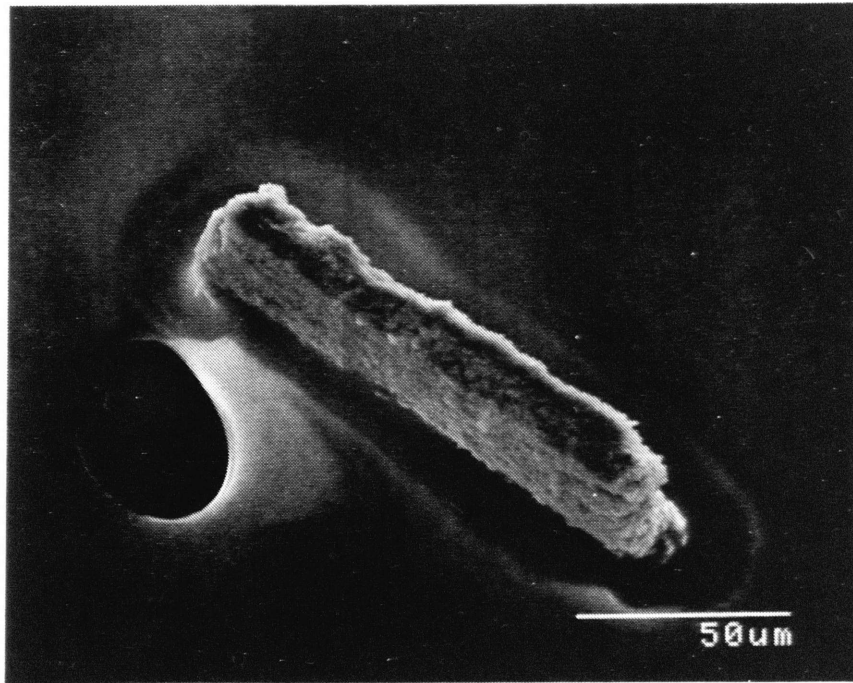


Fig. 44

SEM photo of a typical line segment formed by Photo-Electroforming after tensile test; SiC/Ni held by epoxy glue

## 5.4 Material Flexibility

Although the feasibility of Photo-Electroforming has been demonstrated by using SiC and Ni powders, the process actually allows for various ceramics and metals. A suitable layer material should meet three compatibility requirements: optical compatibility, which means the light absorptance in the laser spectra is high enough; catalytic compatibility, which means the solid accepts electroless metal; and temperature compatibility, which requires the material to be able to tolerate the heating by laser beam. Many materials can meet these three requirements with using argon ion laser and various electroless plating solutions.

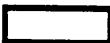
A list of materials is collected in [Fig. 45](#) to show their optical compatibility with the Photo-Electroforming process. At least five types of electroless plating solution can be used for photo-metallization, and among them electroless palladium, silver and platinum have the widest operation window because their colorless nature does not hamper the passage of the laser beam. Electroless nickel and copper have narrower windows, yet various ceramics, such as SiC, AlN, and Si<sub>3</sub>N<sub>4</sub>, and metals, such as Ni, Cu, Co, and Ti, are found to be compatible in these windows.

The catalytic issue is more complicated as different materials may have different catalytic properties toward different electroless solutions. In general, however, non catalytic metal can be activated by immersion in dilute palladium chloride and non metallic material can be activated by a stannous/palladium chloride pretreatment. If any palladium chloride activation is required for laser induced electroless plating, then this activation must be removed before a second electroless plating, e.g. by a very dilute acid, or the second plating will not have selectivity. However, if the second plating is done by electrolytic plating, then there will be no selectivity problem. Experiments showed that palladium activated surface is not conductive enough for electrolytic plating and electrolytic plating becomes possible only when a thin layer of electroless metal covers the surface. Details of

Wavelength (μm)                      0.2   0.3   0.4   0.5   0.6   0.7   0.8   0.9   1.0

---

Spectra window for Ar laser

electroless Ni solution                                                                  1 cm transmittance > 50%

electroless Cu solution                                            1 cm transmittance > 50%

electroless Pd, Ag, and Pt                      (colorless)

Absorptance

α-Al <sub>2</sub> O <sub>3</sub> high purity	 0.75-0.95
SiC	 0.9-0.95
AlN	 0.7-0.8*
BN	 0.2-0.7
Si <sub>3</sub> N <sub>4</sub>	 0.6-0.8
Si	 0.5-0.9*
SiO <sub>2</sub>	 0.1-0.3
Ni	 0.34-0.46*
Cu	 0.88-0.97*
Co	 0.7-0.8*
Mo	0.65-0.75 (solar spectrum)
Ti	 0.5-0.8*
W	 0.8-0.98*

---

\* determined from reflectance

Fig. 45 Optical compatibility of various materials for Photo-Electroforming (see Appendix 9 for source of data)

these experiments are described in Appendix 10. It was found, section 3.2.1, that laser enhanced electroless plating works on non pretreated silicon carbide, while a hot bath of the same solution below 100 C does not. At least one other ceramic, aluminum nitride, has been reported to possess a similar property [Morita 1988]. This "laser activation" phenomena can best serve the process of Photo-Electroforming, since no pre-activation is necessary and the second plating selectivity can be easily achieved. It is speculated that large specific area and high surface temperature is the cause of "laser activation", and other ceramics may have a similar property.

In section 4.2.3, a laser enhancement transition temperature of 200-300 C was identified. As a result, in principle, materials capable of tolerating 300 C can be used. Most ceramics and metals certainly qualify. Some high temperature polymeric materials also qualify. For example, cured polyimide can tolerate up to 500 C without changing its major properties [Wolf 1990, chapter 4].

## **5.5 Comparison of Sequential and Continuous Approaches**

To make a comparative evaluation between the Sequential approach and the Continuous approach, based on process characteristics, the major issues may be rate and facility cost, since the material strength and material flexibility of both approaches are quite the same.

It has been shown, in section 5.1, that the Sequential approach allows for a laser scanning speed more than two orders of magnitude higher than the Continuous approach, due to the long cooling period associated with the Sequential approach. On the other hand, the Continuous approach has the advantage of continuous operation without interlayer delay. Considering the complete process sequence, time saving due to high scanning speed of the Sequential approach may still beat the advantage of the Continuous approach in layer deposition and second plating, since layer deposition and second plating in the Sequential approach takes less than 30 min. per layer, which includes 10 min. powder spreading, 10

min. firing, and 10 min. second plating, while the photo-metallization in the Continuous approach may take much longer, if the pattern is large and complicated.

To further understand the characteristics of these two approaches, the layout and structure of a multilayer substrate used on IBM multi-chip TCM (thermal conduction module) was used as a benchmark. This package substrate is 90 mm on each side and has 130 m of internal wiring distributed on 33 layers [Young 1986]. Using the wiring length and the layer number as a benchmark, and based on the maximum scan rates, 25 cm/sec for Sequential approach and 1 mm/sec for Continuous approach, from section 5.1, and assuming a interlayer operation time of 30 min. for Sequential approach and negligible interlayer operation time for the Continuous approach, the following process cycle time was estimated,

	Sequential	Continuous
interlayer operation	30 min. x 33 =990 min.	fast
patterning	8.7 min.	2167 min.
cycle time	~17 hr	~36 hr

The facility cost associated with the Continuous approach is obviously higher because of the need of a fluid system capable of pumping electroless plating solution at elevated pressure. Higher pressure is preferred due to two issues: to better hold the powder bed and to achieve better resolution. The cell pressure used in this work is around 150-350 psi. Higher pressure may be necessary to improve resolution.

In conclusion, the Sequential approach may be a more general manufacturing process for micro-structures and devices than the Continuous approach, in terms of processing rate, resolution, and operation cost. The Continuous approach may find its

niche in making small quantity objects with large layer numbers, because in these cases the patterning time in each layer is small and the continuous powder deposition can show its advantage.

## **5.6 Comparison of Photo-Electroforming and Existing Techniques**

In this section, Sequential Photo-Electroforming is compared to current poly-Si techniques for micro-electro-mechanical-systems, LIGA process, and photo-sensitive polyimide process, in terms of major process characteristics.

First, the process throughput of Sequential Photo-Electroforming in making micro-structures is potentially higher than that of the poly-Si technique. [Fig. 46](#) shows a comparison of simplified process flows of these two techniques, with important process features highlighted. Photo-Electroforming has a simpler and faster layer deposition step which can build up several microns to tens of microns of powder in one step, while the low pressure chemical vapor deposition (LPCVD) step for growing poly-Si is not only slow ( $\sim 0.8 \mu\text{m/hr}$  at 600 C) but also involving toxic silane [Wolf & Tauber 1986]. Photo-Electroforming does not require a planarization step, while the poly-Si technique not only needs one but may also need additional patterning and etching to make sure the filling does not cover the un-completed poly-Si pattern in the previous layer, when building a real 3-D structure. Growing the filling, usually phosphosilicate glass (PSG), is another slow oxidation step ( $0.1\text{-}1 \mu\text{m/hr}$ ) [Muller et al. 1988], although plasma enhanced CVD (PECVD) can increase the rate to  $3.6 \mu\text{m/hr}$  [Gorczyca et al. 1985]. Spin-on glass (SOG) process provides higher throughput. However, the baking time is still around 0.5-1 hour per layer [Wolf 1990, chapter 4]. As to patterning time, it has been shown in section 5.5 that, based on the experimental 25 cm/sec scan rate, a fairly complicated line pattern in a 9 cm by 9 cm area can be defined in minutes. As a result, the patterning time in Sequential Photo-Electroforming is not the rate limiting step. In summary, the cycle time of the whole

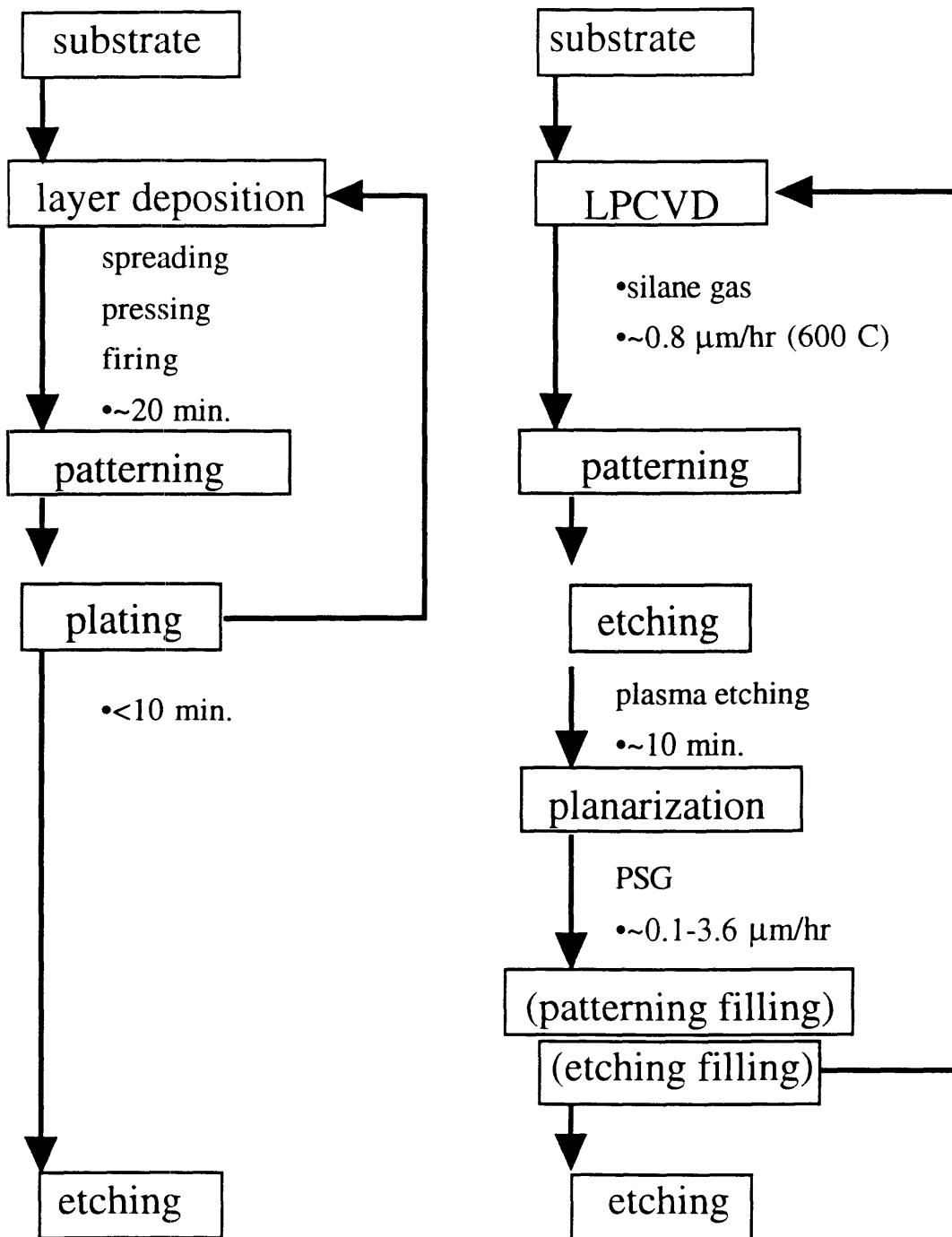


Photo-Electroforming

Poly-Si Technique

Fig. 46 Comparison of Sequential Photo-Electroforming and Poly-Si technique

process of Photo-Electroforming could be shorter than poly-Si technique. For complicated patterns or higher production volume, the batch feature of photolithography may become advantageous.

The planar process resolution of Photo-Electroforming will not be as fine as those obtained from photolithography because of the bubble diverging and thermal diffusion effect, but a resolution of several micrometers should be achievable. As to the layer thickness, Photo-Electroforming can deposit 5-10  $\mu\text{m}$  material at one time on each layer, which is thicker than that of poly-Si technique. For parts of high aspect ratio, layers can be stacked to reach larger thickness. In general, Photo-Electroforming has coarser resolution than poly-Si technique in all directions. But many micro-structures and devices can still be built with this resolution, and the larger layer thickness may be used to create structures not suitable for poly-Si techniques.

In terms of material flexibility, Photo-Electroforming has a very wide range of available materials, including metals and ceramics. The ability to create metal matrix ceramics, such as the SiC/Ni parts created in this work, is a special advantage of Photo-Electroforming over poly-Si technique. One advantage of the poly-Si technique which Photo-Electroforming lacks is the potential ability to fabricate transistor-based micro-circuits on the same substrate of the micro-mechanical devices. However, a micro-circuit-chip can always be bonded to a Photo-Electroformed micro-device later.

Table 3 summarizes the comparison of Photo-Electroforming (represented by Sequential approach) and existing techniques in terms of major process characteristics. Photo-Electroforming costs less than poly-Si technique, and its cycle time could be shorter than poly-Si technique, provided that pattern complexity does not make laser patterning a rate limiting step. Its planar resolution does not compete with photolithography, but its layer thickness can be thicker than that of poly-Si technique. Its biggest advantage is the fully 3-D geometric flexibility, which is more flexible than any other techniques. In

Comparison of Photo-Electroforming and other existing techniques

	Bulk Micromachining	Wafer Bonding	Surface Micromachining	LIGA or SLIGA	Photo-Polyimide	Photo-Electroforming (Sequential)
Rate per layer --patterning --growth or etching	masking + patterning 0.1-10 $\mu\text{m/s}$	masking + patterning $\sim 0.8 \mu\text{m/hr}$	masking + patterning $\sim 100 \mu\text{m/hr}$ (Ni)	masking + patterning $\sim 100 \mu\text{m/hr}$ (Ni)	masking + patterning $\sim 100 \mu\text{m/hr}$ (Ni)	scanning 10-20 $\mu\text{m/hr}$
Resolution --planar --layer thickness	$\sim 100 \mu\text{m}$ $\sim 10 \mu\text{m}$	$\sim 1 \mu\text{m}$ 1-2 $\mu\text{m}$	$\sim 1 \mu\text{m}$ 1-50 $\mu\text{m}$	$< 1 \mu\text{m}$ 1-400 $\mu\text{m}$	$\sim 1 \mu\text{m}$ 1-50 $\mu\text{m}$	$\mu\text{ms}$ 5-10 $\mu\text{m}$
Material	Si	Si	poly-Si, Si <sub>3</sub> N <sub>4</sub> , W, Ni	Ni, Cu, platable metals	Ni, Cu, Ceramics	laser
Major equipment		LPCVD etc.	X-ray source			
Geometric flexibility --planar 2D --high aspect ratio 2D --fully 3D	×	×	×	×	×	×
Reference	Wolf & Tauber 1986	Peterson 1988	Muller 1988	Guckel 1991	Frazier & Allen 1992	This work

summary, Photo-Electroforming does have the potential to become an alternative process for making micro-electro-mechanical systems, especially for making devices and structures with complex 3-D geometry and a resolution requirement of several micrometers.

## 6. Applications

### 6.1 Multilayer Electronic Packaging

Photo-Electroforming can be used to create multilayer electronic packages that offer unique features. In [Fig. 47](#), the interconnection pattern is defined by photo-metallization layer by layer. For improved performance, a porous medium with low dielectric constant can be used. The defined pattern is then joined and enhanced by the second stage plating, for example either electroless or electrolytic copper. In the next step, a binder material, such as low dielectric constant liquid polymer, is infiltrated into the powder bed thereby forming an integrated substrate with multilayer conducting traces inside. Selective etching and plating can then be applied to create pads on the substrate surface. One of the key advantages of this approach is that the vias are created *in situ* as an integral part of the process. It has been estimated in section 5.5 that, as a benchmark, a multilayer substrate for IBM multi-chip TCM (thermal conduction module), which is 90 mm on each side and 6.55 mm thick and has 130 m of internal wiring distributed on 33 layers, can be fabricated in 17-36 hours by Photo-Electroforming.

In order for Photo-Electroforming to work, conductor traces must be made of copper, nickel, or silver. These metals are mostly good conductors. Traces made of metal matrix materials have lower effective conductivity than pure metal lines, and this may present a problem for packaging. However, according to existing theory[Newman 1978], it is estimated that 75% conductivity of pure metal can be obtained if the volume fraction of metal is increased up to 80% through the use of a highly porous support material.

Layer materials used for chip substrates must satisfy requirements for electronic packaging as well as requirements for Photo-Electroforming process. Among electronic requirements, thermal conductivity, dielectric constant, thermal expansion coefficient, and melting point are the major issues. Silicon carbide, the major layer material used in this

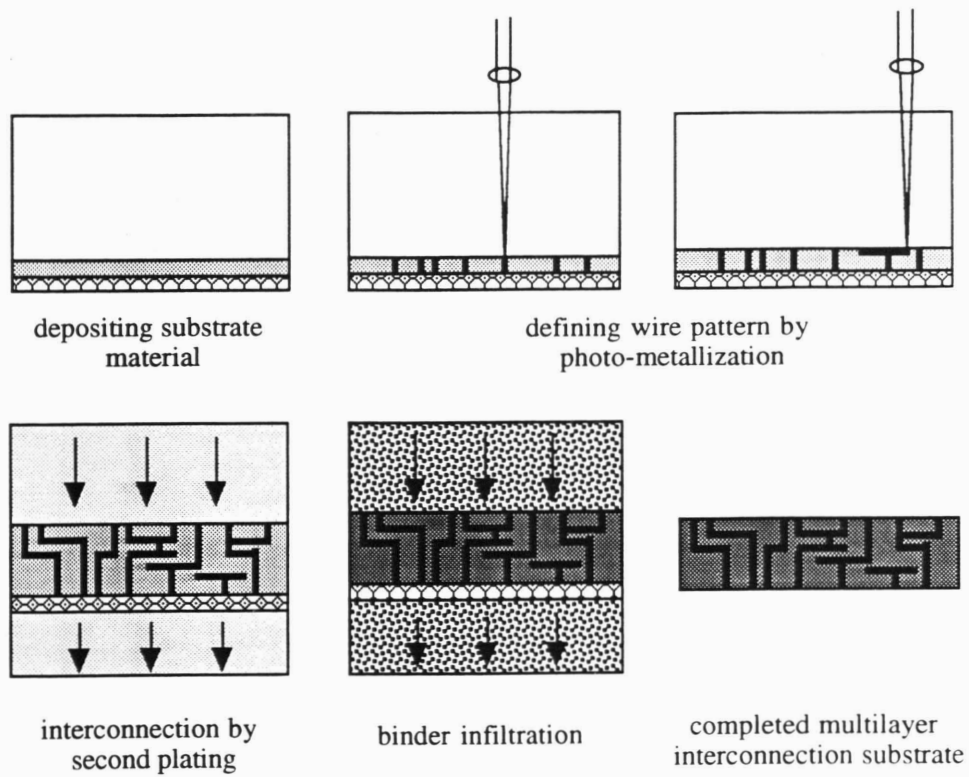


Fig. 47 Making multilayer electronic package substrate by Photo-Electroforming

research, has good thermal conductivity and is actually considered by researchers as a candidate for substrate material [Schwartz 1988], despite that its high dielectric constant may limit its applications. In the field of thick-film technology for making circuit substrates, glass materials capable of co-firing with copper, nickel, or silver conductors have been developed and used for years [Cote 1988]. For example, lead borosilicate glass has a relative dielectric constant of 6-9 and can be a good insulator material [Ulrich 1974]. In general, glasses can be activated through Sn/Pd pretreatment to accept electroless Cu or Ni. The absorptance of blue light (argon ion laser) of glass is usually low (see Fig. 45). However, since a mixture of materials is usually used for thick-film insulator, the optical property of the material may be adjusted accordingly. Another approach is using a different frequency, e.g. CO<sub>2</sub> laser, for glass, which usually absorbs IR light.

## **6.2 Micro-Electro-Mechanical Systems**

In addition to making conductive traces for interconnections, Photo-Electroforming can also fabricate micro-electronic devices such as chip capacitors, inductors, and resistors. The geometric flexibility of Photo-Electroforming can create electrodes of capacitors with complex shapes as well as 3-D coils for inductors with or without ferromagnetic cores. By adjusting the metal/non-conductor volume ratio in Photo-Electroformed lines, resistors can be created.

By Photo-Electroforming, micro-mechanical springs, flexures, and membranes with complex geometry can be fabricated. Using the capability to electrolytically plate different metals in different locations and the ability to remove thin layers of unmetallized powder from between structures, integral assemblies of micro-mechanical parts, such as rotary bearings or gear trains can also be produced by Photo-Electroforming. Applications may include tiny surgical tools, micro-manipulators, micro-optical devices and others. A key feature of Photo-Electroforming for such applications is the ability to fabricate devices from materials with good structural properties.

Photo-Electroforming can be used to create resistance temperature detectors (RTD) by plating platinum on wires distributed in non conductive substrates. Strain gages can be built similarly. By making use of the ferromagnetic property of nickel and its alloys, micro electromagnets, and magnetic sensors can also be built. The cores can be created by plating nickel. The coils around the cores can be made by plating copper. Sensors made by Photo-Electroforming can be integrated with VLSI or with MEMS made in silicon by flip-chip bonding onto a Photo-Electroformed device with contact pads.

Photo-Electroforming is also capable of fabricating actuators, such as micro electromagnetic motors. [Fig. 48](#) shows a possible process of producing a micro electromagnetic motor by Photo-Electroforming. The geometry of the coils and the magnet cores are first defined by photo-metallization. Electrolytic copper is used to create the coils and nickel is used to create the cores. In the fourth step, a binder material is infiltrated into the powder bed to bind it into an integral substrate. A hole is then opened by punching, laser drilling or masked selective etching to create a stator assembly. A separate rotor and shaft assembly is created by Photo-Electroforming and the two assemblies are then bonded together to form the motor. Other actuators such as solenoids are possible

### **6.3 Micro-Tooling**

Photo-Electroforming can be used to build tools and dies for making small-sized, complicated, tight tolerance parts. An example is the fabrication of small inserts for injection molding of precision components. Tools which are composites of nickel and ceramic made by Photo-Electroforming may provide excellent physical properties.

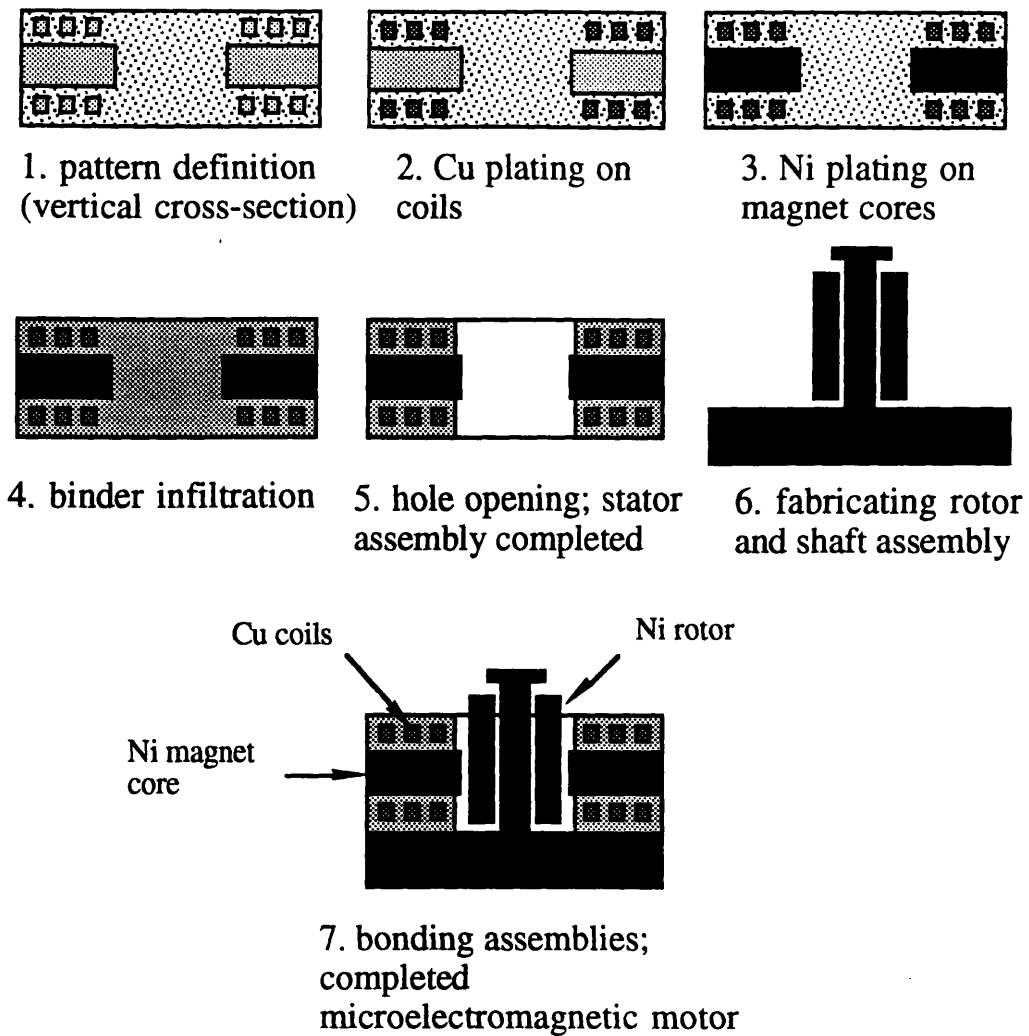


Fig. 48

Making micro-actuator by Photo-Electroforming

## 7. Conclusions

A new manufacturing process for making micro-electro-mechanical systems (MEMS) called Photo-Electroforming was conceived, demonstrated, and studied. The process is capable of creating micro-structures with fully 3-D geometry and various materials at a moderate cost. The motivation to develop such a new process came from the emergence of a "small-scale industry" in recent years. It was recognized that technologies in three fields, micro- sensors and actuators, electronic packages and connectors, as well as "nanotechnologies" such as scanning tunneling microscopes, will begin to promote a need for micro-mechanical structures or parts, and peripheral components and devices for micro-chips or nanomachines in various applications. However, current techniques for making micro- structures or devices were originally developed for integrated circuit (IC) fabrication, which carry with them three major limitations: geometric limitation, material limitation, and high facility cost. Therefore, the goal was to develop a novel technique for manufacturing MEMS which has fully 3-D geometric capability, high material flexibility, and moderate cost.

Three basic principles were used as a guideline for creating and developing the basic process concept: (1) building up material by "additive-layer architecture" to achieve fully 3-D capability; (2) defining geometry by a photo induced property change mechanism; and (3) forming part by a joining step which has selectivity on the defined geometry of property change. A basic process concept called Photo-Electroforming was conceived, and its various process sequences were developed based on the basic principles. The feasibility of each possible process sequence (the feasibility of creating fully 3-D geometry) was studied. The process characteristics, rate, resolution, material, and strength, of feasible process sequences were investigated, and a comparison of the new process and the current micro-machining techniques was made based on these data. Potential applications were discussed.

In the basic process concept of Photo-Electroforming, parts or patterns were built by an additive process that defines geometry by depositing non conductive powder in layers and creating regions of selective conductivity by a photo-metallization mechanism. The metallized (conductive) region is then joined by a second plating into an integral part. This “additive-layer architecture” allows for creation of fully 3-D geometry, in contrast to the planar process used in the IC technology. The combination of laser-metallization and electroplating enables production of parts with high accuracy and fine resolution.

Three photo-induced mechanisms were identified as possible candidates for the photo-metallization step: (1) laser enhanced electroless plating, (2) photo-induced plating on semiconductor immersed in an electrolyte solution, and (3) photo-induced metallization of silver halide. The feasibility of each of these mechanisms was studied. In the method of semiconductor, experiments using p-type silicon as layer material and copper sulfate solution as plating electrolyte were performed. Photo-metallization on silicon wafer with a metal, usually Cu, counter electrode was successful. On particles, however, the photo-metallization effect was less significant. It is speculated that this decrease of quantum efficiency was caused by the increase of number of excess surface states per unit volume as solid size decreases. In the method of silver halide, both silver bromide powder and thin film made from wet chemical reaction were tested. Pure silver image patterns were created on silver halide by selective exposure in a developer. However, the pattern was easily destroyed by the following fixing step. It is speculated that the very fine silver particles were carried away with the unexposed silver bromide being dissolved into the fixer. The most feasible mechanism was laser enhanced electroless plating. Using an argon ion laser beam with spot size 12  $\mu\text{m}$  and commercial electroless plating solutions, Cu and Ni lines of width 10-22  $\mu\text{m}$  were created on pellets made of 1  $\mu\text{m}$  silicon carbide powder, at various scanning speeds.

Feasibility of the new process was demonstrated by using ceramic powder (SiC) and metal powder (Ni and Cu) as the layer material and by using laser enhanced electroless copper and nickel plating for selective metallization. The problem of laser enhanced electroless plating was that the laser induced ejection force, caused by sudden local boiling and by the continuous formation of hydrogen gas bubbles, tends to disturb the powder bed. Two methods of powder deposition, sequential and continuous, were developed to solve this problem, and the two corresponding process sequences were called the Sequential approach and the Continuous approach respectively.

In the Sequential approach, an ex-situ layer buildup scheme was applied to bond every new layer to the previous one by dry pressing and short firing. SiC powder was used as an example. By dry pressing 1  $\mu\text{m}$  SiC powder at 24-32 Kpsi followed by air firing at 800 C for 10 min., a bonding between particles which is strong enough to resist the ejection force yet can be selectively etched away in the final step was created. It is believed that the bonding of silica on the surface of SiC particles caused this effect, as the bonding can be released by etching in boiling potassium hydroxide or hydrofluoric acid, both etch silica efficiently. An alternative procedure was to oxidize the loose powder by firing in air for at least 15 min., and then dry press the powder and fire it in a noble gas such as helium. This procedure was used to bond add-on layers to the base pellet in order not to oxidize the metal patterns underneath. By Sequential approach, single-layer and dual-layer patterns were created on SiC pellets and add-on layers, and then a boiling potassium hydroxide was used to etch the unmetallized powders to reveal stand-alone parts. These parts were made of nickel/silicon carbide composites, with overall sizes from 75-100  $\mu\text{m}$  were created. Combining the capabilities of pattern formation, selective etching, and interlayer bonding, the basic elements for creating fully 3-D geometry were demonstrated. It was also found that laser enhanced electroless plating works on non pretreated 1  $\mu\text{m}$  SiC particles, but a hot bath immersion does not. By applying this

property, the material preparation procedure and the 2nd plating step were simplified. This "laser activation" is probably caused by thermal activation due to local superheating.

In the Continuous approach, a downward flow drag was used to hold the particles on a porous base so the laser induced gas bubbles do not disturb the powder bed. Pressurization is required to force the solution to flow through the porous powder bed and can also reduce the size of gas bubbles thereby further decreasing the disturbing effect. A flow-through cell system was constructed to investigate issues of this approach. Through in-situ observation, it was found that a minimum chamber pressure of 70 psi and a flow velocity of 5 cm/sec was required to hold the 5  $\mu\text{m}$  Ni powder used in the experiments, when the 12  $\mu\text{m}$  focused laser spot was of 0.3W. Crude pattern definition was demonstrated. A stand alone single layer bar and interlayer bonding were also created by direct bonding of laser induced electroless Ni deposits. A whisker structure was frequently observed in the Continuous process. It was determined that a continuous laser exposure at the tip of any protruding deposits might cause a continuous growing of a whisker. A dual-beam optics which brings two half-power beams to intersect each other at their focal points, thereby reducing the dimension of the full power zone, solved this problem.

The mechanism of laser enhanced electroless plating was investigated with the aim of understanding parameters controlling process rate and resolution. Due to the complexity of the process, indirect observation and order of magnitude estimation had to be performed. However, the data and evidence was significant enough for drawing useful conclusions. A method of observing morphology of Ni-film coated on a glass sample was applied to estimate the surface temperature under a focused laser beam scanning through samples immersed in electroless plating solution, and to relate laser power to sample temperature. Thus, an indirect method of changing reaction temperature was available. From the observation that deposition thickness was almost constant, it was deduced that laser enhanced electroless plating rate is insensitive to surface temperature in a wide range of

apparent laser power density, 1-10 GW/m<sup>2</sup>. The magnitude of the deposition rate was determined from size of deposits and total plating time, each estimated in separate experiments, to be in the range of 0.6-3 μm/sec, with an occasional spike forming rate of 6-10 μm/sec. It was found that this rate is very possibly controlled by mass transfer, which is strongly related to hydrogen bubble formation, and could be explained by a bubble displacement model. In summary, laser beam heats up the sample surface and when the surface temperature exceeds a transition temperature, which was determined to be around 200-300 C, enhanced electroless plating occurs and the deposition becomes mass transfer controlled. With the knowledge of this transition temperature, laser induced surface temperature on SiC samples was able to be estimated.

The major process characteristics of Photo-Electroforming were studied. The patterning rate of Sequential Photo-Electroforming is mainly controlled by heat transfer, because it was observed that electroless plating continues during a cooling period long after the laser exposure. The resolution is mainly controlled by the diverging effect of hydrogen bubbles generated together with electroless plating. The maximum scan speed achieved was 24 cm/sec, with a 12 μm beam spot at 1.5 W laser power in electroless Ni on SiC. The finest planar resolution achieved with the same beam spot size by electroless Ni on SiC was 22 μm; and 10 μm by electroless Cu. The layer thickness was 5-10 μm. The maximum achievable scan speed in the Continuous approach was estimated to be around 1 mm/sec, which is limited by the mass transfer controlled deposition rate and by the lack of long cooling period plating due to effective flow-through convective cooling. The Sequential approach is concluded to be a more general manufacturing process for micro-structures and devices than the Continuous approach, in terms of processing rate, resolution, and operation cost. The Continuous approach, which has the advantage of continuous powder deposition but has a lower patterning rate, may find its niche in making small quantity objects with large layer numbers.

A study of major process characteristics, in comparison with existing IC-based poly-silicon technique, shows that Photo-Electroforming has fewer steps and each step requires less operation time and cheaper equipment. Therefore, Photo-Electroforming does have a potential to become an alternative process for making micro-electro-mechanical systems, especially for making devices and structures with complex 3-D geometry and a resolution requirement of several micrometers. Expected potential application areas, including multilayer electronic packaging, MEMS fabrication, and Micro-tooling, were discussed.

# Appendices

## A1: Experimental Details on Laser Enhanced Electroless Plating

### (a) Sequential Approach

The laser used was a Spectra-Physics 2016 argon ion laser. A laser focusing single lens for argon ion laser, product number 01 LFS o21 from Melles Griot, was used to focus the beam to 12  $\mu\text{m}$  spot size at a focal distance of 16 mm. Knife edge measurement confirms this spot size claimed by the vendor. For laser single lens, the spot radius can be expressed as, according to Melles Griot Optics Guide

$$w_o \approx \frac{4\lambda f}{3\pi w}$$

where  $\lambda$  is wave length,  $f$  is focal length, and  $w$  is radius of incident laser beam. The depth of focus defined at 5% increase of minimum spot radius is

$$DOF = \frac{0.32\pi w_o^2}{\lambda}$$

The substrates were prepared from 1  $\mu\text{m}$  SiC powder (Johnson Matthey, Alpha, 99.8%). The powder was first dry pressed into 1/2 in diameter and 2 mm thick pellets under a load of 5000 to 7500 lb. The pellets were then moved into a tube furnace preheated to 800°C in air and fired for 10 min. The electroless plating solutions were NI-429M Special from Enthone Inc. for nickel, and PC electroless Cu from Transene Co. Inc. for copper (see A8 for bath composition). The argon laser was chosen to match the transmission spectra of the plating solution. The laser frequency was set at 488 nm which corresponds to 95% transmission at a depth of 1 cm in the electroless nickel plating solution and 78% for electroless copper. Silicon carbide powder was chosen to match the beam frequency since SiC has an absorptance of 0.9 at 488 nm (see A9 or Fig. 45).

In standard electroless plating procedure, pretreatment of non conductive materials is required to catalyze their surface for accepting electroless deposits [Saubestre 1974]. The fired SiC substrate was first sensitized in stannous chloride solution (Transene Co. Inc., sensitizer solution C) and activated in palladium chloride solution (Transene, activator solution D). The sample was then immersed in electroless plating solution at a depth of about 4 mm and was exposed to the laser beam. The Cu/SiC lines in Fig. 4(a) were created at a laser power output of 0.8-1.0 W and a scanning speed of 530  $\mu\text{m}/\text{sec}$ . It was found that a power as low as 0.3 W can create satisfactory lines of width 10 to 15  $\mu\text{m}$ .

It was found that laser induced plating works even on samples without the standard Sn/Pd pretreatment. Nickel/silicon carbide lines with a width of 22  $\mu\text{m}$  were successfully created on the SiC substrates with a laser power 1.4 -1.6 W at a scanning rate as high as 25 cm/sec . We also found that immersing the samples in a hot bath of electroless plating solution results in a selective continuing metallization only on those metal/SiC lines. The finding of laser selective electroless plating on SiC suggests that either laser induced electroless plating has a mechanism different from traditional thermal explanation or the electroless plating process is very sensitive to high thermal power density, large specific area of the fine powder, or the powder surface quality. This finding is a great advantage for Photo-Electroforming because otherwise the Sn/Pd pretreatment will be necessary and the joining step by a second stage electroless plating will not be selective.

The square frame shown in Fig. 7(a) was created by utilizing the selectivity effect described in the previous paragraph. The scanning was done in the electroless nickel plating solution at a speed of 20  $\mu\text{m}/\text{sec}$  and with a power output of 1.4 W. After the sample was patterned, it was immediately transferred into a bath of the same electroless nickel plating solution at a temperature of 75-85°C. Electroless nickel deposition continued on the square pattern, but not on the non metallized portion. This second stage joining lasted for 10 min. The sample was then cleaned in distilled water before being subjected to

selective etching to lift the part. A boiling 20% potassium hydroxide solution was used as the selective etching agent which etches the silica holding the SiC substrate but does not attack nickel. [Horton 1988]

#### (b) Continuous Approach

Two flow-through cells were constructed for this research. The first cell was made of 316 stainless steel, with one window on top for vertical laser beam input and one window on the side for observation. The second cell, as shown in Fig. A1-1, was made of polycarbonate and aluminum, with two windows for input from two split laser beams and two observation windows, one on top and one on the side. The split beams intersect inside the cell at their focal points. A sketch of the setup is illustrated in Fig. 13.

The porous plugs were prepared from bonded alumina filter disks, obtained from Refractron Technologies Corp. of Newark, N.Y. A small porous base plate was machined from the disk and then glued to stainless steel seats to form a porous plug. Nickel Porous plugs were prepared by firing loosely packed 5  $\mu\text{m}$  spherical Ni powder in helium at 660 C for 35 min. or at 800 C for 15 min. and then gluing the fired porous piece to a stainless steel seat. It was found that EPOXI-PATCH™ glue gives acceptable result.

The flow-through circulation was powered by a 1/2 HP, 14.6 GPH, variable flow rate diaphragm metering pump from Hydroflo Corp. of Plumsteadville, Penn. A 10 cubic inch pulsation dampener was installed to smooth the flow.

#### (c) Sheet Approach

In order to assess the feasibility of the sheet approach of Photo-Electroforming, section 2.3.2, using selective electroless plating, a simple, macro-scale three dimensional part was made from nylon screens and nickel deposits.

Selective metallization was accomplished by immersing the screen in a shallow bath of electroless nickel plating solution (Enthone Inc., NI-429M Special) and then by

exposing it to a light source through a shadow mask. Nylon screens with 150  $\mu\text{m}$  openings were used as the nonconductive layer material. The thickness of the screens was 163  $\mu\text{m}$ . The shadow mask was made by cutting an opening of the desired shape on a piece of aluminum sheet. The light source was a 300 W Tungsten halogen bulb with an aluminum reflector, and the exposure was made at the focal distance of the light source.

Four steps were taken in the experiment. In the first step, the nylon screen was sensitized in stannous chloride solution (Transene Co. Inc., sensitizer solution C) and activated in palladium chloride solution (Transene, activator solution D). Next, the nylon screen was immersed in the electroless nickel plating solution, and the mask was placed close to the screen. The light source heated the screen and the solution selectively through the shadow mask and electroless nickel was plated on to the selected portion of the nylon screen. Fig. A1-2 illustrates the setup. Ten layers (or sheets) of selectively-metallized screens were made by this process. Fig. A1-3(a) shows the metallized discrete sheets. In the third step, selective electrolytic plating in a Watts bath (SEL-REX ELECTRO-NIC 10-03) was applied to join the layers. The first layer was joined to a nickel base plate which acts as the cathode. The second layer was placed on the first layer and then joined. By plating one layer at a time, a three dimensional part was built from ten layers of nickel-nylon material (the layers were electroplated one at a time as no continuous pumping apparatus was available at the time). In the final step, the part was fired at 500°C in air to burn out the unplated nylon. The resulted part is shown in Fig. A1-3(b).

For each layer, 30-50  $\mu\text{m}$  thick nickel was plated to the screen; the resulting height of the part was 1.8 mm. The exposure for electroless nickel plating was about 9 seconds, which corresponds to about 1000Å nickel at an electroless plating rate of 30  $\mu\text{m/hr}$ . The electrolytic plating was done at room temperature with an apparent current density ( i.e., based on the base plate surface area) around 0.03-0.05  $\text{A/cm}^2$ .

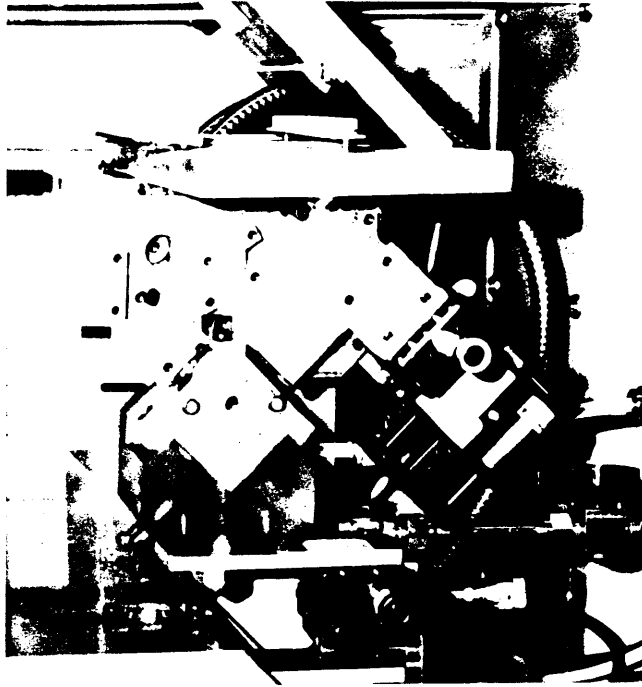


Fig. A1-1

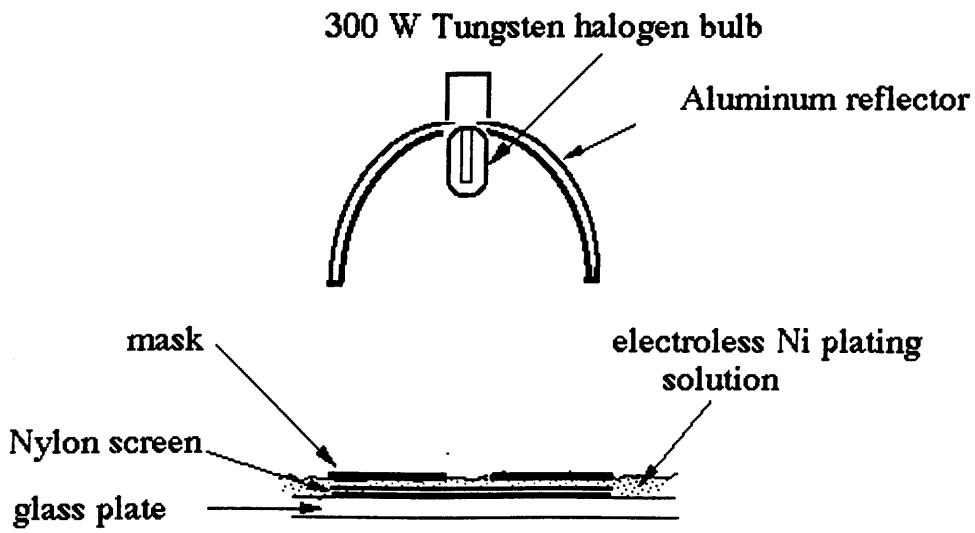
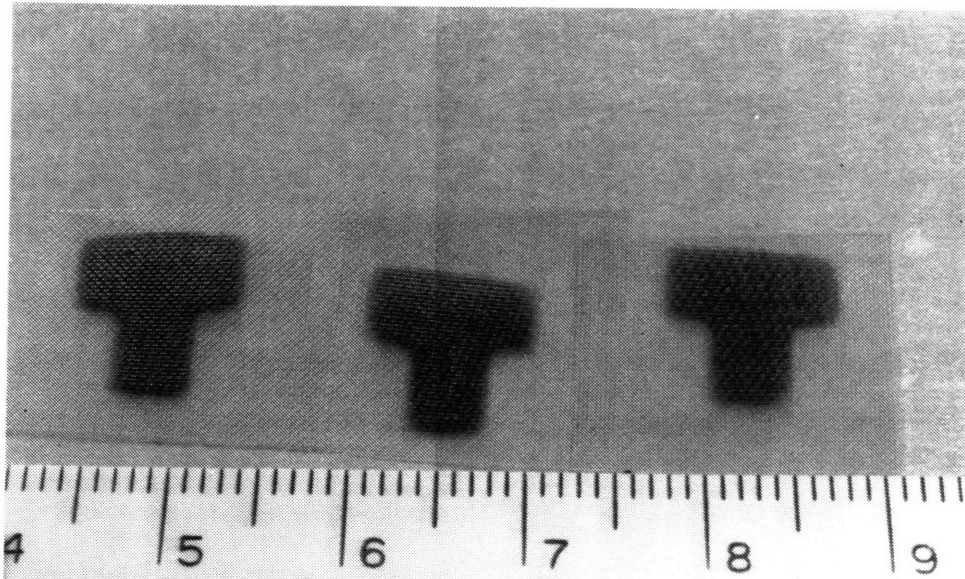
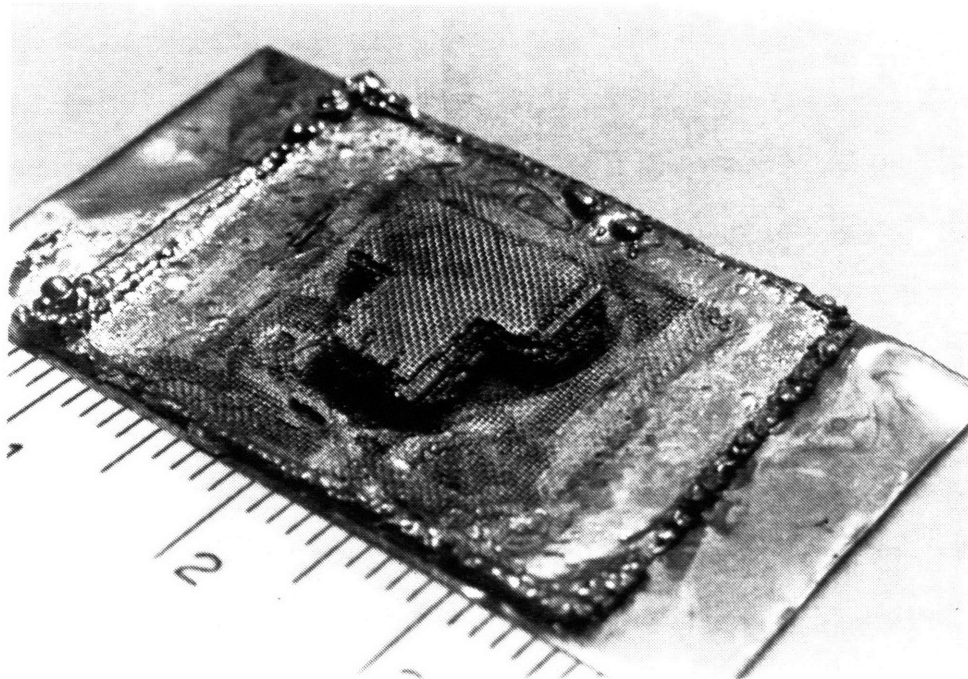


Fig. A1-2



(a)



(b)

Fig. A1-3

## A2: Experimental Details of Semiconductor Method

Semiconductor particles with a portion of their surface coated with a metal in ohmic contact are used as the layer material, as shown in Fig. 2. An electrolyte solution containing metal ions is used as working fluid. Incident light turns particles from partly metallized to fully metallized. In the final electroplating stage, those fully metallized particles can be plated into an integral object, while those partially metallized particles can not be joined together because there is not good electrical contact among them.

Experiments on pieces and particles of semiconductors were performed. A He-Ne laser of 5 mW power output was used as the light source. The plating solution used was an acid copper electroplating solution called SEL-REX Cubath XL from OMI International Corp. of Nutley, New Jersey (see A9 for composition). The substrate material is P-type single crystal silicon wafer of <100> orientation with 1-3  $\Omega$ -cm resistivity. The counter electrode was applied by sputtering a copper film, of a thickness from .5 to 1  $\mu$ m, to partially cover the surface of the wafer. Copper film can also be sputtered on the back side of the wafer. The semiconductor-metal contact was made ohmic by sintering in argon at 840-870 C for 2 min. The counter electrode can also be attached to the semiconductor piece through a wire which is bonded to an aluminum pad in ohmic contact with the semiconductor. Such a wire bonded structure allows for current measurement during the light-induced deposition. Evaporated aluminum on silicon wafer can be made into ohmic junction by firing in nitrogen at 450 C for 20 min. [Fig. A2-1](#) illustrates the idea. A typical current-voltage curve is shown in [Fig. A2-2](#). Under the illumination of a 1 mm beam of 5 mW red light, it was found that the deposition current density on the single crystal Si wafer is about 20 mA/cm<sup>2</sup>, which corresponds to a copper deposition rate of about 0.5  $\mu$ m/min., and the quantum efficiency (number of excited electrons divided by total incident photons) is about 8%. [Fig. A2-3](#) shows a photo-induced copper spot created on the surface of a silicon wafer. It was observed that, under the same exposure, the amount of copper on the

Si wafer with a metal counter electrode was more than that on the Si wafer without a metal counter electrode. In the particle size experiments, single crystal Si particles were prepared by breaking and grinding the Si wafer into small particles with a size of 1-2 mm. The particles were then etched in a mixture of nitric acid, hydrofluoric acid, and acetic acid (with a volume ratio of 6:1:1) for 1 min. to smooth the damaged surfaces. Counter electrode was applied by two methods. In the first method, the particles were placed on a piece of copper (or aluminum sheet) and the ohmic junction was formed by sintering in argon at 840-870 C for 2 min. (in the case of Al sheet, 650-675 C for 10-20 min.) Fig. A2-4(a) shows an Al sheet setup. Counter electrode was also applied by sputtering a copper film to cover one side of a particle. Fig. A2-4(b) shows several particles prepared by this method. By immersing these samples in the plating solution and exposing them to the laser, photo-induced copper deposition was observed on some samples, but the result was not always reproducible. This decrease of quantum efficiency at particle sizes is probably caused by the increase of number of excess surface states per unit volume as the solid size decreases. The excess states associated with the dangling bonds at material surface consumes most of the excited charge carriers and therefore only a small fraction of photo-electrons react with the ions from the solution to form metal atoms. If this efficiency decrease is due to increasing excess surface area to volume ratio, then single crystal particles with perfect surfaces must be prepared to make this method work. This is obviously a complicated task.

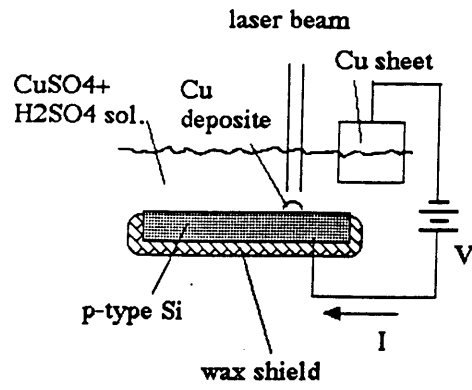


Fig. A2-1

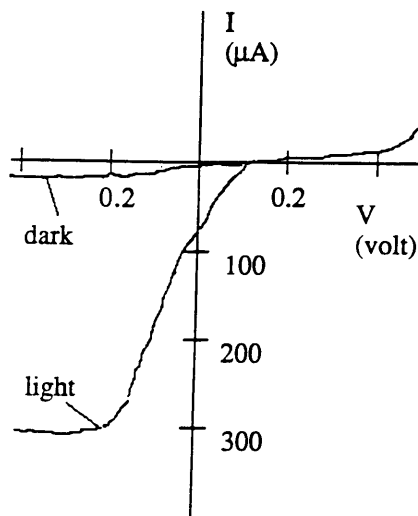


Fig.A2-2

fig.

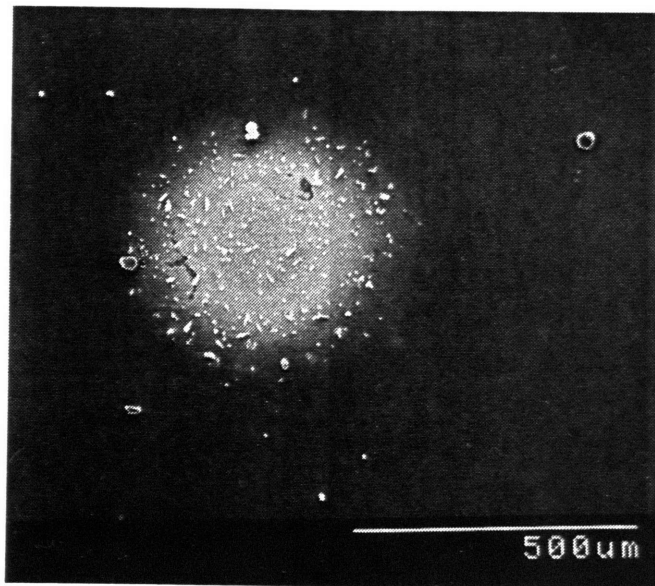
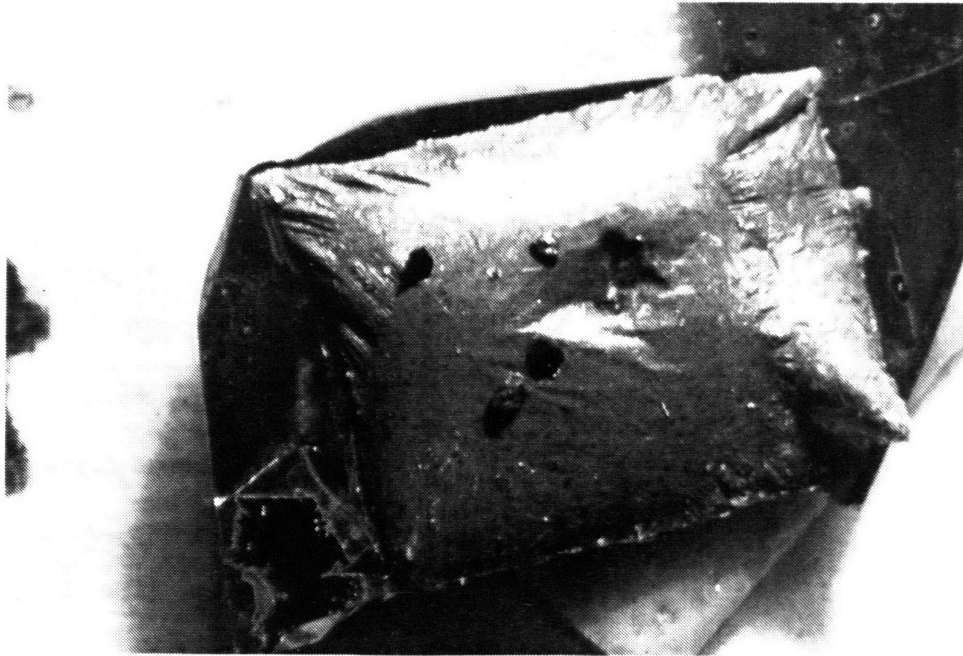


Fig. A2-3

(a)



(b)



Fig. A2-4

### **A3: Experimental Details of Silver Halide Method**

In this approach, silver halide particles or thin film is used as the layer material, and a photographic developer, such as vanadous salts or hydroxylamine [Carrol 1980], is used as the working fluid. The layer material is first immersed in the developer and then exposed to light selectively. In the exposed region, silver forms. The unexposed particles or the portion of the film is then dissolved away by a fixer, and the silver particles remains. A planarization material is then added to fill the void, unexposed region. This selective exposure process is repeated layer by layer until the part geometry is completely defined. The silver particles can then be joined into an integral part by a second plating. And finally, the planarization material is removed to reveal the part.

The silver bromide powder, 99.9% and very fine, was from Johnson Matthey. Silver bromide thin film was also used in the experiment. The film was prepared by mixing one drop of concentrated silver nitrate solution and one drop of potassium bromide solution on a spinning glass, followed by drying in air. This procedure can create a layer thinner than a layer prepared from the powder. The developer is a standard B&W developer from Spring Systems of Pawtucket, Rhode Island, and the fixer is Ilford multigrade fixer, ammonium thiosulfate based, from Ilford Photo of Paramus, New Jersey. The experiments were conducted in a darkroom, using a light bulb and a mask as the light source. Silver image patterns were created on silver bromide layer, either immersed in developer or being developed after the exposure. However, the patterns were easily destroyed by the following fixing step. It is speculated that the very fine silver particles were carried away with the unexposed silver bromide being dissolved into the fixer. To successfully exercise the fixing step, practical method have to be developed to dissolve the unexposed silver halide away without disturbing those tiny and loose silver metal. Since the size of silver halide grain is usually equal to or less than 1  $\mu\text{m}$ , the size of reduced silver metal particles must be on the sub-micrometer scale and therefore the practical difficulty in

handling them can be extreme. Another issue is the need of planarization after the fixing step because a second plating joins both silver particles and unexposed silver halide, as it becomes partially dissociated in water and is thus conductive.

#### A4: Thermal Conductive Model for Laser Heating

This is a simplified model for estimating temperature of a semi-infinite solid subjected to heating from a laser beam spot on the surface. The purpose of this estimation is to provide a supportive understanding of the experimentally estimated surface temperatures on samples used in this research.

Only conduction heat transfer in the solid is considered. Fig. A4-1 depicts the model. The case is in fact equivalent to an infinite solid sphere being heated at a central spot. Using a spherical coordinate and taking a thin shell  $dr$  as the control volume, differential heat balance in a time interval  $dt$  gives

$$\frac{\partial \dot{q}}{\partial r} dt = \rho c dT \quad (\text{A4-1})$$

where heat flux

$$\dot{q} = -k \frac{\partial T}{\partial r} \quad (\text{A4-2})$$

Combining eqn. (A4-1) and (A4-2) gives the governing equation,

$$\frac{\partial T}{\partial t} = \alpha \frac{\partial^2 T}{\partial r^2}; \quad \alpha = \frac{k}{\rho c} \quad (\text{A4-3})$$

where  $\alpha$  is thermal diffusivity of the solid. This is a 1-D thermal conduction equation.

It requires two boundary conditions and one initial condition to solve eqn.(A4-3). It is assumed that laser heat is supplied through a small semi-spherical ball with a radius equivalent to laser beam radius  $r_b$ . Therefore, heat balance at  $r_b$  gives b.c.1

$$\dot{Q} = -2\pi r_b^2 k \frac{\partial T}{\partial r} \Big|_{r=r_b} \quad (\text{A4-4})$$

and temperature at infinity gives b.c.2

$$T(\infty, t) = T_\infty \quad (\text{A4-5})$$

The initial condition is

$$T(r,0) = T_0 \quad (\text{A4-6})$$

Eqn. (A4-3)-(A4-6) can be solved by Laplace Transform (see, e.g. [Arpaci 1966, example 7-3]) to give the following solution,

$$\frac{T(r,t) - T_0}{\frac{p}{2k}} = \left(\frac{\sqrt{4\alpha t}}{\sqrt{\pi}}\right) e^{-(x/\sqrt{4\alpha t})^2} - x \cdot \operatorname{erfc}\left(\frac{x}{\sqrt{4\alpha t}}\right) \quad (\text{A4-7})$$

where p is effective input power density,

$$p = \frac{\dot{Q}}{\pi r_b^2}, \quad (\text{A4-8})$$

$$x = r - r_b, \quad (\text{A4-9})$$

and k is thermal conductivity. The effective input power can be estimated by

$$\dot{Q} = P \cdot a_b \cdot f_c \quad (\text{A4-10})$$

where  $a_b$  is the radiative absorptance of the solid surface,  $f_c$  is a correction factor to account for effect of solution absorption, bubble shielding etc., and P is the laser output power. The surface temperature at the laser spot  $T_s$  is (at  $x=0$ )

$$\frac{T_s - T_0}{\frac{p}{2k}} = \frac{\sqrt{4\alpha t}}{\sqrt{\pi}} \quad (\text{A4-11}).$$

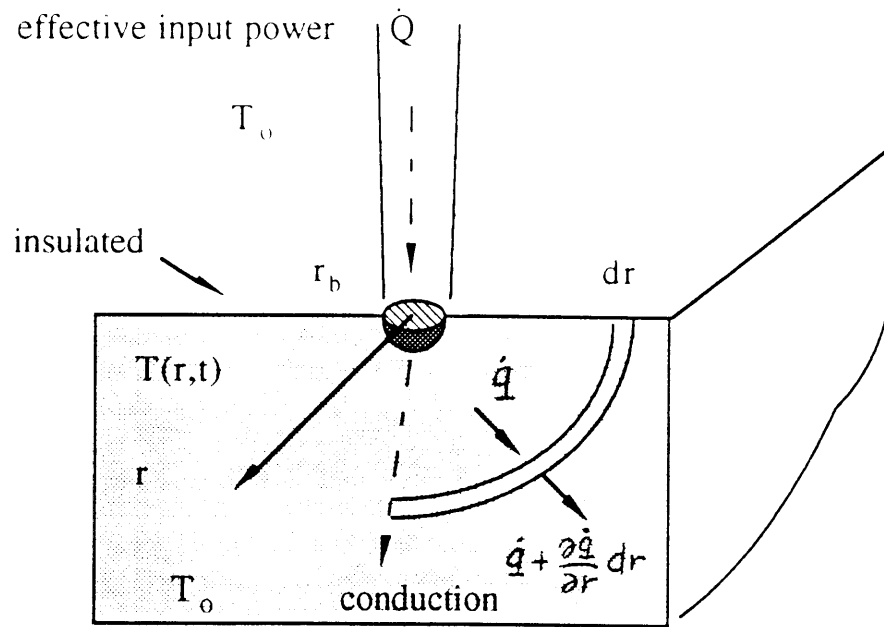


Fig. A4-1

## A5: Thermal Conductive-Convective Model for Laser Heating

This is a simplified model for estimating temperature of a semi-infinite solid subjected to heating from a laser beam spot on the surface. The purpose of this estimation is to provide a supportive understanding of the experimentally estimated surface temperatures on samples used in this research.

This is a modified model for estimating temperature of a semi-infinite solid subjected to heating from a laser beam spot on the surface. Both conduction and convection heat transfer is considered. For simplicity, the convection heat transfer over the solid surface is assumed to be effective only within the laser beam spot, and the rest of the solid surface is assumed to be insulated. This simplification allows the convective effect to be modeled only in the boundary condition and keeps the governing equation one dimensional. Fig. A5-1 depicts the model. The resulting governing equation is the same as eqn. (A4-3),

$$\frac{\partial T}{\partial t} = \alpha \frac{\partial^2 T}{\partial r^2}; \quad \alpha = \frac{k}{\rho c} \quad (\text{A5-1}).$$

The boundary conditions are

$$\dot{Q} - h\pi r_b^2 [T(r_b, t) - T_\circ] = -2\pi r_b^2 k \left. \frac{\partial T}{\partial r} \right|_{r=r_b} \quad (\text{A5-2}),$$

where h is the convective heat transfer coefficient, and

$$T(\infty, t) = T_\circ. \quad (\text{A5-3}).$$

The initial condition is

$$T(r, 0) = T_\circ \quad (\text{A5-4})$$

Eqn. (A5-1)-(A5-4) are basically similar to eqn. (A4-3)-(A4-6) except that the strength of heat source is modified by convective heat transfer, as shown in eqn. (A5-2). These equations can again be solved by Laplace Transform technique. The solution is

$$\frac{T(r,t) - T_{\infty}}{\frac{p}{h}} = \operatorname{erfc}\left(\frac{x}{\sqrt{4\alpha t}}\right) - e^{\beta x + \alpha\beta^2 t} \operatorname{erfc}\left(\frac{x}{\sqrt{4\alpha t}} + \beta\sqrt{\alpha t}\right) \quad (\text{A5-5})$$

where

$$\beta = \frac{h}{2k} \quad (\text{A5-6})$$

and p is the effective input power density, eqn. (A4-8). The surface temperature at the laser spot  $T_s$  is

$$\frac{T_s(t) - T_{\infty}}{\frac{p}{h}} = 1 - e^{-\alpha\beta^2 t} \operatorname{erfc}(\beta\sqrt{\alpha t}) \quad (\text{A5-7}).$$

Using eqns. (A4-8) and (A4-10), eqn. (A5-7) can be rewritten as

$$\frac{T_s(t) - T_{\infty}}{\left(\frac{Pa_b f_c}{\pi r_b^2 h}\right)} = 1 - e^{-\alpha\beta^2 t} \operatorname{erfc}(\beta\sqrt{\alpha t}) \quad (\text{A5-8})$$

where  $a_b$  is the radiative absorptance of the solid surface,  $f_c$  is a correction factor to account for effect of solution absorption, bubble shielding etc., and P is the laser output power. Fig. A5-2 shows the solution of surface temperature, eqn. (A5-8), in dimensionless form. To solve for  $T_s$ , the two major unknowns are h and  $f_c$ . In the case of backside scanning test on Ni-glass film, as described in section 4.1, the surface temperature  $T_s$  was estimated by Ni-film morphology observation and the value of  $f_c$  was close to 1, since there was no bubble shielding or solution absorption. Therefore, the value of h can be solved from eqn. (A5-8), which was found to be  $10^6$  W/m<sup>2</sup>, a very effective convection heat transfer coefficient.

One useful expression of the solution of the solid temperature  $T(r,t)$  can be obtained by dividing eqn. (A5-5) with eqn. (A5-7) to get a normalized temperature and then expressing this normalized temperature in terms of two dimensionless groups, as

$$\frac{T(r,t) - T_0}{T_s(t) - T_0} = \frac{\operatorname{erfc}(A) - e^{-A^2} [e^{(A+B)^2} \operatorname{erfc}(A+B)]}{1 - e^{B^2} \operatorname{erfc}(B)} \quad (\text{A5-9}),$$

where

$$A = \frac{x}{\sqrt{4\alpha t}}$$

$$B = \beta\sqrt{\alpha t}.$$

Solutions of eqn. (A5-9) are shown in Fig. A5-3.

The error function value was obtained from mathematical tables as well as the following approximate expression:

$$\operatorname{erfc}(x) \approx (as + bs^2 + cs^3 + ds^4 + es^5)e^{-x^2} \quad (\text{A5-10})$$

where

$$s = \frac{1}{1 + 0.3275911x}, \quad a = 0.254829592, \quad b = -0.284496736,$$

$$c = 1.421413741, \quad d = -1.453152027, \quad e = 1.061405429.$$

This expression is uniformly accurate to  $10^{-7}$  and can be used in digital computer calculation. [Greenberg 1978]

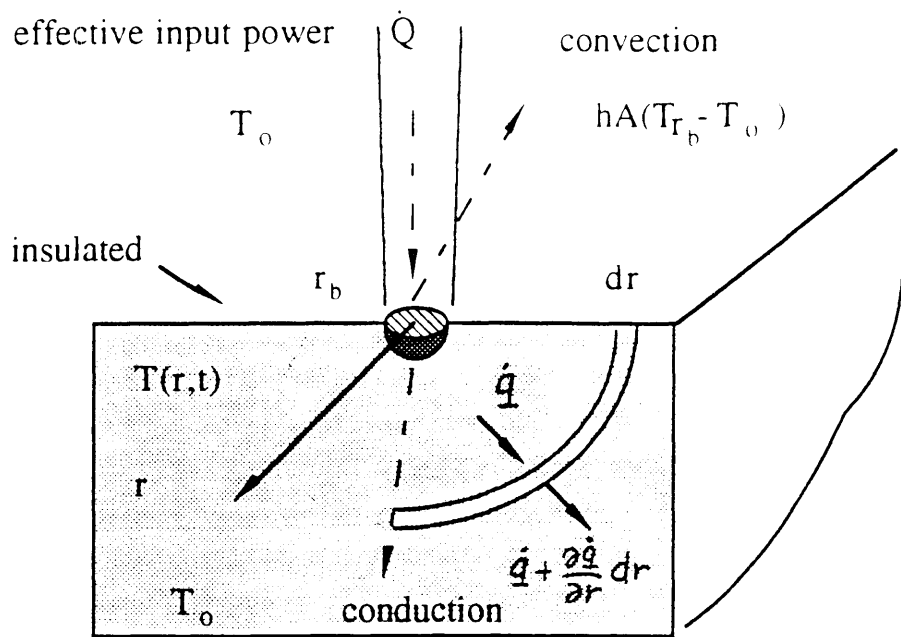


Fig. A5-1

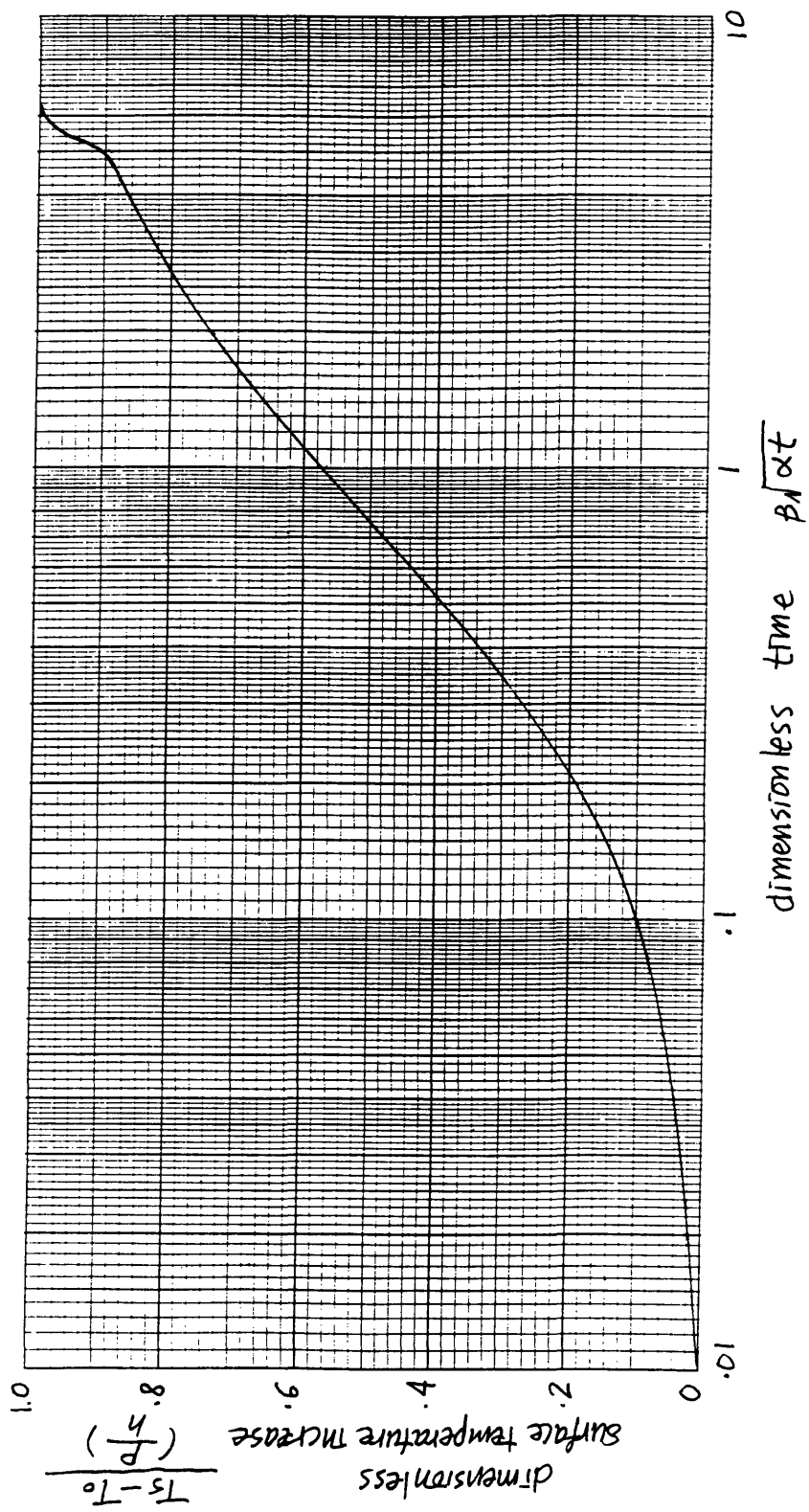


Fig. A5-2

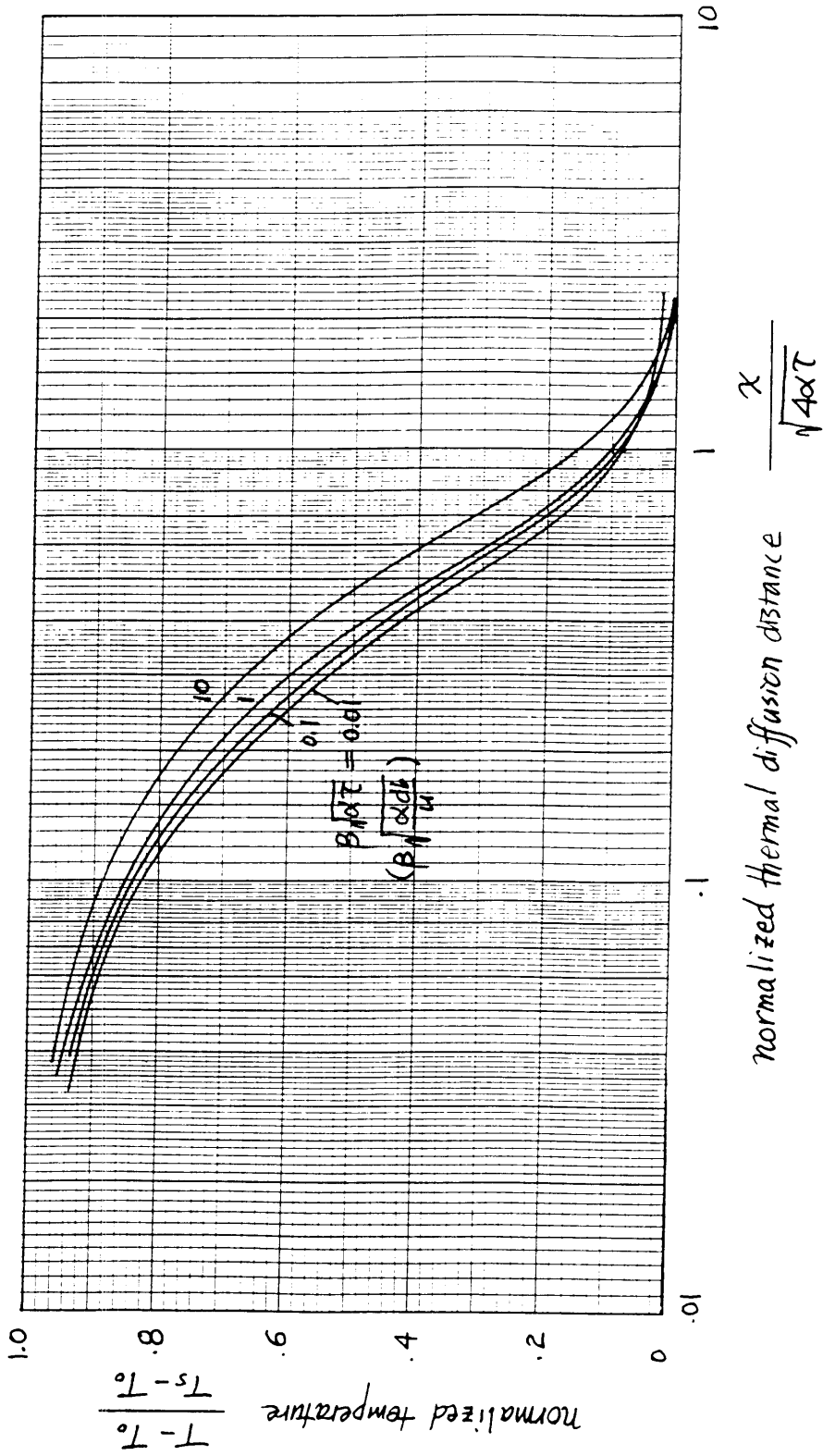


Fig. A5-3

## A6: Boundary Layer Thickness and Diffusion Layer Thickness Estimation

The purpose of this section is to estimate the mass transfer limit in a flow field where the only driving force for mass transfer is the convective-diffusion caused by free stream flow. A comparison between the actual rate limit and this limit can then suggest if there is another mass transfer mechanism.

(a) The relation between boundary layer thickness and diffusion layer thickness

To establish an exact relation between the hydrodynamic boundary layer thickness  $y_h$  and the diffusion layer thickness  $\delta_o$  in a flow field requires solving the hydrodynamic equation and the convective-diffusion equation. To solve for each flow field may be very complicated. However, for the purpose of order of magnitude estimation, this relation can be estimated through Schmidt number,  $Sc$ , by

$$\frac{y_h}{\delta_o} \approx 2Sc^{1/3} = 2\left(\frac{\nu}{D}\right)^{1/3}, \quad (\text{A6-1})$$

where  $\nu$  is fluid viscosity and  $D$  is diffusivity. Eqn. (A6-1) is obtained from solving both hydrodynamic equation and convective-diffusion equation of a rotating disk electrode [see, e.g., Bard and Faulkner 1980, chapter 8]. It is expected that (A6-1) gives a good order of magnitude estimation for most flow fields due to the similarity of transport phenomena. At 80 C, where the electroless Ni plating starts, water viscosity is 0.0038 cm<sup>2</sup>/sec, and Ni<sup>++</sup> diffusivity is 13.6x10<sup>-6</sup> cm<sup>2</sup>/sec (see A9 for source of data), the above ratio is then ~13.

With the above relation, (A6-1), the convective diffusion limit can be estimated from the reactant flux

$$j_l = \frac{D}{\delta_o} C$$

where  $C$  is bulk concentration of the reactant, as long as the flow boundary layer thickness is known. Calculating back, from known deposition rate, a corresponding diffusion layer

thickness can be estimated. For Ni deposition rate of 1  $\mu\text{m}/\text{sec}$ , which corresponds to an equivalent current of 2.9  $\text{A}/\text{cm}^2$ , the required  $\text{Ni}^{++}$  flux is  $1.5 \times 10^{-5} \text{ mol}/\text{cm}^2\text{sec}$ . With a solution bulk concentration of 0.1 M (see A9 for bath composition), the required diffusion thickness is 0.9  $\mu\text{m}$ , and the corresponding boundary layer thickness is 11.7  $\mu\text{m}$ . In (b) and (c), the free stream velocity required to generate this boundary layer thickness is estimated.

(b) Free convective flow caused by laser heating

The exact convective flow field caused by focused laser heating over a solid surface is unknown. However, an approximate flow pattern can be depicted from video observation as shown in [Fig. A6-1](#). Two approximate methods can be used to estimate the boundary layer thickness at a known free stream velocity. The first method is using the solution of rotating disk electrode (RDE) to approximate the real flow field, since it is similar to the flow profile over a rotating disk electrode (RDE), except that the flow direction reverses. According to RDE theory [Bard and Faulkner 1980, chapter 8], the vertical free stream velocity of flow toward the disk is

$$U_o = -0.88(\omega\nu)^{1/2}.$$

The boundary layer thickness is defined at

$$y_h = 3.6(\nu / \omega)^{1/2}$$

Combining the above two expression gives the following relation

$$U_o = -3.168\nu / y_h \tag{A6-2}$$

The free stream velocity required to support a known reaction rate can thus be estimated from the corresponding diffusion layer thickness  $\delta_o$ , and eqns. (A6-1) and (A6-2). Taking the numbers from (a), it can be estimated that a free stream velocity of 10.3  $\text{cm}/\text{sec}$  is required to support 1  $\mu\text{m}/\text{sec}$  Ni deposition rate.

The second method is using the solution of forced convective flow over a flat plate to approximate the real flow. The flat plate boundary layer theory gives the following relation, [Schlichting 1979, chapter VII]

$$U_o = 25 \nu x / y_h^2 \quad (\text{A6-2a})$$

where  $U_o$  is the horizontal free stream velocity and  $x$  is a characteristic length of the flow field. In practice, the value of  $x$  is difficult to determine. However, even if  $x$  is as small as 6  $\mu\text{m}$ , the beam radius, a free stream velocity as large as 40 cm/sec is still required, according to eqn. (A6-2a).

Both estimations suggest that a free stream velocity of 10-100 cm/sec, much larger than observed flow velocity, 1-10 mm/sec, is required to establish the thin diffusion layer to support the actual metal deposition rate, if there is no other microscopic mechanism and convective diffusion is the only mechanism. This implies that there must be a more effective micro-scale mechanism of mass transfer.

(c) Forced convective flow in the Continuous Approach

In the Continuous Photo-Electroforming approach, electroless plating solution flows through the powder bed. The flow field over each powder particle can be modeled by the 3-D stagnation flow theory. Flow over a 3-D stagnation point has been solved by similarity method [see, e.g., Schlichting 1979, chapter V]. From the resulted flow velocity profile, the boundary layer thickness can be defined as

$$y_h \approx 2 / \sqrt{\frac{a}{\nu}} \quad (\text{A6-3})$$

where  $a$  is a constant defining the radial potential flow velocity defined as

$$u = ar. \quad (\text{A6-4})$$

where  $r$  is the radius of the surface around the stagnation point. From potential flow theory, the flow velocity near the tip of a sphere can be expressed as eqn. (A6-4) with

$$a = \frac{3U_0}{2R} \quad (\text{A6-5})$$

where  $R$  is the radius of the sphere and  $U_0$  is the free stream velocity. Combining the above eqns. gives

$$y_h = \sqrt{\frac{8Rv}{3U_0}} \quad (\text{A6-6})$$

A theoretical convective-diffusion rate can thus be estimated using eqn. (A6-1) and (A6-6) with known free stream velocity (flow-through velocity) and particle size,  $5 \mu\text{m}$ , from the Continuous Photo-Electroforming experiments. The result is plotted in Fig. 29A. This rate is about one order of magnitude smaller than the measured laser induced Ni deposition rate, which again suggests that a laser induced mass transfer mechanism is controlling the deposition.

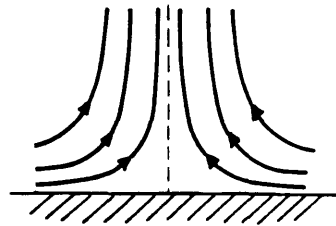


Fig. A6-1

## A7: Bubble Displacement Model

Bubble displacement model was proposed by Ibl and Venczel [1970] to explain the enhanced mass transfer at a gas bubble generating electrode which has a very fast surface reaction rate so that the process is diffusion-controlled. The basic argument is that the displacement, or detaching, of each gas bubble refreshes the interfacial reactant concentrations, and during the time of bubble formation, reactants diffuse to the interface at the diffusion-controlled rate until the bubble detaches and the whole cycle repeats itself. Because the interface is periodically refreshed and the bubble formation time is small, the diffusion-controlled rate is always very high and therefore the mass transfer is enhanced. From the gas bubble formation time, a time averaged reactants flux can be estimated by using the Cottrell current equation, and therefore the mass transfer limited reaction rate can be obtained.

First, the gas bubble formation time is estimated. Assuming the volume generation rate of the gas is  $v$ , then, approximately

$$\text{number of gas bubble per unit area unit time} = \frac{v}{\left(\frac{2}{3} \pi r_{bl}^3\right)}.$$

Over the area of one bubble formation site, i.e.  $\pi r_{bl}^2$ ,

$$\text{number of gas bubble per unit time} = \frac{3v}{2r_{bl}}.$$

where  $r_{bl}$  is the radius of gas bubbles. Therefore, formation time per bubble is

$$\tau = \frac{2r_{bl}}{3v} \quad (\text{A7-1})$$

The diffusion-controlled limiting current can be expressed as, according to the Cottrell limiting current equation, [Bard & Faulkner 1980, chapter 5]

$$i_l = \frac{nFACD^{1/2}}{\sqrt{\pi t}},$$

where  $n$  is the number of electron transferred,  $F$  is Faraday constant, 96487,  $A$  is surface area,  $C$  is bulk concentration,  $D$  is reactant diffusivity, and  $t$  is time. The reactant flux at diffusion limit can be expressed as

$$j_l = \frac{i_l}{AnF} = \frac{CD^{1/2}}{\sqrt{\pi t}}.$$

A time averaged flux can be obtained by integrating over time constant  $\tau$ ,

$$j_{l,ave} = \frac{1}{\tau} \int_0^{\tau} \frac{CD^{1/2}}{\sqrt{\pi t}} dt = 2C \sqrt{\frac{D}{\pi \tau}} = \sqrt{\frac{12vD}{\pi d_{bl}}} C. \quad (A7-2)$$

where  $d_{bl}$  is bubble diameter. An effective diffusion layer thickness  $\delta_p$  can be defined as

$$j_{l,ave} = \frac{D}{\delta_p} C,$$

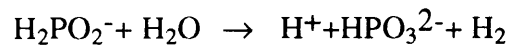
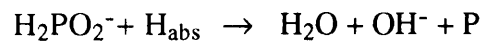
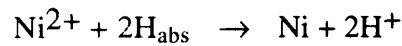
so 
$$\delta_p = \sqrt{\frac{\pi D d_{bl}}{12v}} \quad (A7-3)$$

From reaction stoichiometry (see A-8), the gas generation rate can be estimated from measured deposition rate. From video observation, the bubble size can also be estimated. Therefore, the limiting deposition rate can be obtained from eqn.(A7-2) and can be compared with the measured deposition rate to see if the laser enhanced electroless plating rate can be described by the model. The diffusivity used for this calculation is  $13.6 \times 10^{-6}$  cm<sup>2</sup>/sec (see A9 for source of data). The results are shown in Fig. 31, section 4.2.2.

## A8: Electroless Plating: Principle, Bath Composition, and Sample preparation

### (a) Principle

The currently accepted reaction mechanism of electroless nickel plating from Metals Handbook is as follows, [Fields et al., 1989]

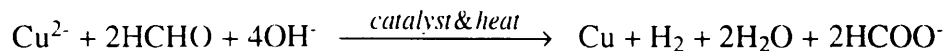


The activation energy for Ni, P, or H<sub>2</sub> formation was found to be 14,000 cal/mol for each production. This suggests a common intermediate reaction, presumably the catalytic dehydrogenation of hypophosphite. The deposition rate of Ni is therefore proportional to the concentration of hypophosphite only, i.e.

$$\text{Ni deposition rate} = k [\text{H}_2\text{PO}_2^-]$$

[Pearlstein 1974, Gutzeit 1959]. The average plating efficiency, defined as moles of nickel produced for every one mole of hypophosphite consumed, is around 35-36% [Fields et al. 1989, Pearlstein 1974]. The phosphor content of electroless nickel is usually around 3-15% wt. This means per 2.78 mol of hypophosphite can generate 1 mol of Ni, less than 0.29 mol of P, and at least 1.49 mol of hydrogen gas. The deposition rate is very sensitive to temperature. Normally, electroless Ni is operated at a bath temperature from 70-95 C, with a deposition rate of 10-30 μm/hr.

In electroless plating of copper, formaldehyde is usually used as the reducing agent and the process also generates hydrogen gas, [Pearlstein 1974]



The electroless copper deposition rate is 2.5-25  $\mu\text{m}/\text{sec}$ , depending on types of bath and operating conditions.

Except Ni and Cu, electroless plating of cobalt, palladium, and silver are also possible [Pearlstein 1974].

#### (b) Bath composition

The composition of the electroless Ni plating solution used in this work, Ni-429M Special from Enthone Inc., is as follows: water 65% wt., nickel sulfate 10%, sodium hypophosphite 15%, propionic acid 5%, and acetic acid 5%. The nickel salt concentration is 0.1 M. The content of nickel metal is 6 gm/l.

The electroless Cu solution (PC electroless Cu from Transene Co. Inc.) has two components. Component A contains 2% copper sulfate, 2% sodium hydroxide, 2% diethanolamine, 8% triethanolamine, and 4% ethylene diamine tetraacetate tetrasodium salt in aqueous solution. Component B contains 25% methonal, 4% formaldehyde (37%), and 71% water.

#### (c) Material Pretreatment Procedure

For electroless plating to work on nonconductive materials, cleaning and pretreatment of the material is very important. Cleaning provides fresh and uncontaminated surfaces for the subsequent procedure, and pretreatment creates catalytic sites on these surfaces.

Tab. A8-1 lists a typical cleaning procedure for nonconductive materials. Usually, different material needs different etching agent. Tab. A8-2 lists some examples. Etching step is sometimes termed as "conditioning". The purpose of etching is to provide some

interlocking roughness on the surface and to provide suitable sites for chemical bonding of subsequently applied metals [Pearlstein 1974].

Tab. A8-1

1. Solvent degrease, e.g. cleaning in methanol
2. Cleaning, (violent rinse or ultrasonic cleaning in distilled water)
3. Etching,
4. Cleaning, (violent rinse or ultrasonic cleaning in distilled water)

Tab. A8-2

Silicon carbide	diluted hydrofluoric acid or diluted mixture of hydrofluoric acid and nitric acid
Aluminum oxide	orthophosphoric acid
Silicon	diluted hydrofluoric acid or diluted mixture of hydrofluoric acid and nitric acid
Nylon	etching not necessary

Pretreatment procedure follows cleaning. The procedure has actually two steps, which are usually referred to as sensitization and activation, or sensitization and nucleation. Sensitization consists of absorbing on the surface of the material a readily oxidizable material. In the activation step, the sensitizer absorbed on the material surface is oxidized thereby reducing the catalytic metal inside the activator solution and depositing it at discrete nucleation centers on the surface. These catalytic nuclei act as growing sites of the subsequent electroless deposits [Pearlstein 1974]. The most common and effective sensitization/activation method is Sn/Pd treatment, which uses a solution of stannous chloride and hydrochloric acid as the sensitizing agent, and palladium chloride with hydrochloric acid as activating agent. In this work, sensitizer solution C and activator solution D from Transene Co. Inc. were used. The composition of solution C is 2% hydrochloric acid and 1 % stannous chloride in water. The composition of solution D is 2 % hydrochloric acid and 1 % palladium chloride in water.

Tab. A8-3 shows a typical process sequence.

Tab. A8-3

- 1 33% hydrochloric acid immersion to protect from harmful drag in; (2 min.)
- 2 Sensitizer solution immersion (2 min.) followed by water rinse;
- 3 Activator solution immersion (2 min.) followed by water rinse;
- 4 5% sulfuric acid dip to speed electroless metal deposition and protect from drag-in contamination; followed by water rinse (for sulfuric acid based electroless plating solution) (3-5 min.)
- 5 Electroless plating
- 6 5% sulfuric acid dip to neutralize surface (3-5 min.); followed by water rinse
- 7 20% hydrochloric acid dip (10-60 sec) followed by water rinse

The effectiveness of the above procedures on silicon, aluminum oxide, silicon carbide, and nylon was confirmed in the experiments done in this research.

## A9: Material Properties

Most of the material properties were taken from the literature, and some of them were tested by our own experiments. Values taken from literature involves unavoidable errors as the preparation of materials might be different. However, model calculations based on these data can still give useful estimates to assist understanding of the physics of the process as described in respective sections in the main text. Neither the listed properties nor the calculations were intended to be precise values or models.

The thermal properties of solid materials were obtained from [Touloukian and Ho 1970]. This data series collect thermal properties data of many different materials prepared by different method. For silicon carbide, thermal conductivity was calculated from density, specific heat data, and thermal conductivity data. As shown in the data series, the thermal conductivity of SiC decreases with increasing temperature in the temperature range of 500-1200 K. Denser SiC has higher thermal conductivity, but the variation is less than a factor of 2 for density from 2.2 to 3.1. The density of the SiC pellet prepared in this work was measured to be about 2.2 g/cm<sup>3</sup>. Therefore, a curve of density 2.2 was used for the thermal conductivity of the SiC pellets. The specific heat of SiC is quite a constant over the above temperature range. At 500 C, the estimated thermal diffusivity of SiC is 6.5 x10<sup>-6</sup> m<sup>2</sup>/sec. For Ni-coated glass, it was assumed that the thin Ni film, of thickness 0.2 μm as measured by Dektak profilometer, had negligible effect on overall thermal properties and the thermal diffusivity of soda lime glass, 5.7x10<sup>-7</sup> m<sup>2</sup>/sec was used, which is quite independent of temperature.

The radiative absorptance of solid materials and coatings were obtained from [Touloukian et al. 1972]. The absorptance of argon laser light of nickel film, determined from reflectance data, is 0.46. The absorptance of argon laser light of SiC is 0.9.

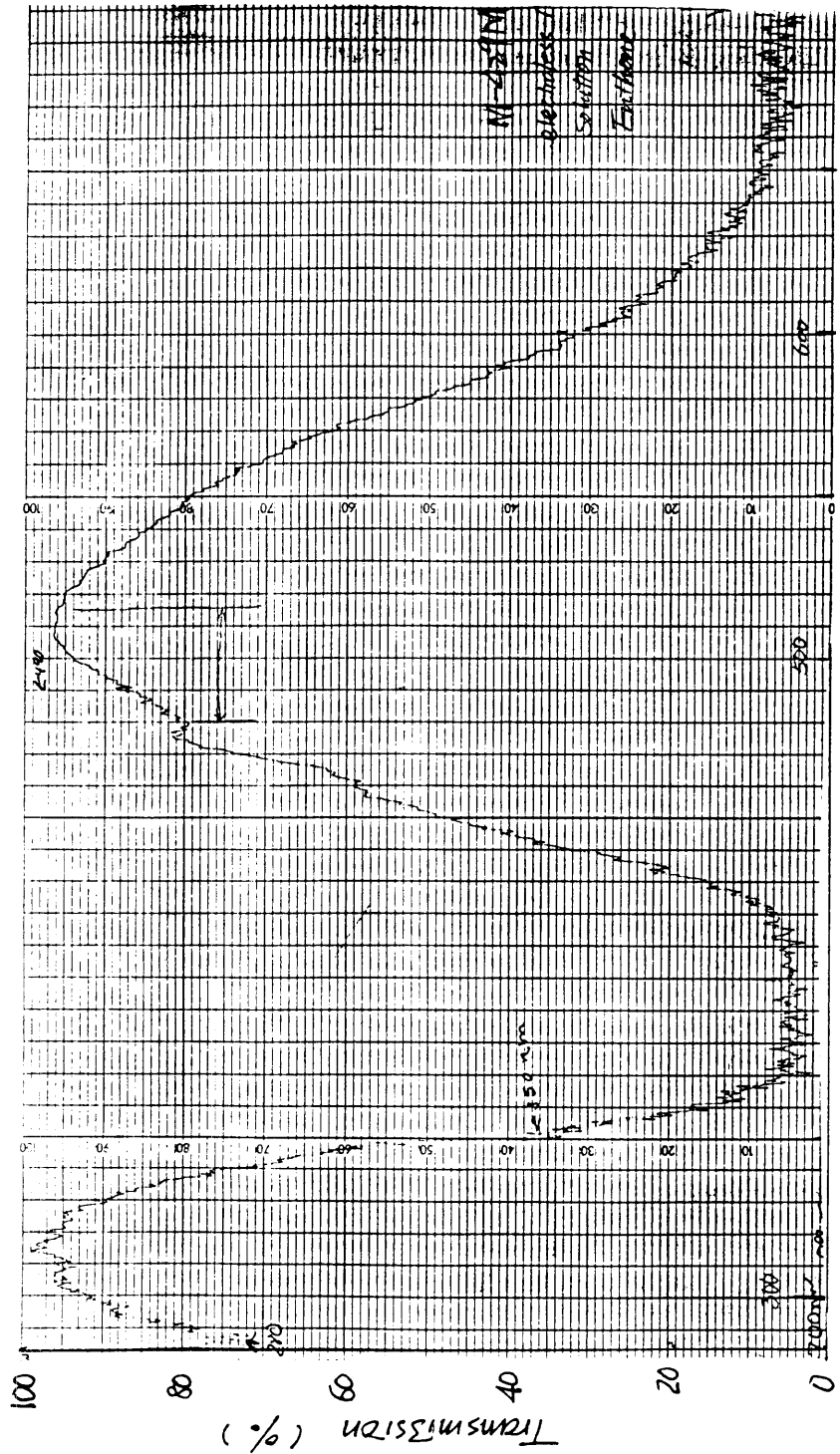
The transmission spectra of electroless plating solutions used in this research were measured by Spectrophotometer 330 of Perkin Elmer, as shown in Fig. A9-1. The light path was 1 cm, and the transmission spectrum of the plastic container is also included in the figures.

No literature on measurement of diffusivity of Ni ion complex is known to the author. According to [Sherwood et al.1975], there appears to be no generally reliable theory or empirical procedure for predicting diffusivity variation with concentration in strong solution. However, all species in aqueous solutions have a diffusivity around  $5 \times 10^{-6}$  cm<sup>2</sup>/sec [Bard & Faulkner 1980, chap. 4]. For the diffusivity of Ni ion complex, a value of  $5-10 \times 10^{-6}$  cm<sup>2</sup>/sec has been used for model calculation in literature [Orlik & Galus 1990, Gangasingh & Tabolt 1991, Hessami & Tobias 1989]. A room temperature value of  $5 \times 10^{-6}$  cm<sup>2</sup>/sec was thus used. However, the electroless plating solution used in this work starts its function at about 80 C. Therefore, the diffusivity was adjusted to 80 C by using the following relation, [Ying et al. 1988]

$$\frac{D\mu}{T} = \text{constant}.$$

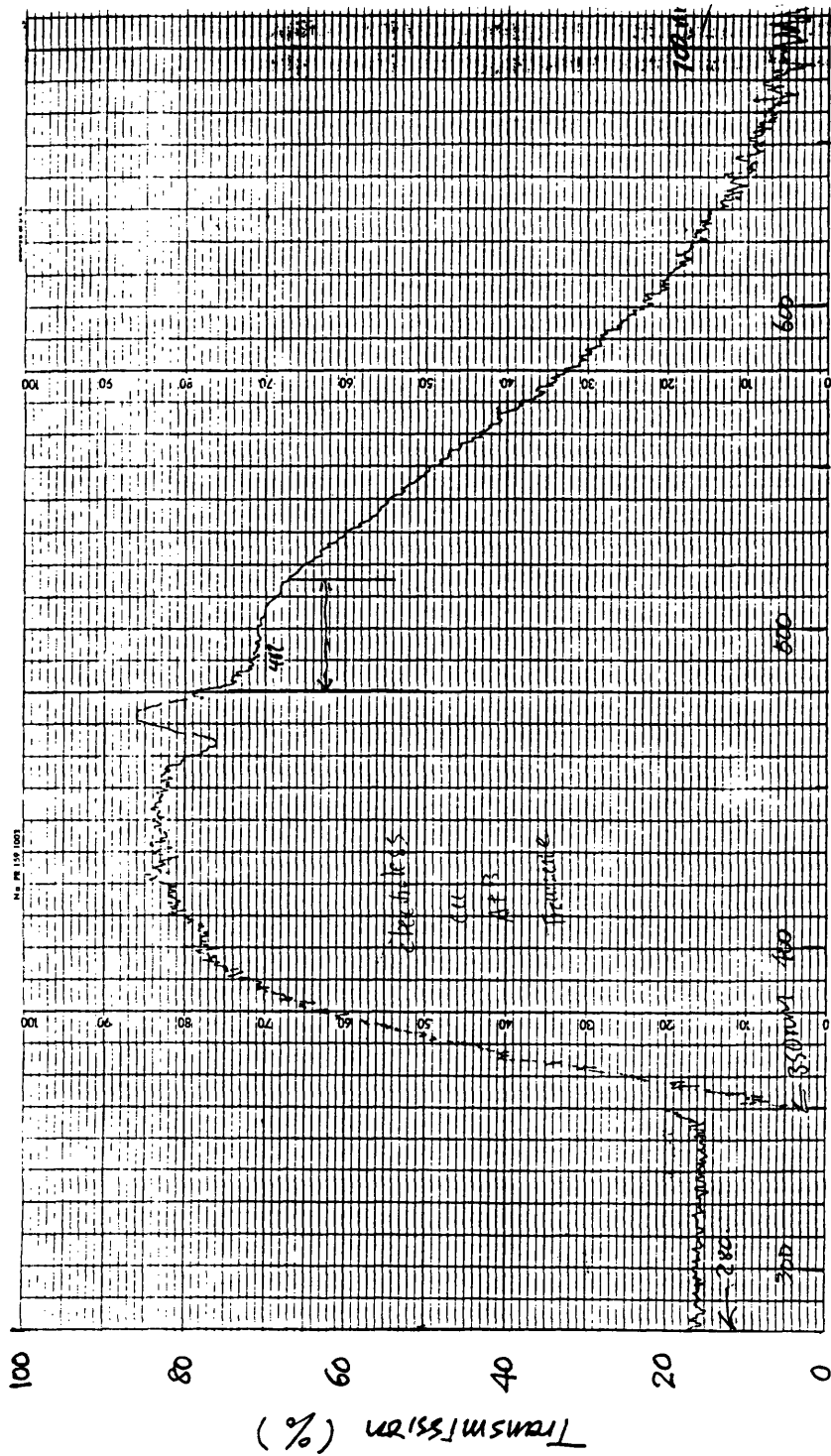
Therefore, the diffusivity of Ni<sup>++</sup> is  $13.6 \times 10^{-6}$  cm<sup>2</sup>/sec.

The composition of the electrolytic copper plating solution used in this work, SEL-REX CuBath XL, is copper sulfate 82 g/l, sulfuric acid 210 g/l, and chloride ion 80 mg/l. The electrolytic nickel plating solution, SEL-REX LECTRO-NIC 10-03, has the composition of nickel sulfate 300 g/l and boric acid 40.5 g/l. The electrolytic silver plating solution, SILVER CY-LESS, has the composition of silver succinimide 3.25 % and potassium hydroxide 2.77 % in water.



Wavelength  $\lambda$  (nm)

Fig. A9-1 (a) Transmission spectrum of electroless Ni solution, with container



wavelength  $\lambda$  (nm)  
 Fig. A9-1 (b) Transmission spectrum of colorless Cu solution, with container

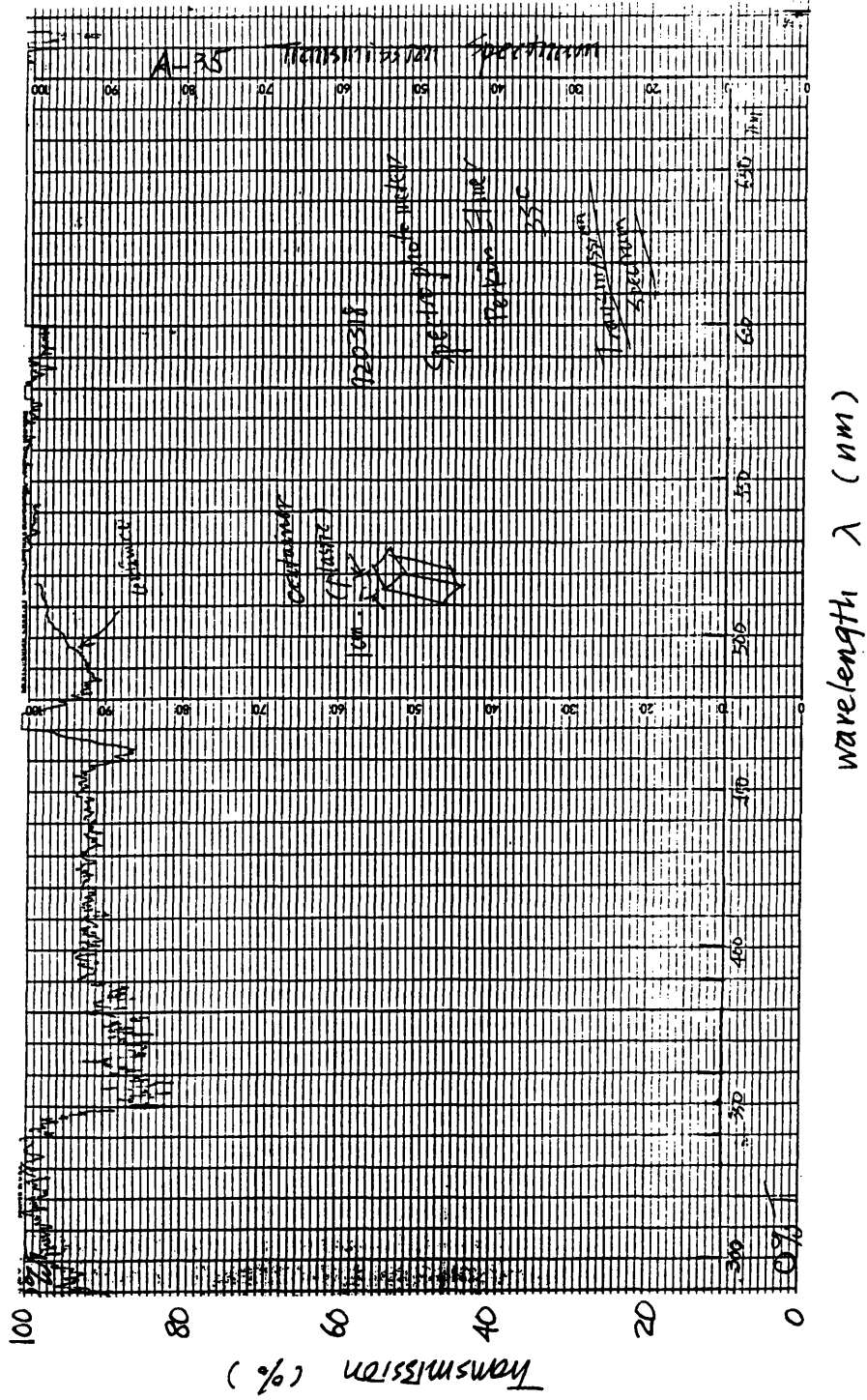


Fig. A9-1 (c) Transmission spectrum of the plastic container

## A10: Flow-through Plating

The metallized layer material can be joined either by electroless plating or by electrolytic plating. In either case, the plating takes place in a porous powder bed and hence is a type of flow-through plating.

Since electroless plating is an autocatalytic process, flowing a heated electroless plating solution through a powder bed causes continuous metal deposition in regions previously defined by photo-metallization. The flow-through provides a supply of reactant until the interconnected porosity is gone. Thus, if a high enough flow is maintained to guarantee uniform plating, high densities can be achieved. For example, consider the joining of a photo-defined geometry in a powder bed of 100 cm<sup>2</sup> area and 0.4 cm thick consisting of 5 μm particles where the part takes 10% of the total volume. If a 0.5 μm coating on each particle is sufficient, about 15 gram of Cu or Ni would be required. In order to have uniform metal plating throughout the powder bed, we may want to restrict the depletion ratio of the flow-through electroless plating. Assuming we are pumping the flow at a differential pressure of 3 x 10<sup>6</sup> Pa, which can be achieved by a diaphragm pump, the resulted flow rate through the powder bed would be about 160 ml/sec. Assuming that the depletion is to be maintained at 1%, then the electroless plating has to be operated at about 5% of its normal rate, 10-30 μm/hr, with the given flow rate. This can be achieved by controlling the solution temperature. In this case, the total joining time would be approximately 25 minutes.

In the case of flow-through electrolytic plating, the layer material actually acts as a porous cathode. Porous electrode and flow-through system find its applications in the recovery or removal of metal ions from waste process streams [Newman 1978, Selman 1978]. Therefore, this flow-through plating process is a typical application of flow-through porous electrodes in electrochemical processes.

Two major parameters to be controlled in the flow-through plating process are solution flow rate and plating current density. Solution flow rate affects the variation and distribution of ion concentration, and current density affects the quality and time of electroplating. For laminar flow, the flow rate through a porous structure is governed by the following relation, [Newman 1978]

$$\Delta p = 4.2 \frac{\mu v L s^2}{A \epsilon^3}$$

where  $\Delta p$  is dynamic pressure difference across the porous structure,  $\epsilon$  is porosity,  $\mu$  is viscosity,  $v$  is volume flow rate,  $s$  is specific area,  $L$  is bed depth, and  $A$  is bed cross-sectional area. Therefore, the flow rate can be controlled by regulating the pressure difference.

Assuming 100% current efficiency, the relation between ion concentration variation and average plating current density can be found, by balancing the charges, as,

$$(C_i - C_0)v = \frac{MsALj}{nF}$$

where  $C_i$  is ion concentration of solution flowing into the porous bed,  $C_0$  is ion concentration of solution flowing out of the porous bed,  $M$  is atomic weight of deposited metal,  $n$  is number of electron transferred in the reaction,  $F$  is Faraday's constant, 96487 (C/equiv), and  $j$  is average current density (A/cm<sup>2</sup>).

As a benchmark, taking the same example described previously, assuming the average current density on each particle is 0.001 A/cm<sup>2</sup>, which is an order of magnitude smaller than normal plating current density, the joining time would take about 23 min. at a current of 34 A. restricting depletion to no more than 1% of the ion concentration during the flow-through (lower depletion percentage results in more uniform plating) would require a flow rate of 15 ml/sec. A pressure difference of  $3.5 \times 10^5$  Pa across the powder bed can provide this flow rate. Due to the solution resistance inside the porous powder bed, the polarization across the powder bed is usually not uniform and thus the current

density distribution is not uniform either. Plating uniformity can be improved by increasing the flow rate, which improves mass transfer inside the powder bed, and by reducing the current density, which reduces the polarization drop across the powder bed. Improvement can also be made by adding certain additives such as chloride ions to reduce the solution resistance. In case of thick parts where highly non uniform polarization across the powder bed may occur, the second plating can be carried out at several stages during the powder buildup to make current density more uniform.

Flow-through plating experiments were performed to examine the feasibility and selectivity of joining by electrolytic plating. Silicon carbide powder of particle size 60-80  $\mu\text{m}$  was first pretreated by the standard Sn/Pd procedure (see A8). A portion of the powder was then coated with a thin layer of copper by immersing in electroless Cu solution at 35-45 C for 15-20 min. The two lots of powder were then filled into a plastic tube-shape mold, 6 mm in diameter and 5 mm high, in a SEL-REX Cubath Cu plating solution. The filling was carefully arranged such that the pretreated but non metallized powder occupied 1/4 of total volume. Both lots of powder were made cathodic by contacting a porous Cu mesh at the bottom of the mold. Plating solution was pumped through the tube mold and the Cu mesh at a flow rate of 0.8-0.9  $\text{cm}^3/\text{sec}$ , and plating at 0.2 A lasted for 5 hours. The metallized particles were all joined together, while the non metallized particles were not. The resulting Cu/SiC part is shown in Fig. A10-1. The recess in the lower right portion of the part was the original position of the pretreated but non metallized powder. Thus, the joining selectivity of flow-through plating was demonstrated.

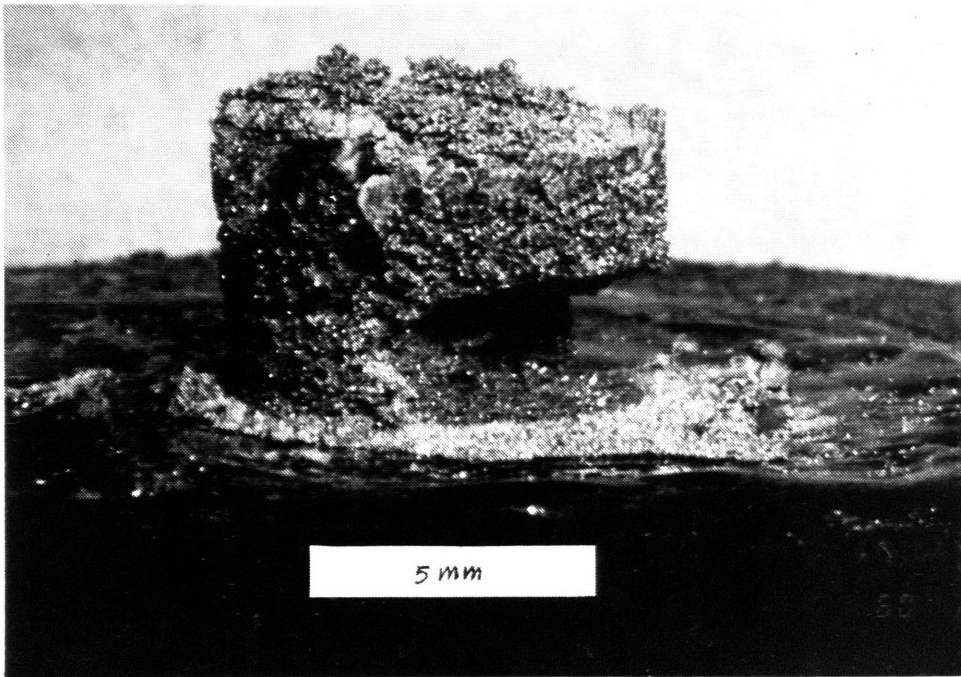


Fig. A10-1

## Bibliography

- Arpaci, V.S., *Conduction Heat Transfer*, Addison-Wesley, Reading, Mass., 1966
- Ashley, S., "Rapid Prototyping Systems", *Mechanical Engineering*, April 1991, pp.34-43.
- Bard, A.J. and Faulkner, L.R., *Electrochemical Methods: Fundamentals and Applications*, John Wiley and Sons, N.Y., 1980
- Berry, J., Medical Engineer, 5 Victoria Dr., Westkirby, Merseyside, England, Method of Electrostatic Spinning Process, private communication, 1993
- Bertoncini, D. " The Development of a Zif Connector Design and Manufacturing Process", *23rd Annual Connector and Interconnection Technology Symposium IICIT*, Deerfield, Illinois, 1990, pp. 199-219
- Binning, G., Rohrer, H., Gerber, Ch. and Weibel, E., "Surface Study by Scanning Tunneling Microscopy", *Physical Review Letters*, vol.49, no.1, 1982, pp.57-61.
- Bloomstein, T.M. and Ehrlich, D.J., "Laser Deposition and Etching of Three-Dimensional Microstructures", *IEEE*, CH2817-5/91/0000-0507, 1991, reprint.
- Carrol, B.H., Higgins, G.C. and James, T.H., *Introduction to Photographic Theory: The Silver Halide Process*: John Wiley and Sons (New York)1980.
- Cote, R.E. and Bouchard, R.J., "Thick-film Technology", in *Electronic Ceramics: Properties, Devices, and Applications*, ed. by L.M. Levinson, Marcel Dekker Inc., N.Y., 1988
- Deckard, C. and Beaman, J., "Solid Freeform Fabrication and Selective Powder Sintering", in Proceedings NAMRAC Symposium #15.
- Deitz, D., "Stereolithography Automates Prototyping", *Mechanical Engineering*, Feb. 1990, pp.34-39.
- Dini, J.W., "Ion Plating Can Improve Coating Adhesion", *Metal Finishing*, September 1993, pp. 15-20
- Ehrfeld, W., Bley, P., Gotz, F., Hagmann, P., Maner, A., Mohr, J., Moser, H.O., Munchmeyer, D., Schelb, W., Schmidt, D. and Becker, E.W. "Fabrication of Microstructures Using the LIGA Process", *IEEE TH0204-8/87/0000/0011*, 1987, reprint.
- Fallon, M. "Desktop Manufacturing Takes You From Art to Part", *Plastics Technology*, Feb. 1989.
- Fan, L., Tai, Y.C. and Muller, R.S., "Integrated Movable Micromechanical Structures for Sensors and Actuators", *IEEE Transactions on Electronic Devices*, vol.35, no.6, June 1988, pp.724-730.
- Fields, W.D., Duncan, R.N., Zickgraf, J.R., and Baudrand, D.W., "Electroless Plating", *Metals Handbook*, 9th ed., vol. 5, ASM, Metals Park, Ohio, 1989

- Frazier, A.B. and Allen, M.G., "High Aspect Ratio Electroplated Microstructures using a Photosensitive Polyimide Process", *Micro Electro Mechanical Systems 92*, Travemunde, Germany, February 4-7, 1992, pp. 87-92
- Gangasingh, D. and Talbot, J.B. "Anomalous Electrodeposition of Nickel-Iron", *Journal of Electrochemical Society*, v. 138, n. 12, Dec. 1991, pp. 3605-3611
- Gerhart, P.M. and Gross, R.J., *Fundamentals of Fluid Mechanics*, Addison-Wesley Pub. Co., Reading, Mass., 1985
- German, R.M. *Powder Injection Molding*, Metal Powder Industries Federation (Princeton, N.J.)1990, pp.376-378.
- Gorczyca, T.B. et al. "PECVD of Dielectrics", in *VLSI Electronics Micro Structure Science, vol. 8: Plasma Processing for VLSI*, ed. by E.G. Einspruch and D.M. Brown, Academic Press Inc., Orlando, Fla., 1984
- Greenberg, M.D., *Foundations of Applied Mathematics*, Prentice-Hall Inc., Englewood Cliffs, New Jersey, 1978
- Guckel, H., Skrobis, K.J., Christenson, T.R., Klein, J., Han, S., Choi, B., Lovell, E.G. and Chapman, T.W., "On the Application of Deep X-Ray Lithography with Sacrificial Layers to Sensor and Actuator Construction (the Magnetic Micromotor with Power Takeoffs)", *Transducer '91*, The Sixth International Conference on Solid-State sensors and Actuators, paper substitution.
- Gutzeit, G., "An Outline of the Chemistry involved in the the Process of Catalytic Nickel Deposition From Aqueous Solution", *Plating*, October 1959, pp.1158-1164
- Haberle, W., Horber, J.K.H., and Binnig, G., "Force Microscopy on Living Cells", *Journal of Vacuum Science and Technology B*, vol. 9, no. 2, 1991, pp. 1210-1213
- Hessami, S. and Tobias, C.W., " A Mathematical Model for Anomalous Codeposition of Nickel-Iron on a Rotating Disk Electrode", *Journal of Electrochemical Society*, v. 136, n. 12, Dec. 1989, pp. 3611-3616
- Honma, H. and Kanemitsu, K., "Electroless Nickel Plating on Alumina Ceramics", *Plating and Surface Finishing*, September 1987, pp.62-67
- Horton, R.A., "Investment Casting", *Metals Handbook*, 9th ed., vol. 5, ASM, Metals Park, Ohio, 1989
- Ibl, Von N. and Venzel, J., "Untersuchung des Stofftransports an gasentwickelnden Elektroden", *Metalloberfläche*, v.24, 1970. pp. 365
- Ikuta, K. and Hirowatari, K., "Real Three Dimensional Micro Fabrication using Stereo Lithography and Metal Molding", *Proceedings of IEEE Micro Electro Mechanical Systems*, Fort Lauderdale, Florida, February 7-10, 1993, pp. 42-47
- Janssen, L.J.J. and Hoogland J.G., "The Effect of Electrolytically Evolved Gas Bubbles on The Thickness of the Diffusion Layer", *Electrochimica Acta*, 1970, vol. 15, pp. 1013-1023

- Janssen, L.J.J. and Hoogland J.G., "The Effect of Electrolytically Evolved Gas Bubbles on The Thickness of the Diffusion Layer -- II", *Electrochimica Acta*, 1973, vol. 18, pp. 543-550
- Kiang, Y.C., Moulic, J.R. and Zahavi, J., "Metal Silicide Formed by Laser Irradiation of Silicon Chip in Plating Solution", *IBM Technical Disclosure Bulletin*, vol. 26, no. 1, June 1983, pp.327.
- Macdonald, C., Chen, L.Y., Yao, J.J., Zhang, Z.L., McMillan, J.A. and Thomas, D.C., "Selective Chemical Vapor Deposition of Tungsten for Microelectromechanical Structures," *Sensors and Actuators*, vol. 20, 1989, pp.123-133.
- Morita, N., Watanabe, T. and Yoshida, Y., "Selective Area Deposition of Metal Thin Films on Ceramic Substrates by Laser-induced Plating", *Transactions of the Japan Society of Mechanical Engineers, Mechanical Engineers, Part C*, vol.55 no.515, July 1989, pp.1790-1795.
- Muller, R.S. and Tai, Yu C., "Micromechanical Elements and Methods for their Fabrication", U.S.Pat. No. 4,740,410, 1988.
- Newman, J.S. and Tiedemann, W., "Flow-Through Porous Electrodes", in *Advances in Electrochemistry and Electrochemical Engineering*, vol.11, ed. by H. Gerischer and C.W. Tobias, John Wiley and Sons (New York) 1978.
- O'Connor, L., "MEMS: Microelectromechanical Systems," *Mechanical Engineering*, Feb. 1992, pp. 40-47.
- Orlik, M. and Galus, Z. "Electrochemistry of the Nickel Cyanide System at Mercury Electrode", *Journal of Electroanalytical Chemistry Society*, v. 296, 1990, pp.101-115
- Parker, K., "Electroless Nickel: State of the Art", *Plating and Surface Finishing*, March 1992, pp. 29-33
- Pearlstein, F., "Electroless Plating", in *Modern Electroplating*, ed. by F.A. Lowenheim, John Wiley & Sons, Inc. (New York) 1974.
- Petersen, K. et al., "Silicon Fusion Bonding for Pressure Sensors," *IEEE TH215-4/88/0000-0014*, 1988.
- Pleskov, Yu. V. and Gurevich, Yu. Ya., *Semiconductor Photoelectrochemistry*, Chapters 7 and 8, Consultant Bureau (New York) 1986.
- Puippe, J.Cl., Acosta, R.E., and von Gutfeld, R.J., "Investigation of Laser Enhanced Electroplating Mechanisms", *Journal of Electrochemical Society*, v. 128, n. 12, 1981, pp. 2539-2545
- Reiche, H., Dunn, W.W. and Bard, A.J., "Heterogeneous Photocatalytic and Photosynthetic Deposition of Copper on TiO<sub>2</sub> and WO<sub>3</sub> Powders", *Journal of Physical Chemistry*, vol. 83, no. 17, 1979, pp. 2248.
- Richerson, D.W., *Modern Ceramic Engineering*, Marcel Dekker Inc., N.Y., 1982

- Sachs, E., Cima, M., Williams, P., Brancazio, D. and Cornie, J., "Three Dimensional Printing: Rapid Tooling and Prototypes Directly From a CAD Model", *Journal of Engineering for Industry*, vol. 114, no.4, Nov. 1992, pp. 481-488.
- Saubestre, E.B., "Plating on Nonconductors," in *Modern Electroplating*, ed. by F.A. Lowenheim, John Wiley & Sons, Inc. (New York) 1974.
- Schlichting, H., *Boundary Layer Theory*, McGraw-Hill, N.Y., 1979
- Schwartz, B. "Ceramic Packaging of Integrated Circuits", in *Electronic Ceramics: Properties, Devices, and Applications*, ed. by L.M. Levinson, Marcel Dekker Inc., N.Y., 1988
- Schwartz, M. "The Chemical Reduction of Nickel-Phosphorous Alloys from Pyrophosphate Solutions", Technical Proceedings of the Forty-Seventh Annual Convention, American Electroplaters' Society, Los Angeles, Cal., July 24-28, 1960, pp. 176-183
- Seidel, H., Csepregi, L., Heuberger, A. and Baumgartel, H., "Anisotropic Etching of Crystalline Silicon in Alkaline Solutions", *Journal of Electrochemical Society*, vol. 137, no. 11, Nov. 1990, pp.3612-3626.
- Selman, J.R. and Yuh, C.Y., "Current Distribution in Flow-Through Electrodes during Electrodeposition", in *Advances in Electrochemistry and Electrochemical Engineering*, vol.11, ed. by D.D. Snyder et al., The Electrochemical Society Inc. (Pennington, NJ) 1982.
- Sherwood, T.K., Pigford, R.L., and Wilke, C.R., *Mass Transfer*, McGraw-Hill Inc., N.Y. 1975
- Siegrist, F.L., "Electroforming with Nickel: A Versatile Production Technique", *Metal Progress*, Nov.1964, pp.121-130.
- Smith, W.F. *Structures and Properties of Engineering Alloys*, McGraw-Hill Inc., N.Y., 1981
- Strecker, H. and Persch, G., "Applications of Scanning Tunneling Microscope in Magnetic Storage Device Manufacturing", *Journal of Vacuum Science and Technology B*, vol. 9, no. 2, 1991, pp. 663-665
- Touloukian, Y.S., DeWitt, D.P., and Hrenicz, R.S., *Thermal Radiative Properties: Coatings*, IFI/Plenum, N.Y., 1972
- Touloukian, Y.S. and DeWitt, D.P., *Thermal Radiative Properties: non metallic solids* IFI/Plenum, N.Y., 1972
- Touloukian, Y.S. and Ho, C.Y., *Thermophysical Properties of Matter: The TPRC Data Series*, IFI/Plenum, N.Y., 1970
- Tucker, Marla C., "Meeting Global MCM Manufacturing Challenges", *Solid State Technology*, June 1992, pp.101-104.

- Ulrich, D.R. "Dielectric Materials, Processing, and Controls", in *Handbook of Thickfilm Hybrid Micro-Electronics*, ed. by C.A. Harper. McGraw-Hill Book Co., N.Y., 1974
- Van der Putten, Andre M.T.P., Jacobs, Jan W.M., Rikken, Jan M.G. and de Kort, Kees G.C.. "Laser-Induced Metal Deposition From the Liquid Phase", *SPIE (Society of Photo-Optical Instrumentation Engineers)*, vol. 1022, 1988, pp. 71-76.
- Wang, S.S., McNeil, V.M. and Schmidt, M.A., "Selective Etching of N-type Silicon Using Pulsed Potential Anodization", *Transducer '91*, The Sixth International Conference on Solid-State Sensors and Actuators, paper substitution.
- Wolf,S. and Tauber, R.N., *Silicon Processing for the VLSI Era, volume 1: Process Technology*, Lattice Press, Sunset Beach, Cal., 1986
- Wolf,S. *Silicon Processing for the VLSI Era, volume 2: Process Integration*, Lattice Press, Sunset Beach, Cal., 1990
- Wolfe, A., "Micromachining Moves Into High Gear", *Mechanical Engineering*, Sept. 1990, pp.49-53.
- Wrighton, M.S., Wolczanski, P.T. and Ellis, A.B., "Photoelectrolysis of Water by Irradiation of Platinized N-Type Semiconducting Metal Oxides", *Journal of Solid State Chemistry*, no.22, 1977, pp.17-19.
- Ying, R.Y. et al., "Selected Transport Properties of Some Electroless Copper Plating Baths", *Journal of Electrochemical Society*, v. 135, n. 3, March 1988, pp.654-656
- Young, W.S. "Multilayer Ceramic Technology", in *Ceramic Materials for Electronics: Processing, Properties, and Applications*, ed. by Buchanan, R.C., Marcel Dekker Inc., N.Y., 1986